THESES SIS/LIBRARY
R.G. MENZIES LIBRARY BUILDING NO:2
THE AUSTRALIAN NATIONAL UNIVERSITY
CANBERRA ACT 0200 AUSTRALIA

TELEPHONE: +61 2 6125 4631
FACSIMILE: +61 2 6125 4063
EMAIL: library.theses@anu.edu.au

USE OF THESES

This copy is supplied for purposes
of private study and research only.
Passages from the thesis may not be
copied or closely paraphrased without the
written consent of the author.

Defect Engineering of InP and InGaAs for Optoelectronic Applications

Christine Yvette Carmody

A thesis submitted for the degree of

Doctor of Philosophy

at the

Australian National University

June 2003

Acknowledgements

This thesis was done thanks to the supervision, support and guidance of Prof. Chennupati Jagadish at the Department of Electronic Materials Engineering, Research School of Physical Sciences and Engineering, ANU. Significant advice and assistance with experimental techniques, as well as growth of structures, was also provided by Dr. Hark Hoe Tan. To these I would like to extend my sincere thanks for their patience and dedication in helping me to finish this work. Thanks also to Dr. Fu Lan for her help and stimulating discussions with the intermixing studies, Prof. Henri Boudinov for his insightful contributions with the Hall effect and isolation studies (as well as pertinent philosophical advice), likewise Dr. Sanju Deenapanray for his enthusiastic contributions to my understanding of defects in semiconductors, and Dr. Manuela Buda, whose timely assistance always left me several steps closer to unraveling my results.

Understanding the results of my experiments could not have reached the level of completion it did without a number of crucial complementary experiments done on my behalf. Dr. Lap van Dao, under the supervision of Prof. Mike Gal at the School of Physics, University of New South Wales, did a number of time resolved photoluminescence measurements for me. Dr. Max Lederer and Vesselin Kolev under Prof. Barry Luther Davies at the Laser Physics Centre, Research School of Physical Sciences and Engineering, Australian National University, provided detailed time resolved differential reflectance measurements on my implanted InP samples. Dr. Zou Jin, at the Electron Microscope Unit at the University of Sydney, performed extensive XTEM analysis. XPS analysis was kindly performed by Dr. Bill Bin Gong at the University of New South Wales, whose work as it turned out was pivotal to understanding

intermixing in the InP/InGaAs based quantum well systems. In Sweden I was lucky to have outstanding collaborators in both the optical and electrical analysis of my results. Andreas Gaarder and Prof. Saulius Marcinkevicius at the Royal Institute of Technology provided thorough and enlightening time resolved optical analysis, and the scanning probe microscopy team of Olivier Douheret and Kestas Maknys under the supervision of Prof. Anand Srivanasan clarified my understanding of the electrical characteristics of my samples enormously with their work. To all these I extend my heartfelt gratitude.

Thanks also to my fellow students and staff at EME, who cast a friendly if surprised eye on my eccentricities and were a joy to work amongst: Prof. Jim Williams, Prof. Rob Elliman, Dr. Mark Ridgway, Dr. Neville Fletcher, Dr. Mladen Petravic, Dr. Gustavo Azevedo, Dr. Jenny Wong-Leung, Dr. Stephanie Cheylan, Dr. Craig Johnson, Dr. Michael Cohen, Dr. Chris Glover, Dr. Charlene Lobo, Dr. Annette Dowd, Dr. Tessica Weijers, Dr. Sergei Kucheyev, Dr. Jodie Bradby, Michael Gao, Penny Lever, Jillian Hay, Marc Spencer, Nat Smith, Kallista Stewart, Victoria Coleman, Michael Fraser, David Brett, Andrew Wilkinson, Ali Khalil and Paulus Gareso.

For invaluable technical support (and motorbike advice): Michael Aggett, Tony Watt, Alan Hayes, Tom Halstead, David Llewellyn, Bernie King and Martin Conway.

For administrative support, my sincere thanks go to Ms. Laura Walmsley and Ms Renee Vercoe.

My sincere appreciation for support, mentoring and inspiration goes in particular to Dr. Vijoleta Braach-Maksvytis, Dr. Burkhard Raguse, as well as Dr. Grant Griffiths, Jan Myers, Dr. Zain Kachwalla, Dr John Wiggins, Dr Torsten Reda and Dr Greg Stevens and others at Biomimetic Engineering, Commonwealth Science and Industrial Research Organisation, who allowed me an insight into the wonderful things happening at the interface between physics

and biochemistry. My work on self assembled monolayers on semiconductors has not been included in this Thesis due to the complex nature of the phenomena associated with this field. Although a lot of effort has gone into understanding the physical processes taking place at the interface between semiconductors and organic films, the phenomena were found to be much more complex than initially anticipated. This emerging field could be pursued as a new research area in its own right.

And thanks especially to all my long-suffering, entertaining and amazing friends, because there would be no sanity without you.

The financial assistance provided by the Australian Postgraduate Award (APA) scheme, Australian National University, as well as the CSIRO Telecommunications and Industrial Physics PhD Scholarship is acknowledged.

To my parents and my sister.

Abstract

InP and InGaAs lattice matched to InP hold a special place in the optoelectronics industry because of their room temperature bandgaps of 1.27 and 0.73 eV; these translate into emission/detection wavelengths of ~ 0.9 and 1.6 μm. As such, they are ideal for the development of long wavelength technology, in particular the 1.3 and 1.55 μm emissions that are achievable in lattice matched InGaAs/InP systems, which can be transmitted through optical fibre with low signal loss for long distance telecommunications. However, the device processing technologies of InP and InGaAs are less mature than those of, say, GaAs or Si, and continuing research is needed to take full advantage of the intrinsic properties of these materials.

One branch of current research involves defect production and diffusion, which is known to greatly modify the electrical and optical properties of these semiconductors. Ion implantation is one way of introducing a large amount of defects, and a significant part of this work focuses on understanding the changes to the electrical and optical properties of InP and InGaAs resulting from such implantation. Combined with structural studies, an insight into multiple defective layers of varying optical and electrical properties after implantation has been gleaned. In both InP and InGaAs, implantation was found to result in large concentrations of shallow donors which reduced the resistance of the semiconductor. Depending on the element implanted, this reduced resistivity was concentrated in one or two layers within the damaged region. Implantation also resulted in the creation of non-radiative recombination centers, which in some cases reduced the carrier lifetime of the material to the sub-picosecond range. With the aim of creating materials suitable for ultrafast photodetectors, this work has successfully found ways to increase the resistivity of both implanted InP and InGaAs while keeping the response times as low as possible.

In addition to the creation of defects, their diffusion was induced using annealing techniques, and the corresponding structural, electrical and optical changes observed. This provided another parameter for varying the properties of defective InP and InGaAs with device applications in mind. Annealing, in combination with ion implantation and dielectric capping layer techniques, was also used to promote interdiffusion of InP/InGaAs and InGaAs/AlGaInAs quantum well structures, thereby tuning the emission/detection wavelengths. The damage accumulation processes resulting from implantation in InP and InGaAs at different temperatures was found to strongly influence the degree of interdiffusion achieved. This was related to whether implantation conditions were conducive to formation of point defects or more complex clusters and loops, since the former were more mobile and thus good vectors for interdiffusion. Strain, as well as the interplay of group III and group V interdiffusion and surface chemistry, was found to play a major role in the amount of wavelength tuning that was achievable. The quantum well structures studied showed a great deal of versatility in terms of the obtained peak emission wavelength shifts, and in some cases this emission/detection wavelength was actually shifted to larger values (redshifted), something not achievable in standard interdiffusion of AlGaAs/GaAs and InGaAs/GaAs quantum wells.

This work has provided clear advances in the understanding of defective InP and InGaAs with direct applications to devices. By varying implant dose, initial free carrier concentration, annealing temperature and dielectric deposition parameters, bulk materials and heterostructures can be obtained with the ideal characteristics for optoeletronic applications.

Contents

1. **Introduction** 1

2. **Experimental Techniques** 6

2.1. Introduction 7

2.2. Epitaxial Growth/Samples 7

2.3. Sample Processing 8

2.3.1. Ion implantation 8

2.3.2. Rapid Thermal Annealing (RTA) 13

2.3.3. Plasma Enhanced Chemical Vapor Deposition (PECVD) 13

2.3.4. Electron Beam Evaporation 15

2.3.5. Spin-on Glasses (SOGs) 15

2.4. Material Characterisation 16

2.4.1. Double Crystal X-ray Diffractometry (DCXRD) 16

2.4.2. Cross-sectional Transmission Electron Microscopy (XTEM) 17

2.4.3. Rutherford Backscattering - Channeling Spectrometry (RBS-C) 18

2.4.4. X-ray Photoelectron Spectroscopy (XPS) 20

2.4.5. Sheet Resistance 22

2.4.6. Hall Effect 22

2.4.7. Scanning Spreading Resistance Microscopy (SSRM) 25

2.4.8. Scanning Capacitance Microscopy (SCM) 27

2.4.9. Photoluminescence (PL) 28

2.4.10. Time Resolved Photoluminescence (TRPL) 30

2.4.11. Time Resolved Differential Reflectance (TRDR) 31

References 33

3. **Structural, Electrical and Optical Properties of Ion Implanted InP** 37

3.1. Introduction 38

3.2. Experimental 39

3.3. Structural Studies 41

3.3.1. Dose dependence 41

3.3.2. Implant element and annealing dependence 44

3.4. Electrical Studies 50

3.4.1. Dose dependence 50

3.4.2. Implant element and annealing dependence 53

3.5. Optical Studies 64

3.5.1. Dose dependence 64

3.5.2. Implant element and annealing dependence 65

3.6. Conclusion 69

References 71

4. **Electrical Isolation of *n* - and *p* - $In_{0.53}Ga_{0.47}As$** 73

4.1. Introduction 74

4.2. Experimental 76

4.3. *p* - InGaAs 77

4.4. n - InGaAs 84

4.5. Conclusion 88

References 90

5. **Ion Implanted InP for Ultrafast Photodetector Applications** 92

5.1 Introduction 93

5.2 Experimental 94

5.3 MeV Fe ion implants into SI - InP 95

5.4 MeV P ion implants into p - InP 104

5.5 Conclusion 110

References 111

6. **Ion Implanted InGaAs for Ultrafast Photodetector Applications** 113

6.1 Introduction 114

6.2 Experimental 115

6.3 MeV Fe ion implants into undoped InGaAs 116

6.4 MeV P ion implants into p - InGaAs 134

6.5 Conclusion 138

References 140

7. Ion implantation Induced Interdiffusion in InP and InGaAs Based Quantum Wells 142

7.1 Introduction 143

7.2 Experimental 145

7.3 Thermal Stability of the Quantum Wells 148

7.4 Cap Layer Implants (Low Energy) 150

7.4.1 InGaAs/InP Quantum Wells 150

7.4.2 InGaAs/AlInGaAs Quantum Wells 156

7.5 Deep Implants (High Energy) 161

7.6 Conclusion 163

References 165

8. Impurity Free Vacancy Disordering in InP/InGaAs Quantum Wells 167

8.1 Introduction 168

8.2 Experimental 173

8.3 SiO_2 Induced Interdiffusion 174

8.4 SiO_2, SiN_x or TiO_2 Single Layer Induced Interdiffusion 178

8.5 SiO_2- and SiN_x or TiO_2 Bilayer Induced Interdiffusion 182

8.6 Spin-on Glass Induced Interdiffusion 186

8.7 Conclusion 191

Suggestions for Further Work 193

References 194

9. Concluding Remarks and Suggestions for Further Work 196

List of Figures

2.1. Profile of In vacancies as a function of depth for 1 MeV P ion implantation into InP, as simulated by TRIM 9

2.2. Schematic of the 1.7 MV tandem ion accelerator used for high energy ion implantation 11

2.3. Configuration of the PECVD system 14

2.4. Schematic of a double-crystal X-ray diffractometer (DCXRD) 17

2.5. Schematic representation of the backscattering process for a specific geometry 19

2.6. Schematic of the basic apparatus used in X-ray photoelectron spectroscopy 21

2.7. Schematic diagram to illustrate the Hall effect on a semiconductor sample in the form of a "Hall bar" 23

2.8. Schematic diagram to illustrate the van der Pauw configuration 25

2.9. Schematic representation of the photoluminescence setup 29

3.1. DCXRD of 1 MeV P ion implanted SI InP at 200°C as a function of dose 42

3.2. DCXRD for 10^{16} cm^{-2} implant of 1 MeV P ions at 200°C and model (a); (b) strain profile corresponding to simulated spectrum in (a) 42

3.3. DCXRD of 3.3 MeV In ion implanted SI InP at 200°C at different doses corresponding to the damage created by 10^{14}, 10^{15} and 10^{16} cm^{-3} 1 MeV P ion implants at the same temperature 45

3.4. X-ray rocking curves from InP implanted with various ions at 200°C to a dose of 10^{16} cm^{-2}.1 MeV P (a), 2MeV As (b), 2.1 MeV Ga (c) and 3.3 MeV In (d) 45

3.5. DCXRD spectra for (a) 2 MeV As and (b) 3.3 MeV In ion implanted InP at 200°C to a dose of 10^{16} cm^{-2} as a function of etch depth 47

3.6. Cross sectional TEM images of As ion as-implanted (a) and annealed (b), Ga ion as-implanted (c) and annealed (d), and In ion as-implanted (e) and annealed (f) semi-insulating InP 48

3.7. Effective mobility μ_{eff} (a), sheet carrier concentration C_s (b) and sheet resistance R_s (c) as determined by Hall measurements and as a function of 1 MeV P ion dose for P ion and 3.3 MeV In ion implants at 200°C into SI InP. In ion doses calculated to give equivalent levels of damage causes by P ion implants are also shown 51

3.8. Mobility (a), sheet carrier concentration (b) and sheet resistance (c) as a function of annealing temperature, for P, As, Ga and In ion implanted SI InP 55

3.9. Ga ion implanted InP annealed at 600°C: (a) Representative SCM (dC/dV mode) imageand (b) Representative SSRM image 57

3.10. SSRM and SCM line scans obtained for the P ion implanted InP samples annealed at 400°C, 500°C and 600°C. (a) SSRM resistance profiles. (b) SCM profiles (dC/dV mode) 59

3.11. SSRM and SCM line scans obtained for the Ga ion implanted InP samples annealed at 400°C, 500°C and 600°C. (a) SSRM resistance profiles. (b) SCM profiles (dC/dV mode) 59

3.12. SSRM and SCM line scans obtained for the As ion implanted InP samples annealed at 400°C, 500°C and 600°C. (a) SSRM resistance profiles. (b) SCM profiles (dC/dV mode) 60

3.13. SSRM and SCM line scans obtained for the In implanted InP samples annealed at 400°C, 500°C and 600°C. (a) SSRM resistance profiles. (b) SCM profiles (dC/dV mode) 60

3.14. Plot of time resolved photoluminescence decay times for p-InP ($\sim 3.4 \times 10^{17}$ cm^{-3}) implanted with different doses of 1 MeV P ions at 200°C 65

3.15. TRPL decay times measured at 300 K and simulated peak atomic displacements (TRIM) produced for P, As, Ga and In ion implanted SI InP 67

3.16. dR/R signals of P ion implanted (a), and As ion implanted (b) samples annealed at 700°C 67

4.1. (a) Dose dependence of sheet resistance of p-InGaAs samples, irradiated with 2 MeV C, 2 MeV O, 0.7 MeV Li and 0.6 MeV H ions. (b) The estimated vacancies/ion/cm calculated using TRIM vs critical dose obtained from data in (a), with a linear best fit 78

4.2. (a) Dose dependence of sheet resistance of p-InGaAs samples with different initial free electron carrier concentrations, irradiated with 2 MeV O ions. (b) Original free carrier concentration of the samples vs critical dose obtained from data in (a), as well as for similar implants done with 2 MeV C, 2 MeV O 0.7 MeV Li and 0.6 MeV H ions (including linear fits) 79

4.3. Isochronal annealing stability of sheet resistance for p-InGaAs ($p \sim 8 \times 10^{17}$ cm^{-3}) epilayers implanted at a range of doses above and below D_{Cr} for (a) 2 MeV O, (b) 2 MeV C, (c) 0.7 MeV Li, and (d) 0.6 MeV H ion implantation 82

4.4. (a) Dose dependence of sheet resistance of n-InGaAs samples, irradiated with 2 MeV C, 2 MeV O, 0.7 MeV Li and 0.6 MeV H ions. (b) The estimated vacancies/ion/cm

calculated using TRIM vs critical dose obtained from data in (a), with a linear best fit ... 85

4.5. (a) Dose dependence of sheet resistance of n-InGaAs samples with different initial free electron carrier concentrations, irradiated with 2 MeV C ions. (b) Original free carrier concentration of the samples vs threshold dose obtained from data in (a) 86

4.6. Isochronal annealing stability of sheet resistance for n-InGaAs ($n \sim 2.7 \times 10^{17}$ cm^{-3}) epilayers implanted at a range of doses above and below D_{Cr} for (a) 2 MeV O, (b) 2 MeV C, (c) 0.7 MeV Li, and (d) 0.6 MeV H ion implantation ... 87

5.1. Effective mobility, μ_{eff}, sheet carrier concentration, N_s and sheet resistance R_s as a function of dose for 2 MeV Fe ion implantation into SI InP at 200°C, as determined by Hall effect measurements ... 96

5.2. X-ray rocking curves as a function of dose for 2 MeV Fe ion implantation ... 97

5.3. XTEM of Fe ion implanted InP to doses of 10^{14} and 10^{16} cm^{-2} at 200°C ... 98

5.4. Dependence of effective mobility (a), sheet carrier concentration (b) and sheet resistance (c) on annealing temperature for SI InP samples implanted with 2 MeV Fe ions ... 99

5.5. Photoluminescence transients for Fe ion implanted InP (dose: 10^{14} cm^{-2}) annealed at different temperatures ... 100

5.6. Arrhenius plot of the inverse PL decay time For Fe ion implanted and annealed InP layers (circles). The squares show the data for the P ion implanted samples suggesting a similar slope to that of InP:Fe ... 102

5.7. Mobility (a), sheet carrier concentration (b) and sheet resistance (c) as a function of P ion implant dose, for *p*-type InP with hole concentrations ~3.4 x 10^{17} and ~1.3 x 10^{18} cm^{-3} 106

5.8. Effective mobility (a), sheet carrier concentration (b) and sheet resistance (c) as a function of implantation dose for *p*-type InP implanted with 1 MeV P ions and annealed at 500 and 600 °C, respectively 107

5.9. PL decay times for P ion implanted InP samples annealed at 500 and 600°C as a function of implantation dose 108

6.1. Effective mobility, μ_{eff}, sheet carrier concentration, N_s, and sheet resistance, R_s, for both room temperature and 200°C 2 MeV Fe ion implantation as a function of dose 117

6.2. DCXRD of an unimplanted 1.5 μm InGaAs epilayer grown on a SI InP substrate 119

6.3. Evolution of X-ray rocking curves as a function of dose for room temperature implantation of InGaAs epilayers with 2 MeV Fe ions 119

6.4. XTEM scans for InGaAs epilayers on InP, implanted with 2 MeV Fe ions at room temperature to 10^{16} cm^{-} 121

6.5. DCXRD of InGaAs implanted to 10^{16} cm^{-2} at room temperature with 2 MeV Fe ions and annealed at temperatures between 500°C and 900°C 122

6.6. XTEM image for InGaAs epilayers on InP implanted with 2 MeV Fe ions at room temperature to 10^{16} cm^{-2} 122

6.7. Evolution of DCXRD spectra as a function of dose for 200°C implantation with 2 MeV Fe ions 123

6.8. XTEM images for InGaAs epilayers on InP, (a) and (b) implanted with 2 MeV Fe ions 200°C to 10^{15} cm^{-2}, and (c) and (d) to 10^{16} cm^{-2} 124

6.9. DCXRD of InGaAs implanted to 10^{16} cm^{-2} at 200°C with 2 MeV Fe ions and annealed at temperatures between 500°C and 900°C 126

6.10. XTEM images for InGaAs epilayers on InP, implanted with 2 MeV Fe ion 200°C to 10^{16} cm^{-2}, and annealed at 800°C for 30 seconds 126

6.11. Effective mobility, μ_{eff}, and sheet resistance R_s for room temperature 2 MeV Fe ion implantation as a function of annealing temperature for 10^{15} and 10^{16} cm^{-2} 128

6.12. (a) Measured and simulated TRPL traces from annealed InGaAs samples implanted at room temperature with a dose of 10^{15}cm^{-2}. (b) Differential reflectivity measurements of the same samples excited with band gap energy photons 131

6.13. Effective mobility, μ_{eff}, sheet carrier concentration, N_s and sheet resistance R_s for *p* -InGaAs implanted at room temperature with 1 MeV P ions as a function of dose and for annealing at 500°C and 600°C for 60 seconds 135

6.14. X-ray rocking curves of room temperature 1 MeV P ion implanted *p* -InGaAs to a dose of 10^{16} cm^{-2} as a function of annealing temperature 136

6.15. Evolution of X-ray rocking curves for room temperature 1 MeV P ion implanted *p* -InGaAs as a function of dose for (a) 500°C and (b) 600°C annealing for 60 seconds 136

7.1. Schematic of quantum well interdiffusion 143

7.2. Schematic of quantum well epitaxial structures used in the study 146

7.3. Vacancies produced by implanting into InGaAs epilayers on InP as a function of depth, calculated by TRIM 147

7.4. Schematic of quantum well interdiffusion induced by ion implantation (low and high energy cases depicted) 147

7.5. 77K photoluminescence peak energy of InP/InGaAs quantum wells (with InP or InGaAs cap) and InGaAs/AlGaInAs quantum wells (with InP or InGaAs cap) as a function of annealing temperature 149

7.6. Low temperature (77K) photoluminescence spectra from InP/InGaAs quantum well structure implanted at room temperature with 20 keV P ions to various doses and rapid thermally annealed at 700°C for 60 seconds 151

7.7. Energy shift of InP capped InP/InGaAs quantum wells as a function of dose for 20 keV P ion cap implants at both room temperature and 200°C 152

7.8. Energy shift of InGaAs capped InP/InGaAs quantum wells as a function of dose for 20 keV P ion cap implants at both room temperature and 200°C 152

7.9. Glancing angle RBS-C spectra for the InP capped sample, implanted with 20 keV P ions to a dose of $10^{14}cm^{-2}$ at room temperature and 200°C 153

7.10. Glancing angle RBS-C spectra for the InGaAs capped sample, implanted with 20 keV P ions to a dose of 10^{13} and $10^{14}cm^{-2}$ at room temperature and 200°C 153

7.11. Energy shift of InP capped InGaAs/AlGaInAs quantum wells as a function of dose for 20 keV P ion cap implants at both room temperature and 200°C 157

7.12. Energy shift of InGaAs capped InGaAs/AlGaInAs quantum wells as a function of dose for 20 keV P ion cap implants at both room temperature and 200°C 157

7.13. Energy shifts of InGaAs/AlInGaAs quantum wells as a function of dose for 20 keV P ion cap implants at room temperature, for different annealing temperatures and cap layers 159

7.14. Energy shifts of InGaAs/AlInGaAs quantum wells as a function of dose for 20 keV P ion cap implants at 200°C, for different annealing temperatures and cap layers ... 159

7.15. Energy shift as a function of dose for all quantum well samples after implants with 1 MeV P ions at 200°C and annealing at 700°C for two 60 second intervals ... 162

8.1. Schematic of interdiffusion induced by impurity free vacancy disordering ... 169

8.2. Ground state (electron-heavy hole) transition energy variation with interdiffusion, for various values of k = group V/group III diffusion rates ... 171

8.3. Schematic illustrating concepts for 'single layer' and 'bilayer' impurity free vacancy disordering ... 172

8.4. 77K photoluminescence spectra of InGaAs capped InP/InGaAs quantum wells for PECVD of 60 nm SiO_2 ... 175

8.5. Photoluminescence shifts as a result of SiO_2/SiN_x bilayer dielectric treatment of the InGaAs capped InP/InGaAs quantum wells, with the SiO_2 thickness varying between 50 and 700 Å and an overlayer thickness of ~200nm, after annealing at 800°C for 60s. a) Photoluminescence spectra at 77K, b) Energy shifts as a function of SiO_2 thickness ... 183

8.6. Photoluminescence shifts as a result of SiO_2/TiO_2 bilayer treatment of InGaAs capped InP/InGaAs quantum wells, with the SiO_2 thickness varying between 5 and 70 nm and an overlayer thickness of ~ 200 nm, after annealing at 800°C for 60s. a) Photoluminescence spectra at 77K, b) Energy shifts as a function of SiO_2 thickness ... 185

8.7. Photoluminescence shifts of InGaAs capped InP/InGaAs quantum wells coated with an undoped, Ga-, P- and T- doped spin-on glasses ... 187

8.8. XPS in-depth profiles of InGaAs capped InP/InGaAs quantum wells treated with an undoped SOG 189

List of Tables

8.1 Thermal expansion coefficents for InGaAs, InP and GaAs and various dielectrics 179

8.2 Photoluminescence energy shifts (in meV) for 200 nm PECVD deposited SiO_2, SiN_x and TiO_2 single layers on InGaAs quantum well samples 179

Table of Acronyms

DCXRD	Double crystal x-ray diffractometry
k	ratio of gpV to gp III diffusion lengths
MOCVD	Metalorganic chemical vapor deposition
μ_{eff}	Effective mobility
N_s	Sheet carrier concentration
PECVD	Plasma enhanced chemical vapor deposition
PL	Photoluminescence
QW	Quantum well
RBS-C	Rutherford backscattering-channeling spectrometry
R_s	Sheet resistance
RTA	Rapid thermal annealing
SCM	Scanning capacitance microscopy
SSRM	Scanning spreading resistance microscopy
SOG	Spin-on glass
TRDR	Time resolved differential reflectance
TRPL	Time resolved photoluminescence
XPS	X-ray photoelectron spectroscopy
XTEM	Cross-sectional transmission electron microscopy

Publications related to this thesis

Journals

1. *A comparison of impurity-free and ion-implantation-induced intermixing of InGaAs/InP quantum wells*, L. V. Dao, M. Gal, C. Carmody, H. H. Tan, and C. Jagadish, J. Appl. Phys. **88**, 5252 (2000)
2. *Ultrafast trapping times in ion implanted InP*, C. Carmody, H. Boudinov, H. H. Tan, C. Jagadish, M. J. Lederer, V. Kolev, B. Luther-Davies, L. V. Dao, and M. Gal, J. Appl. Phys. **92**, 2420 (2002)
3. *Thermoluminescence in ion-implanted GaAs*, M. Gal, L.V. Dao, E. Kraft, M.B. Johnston, C. Carmody, H.H. Tan and C. Jagadish, J. Luminescence, 96, 287-293 (2002).
4. *Influence of cap layer on implantation induced interdiffusion in InP/InGaAs quantum wells*, C. Carmody, H. H. Tan, and C. Jagadish, J. Appl. Phys. **93**, 4468 (2003)
5. *Ultrafast carrier trapping and recombination in highly resistive ion implanted InP*, C. Carmody, H. H. Tan, C. Jagadish, A. Gaarder and S. Marcinkevicius, J. Appl. Phys, **94** (2003)
6. *Ion Implanted $In_{0.53}Ga_{0.47}As$ for ultrafast optoelectronic applications*, C. Carmody, H. H. Tan, C. Jagadish, A. Gaarder, and S. Marcinkevičius, Appl. Phys. Lett., **82**, 3913 (2003)
7. *Structural, Electrical and Optical analysis of ion implanted semi insulating InP*, C. Carmody, H. H. Tan, C. Jagadish, O. Douhéret, K. Maknys and S. Anand, J. Zou, L. Dao and M. Gal., submitted to J. Appl. Phys. (2003)
8. *Electrical isolation of n - and p - $In_{0.53}Ga_{0.47}As$ epilayers using ion irradiation*, C. Carmody, H. H. Tan, and C. Jagadish, submitted to J. Appl. Phys. (2003)

Conference Proceedings

1. *Electrical and optical properties of MeV As and P ion implanted and annealed Indium Phosphide*, C. Carmody, H. Boudinov, H. H. Tan, C. Jagadish, M. J. Lederer, V. Kolev and B. Luther-Davies, Proceedings of 2000 IEEE Semiconducting and Insulating Materials Conference, IEEE Publishing Co., Piscataway, NJ, 137 (2000)
2. *Use of ion-implantation for the creation of ultrafast photodetector materials and tuning of quantum well infrared photodetectors*, H. H. Tan, L. Fu, C.Y. Carmody and C. Jagadish, Proceedings of SPIE Conference on Photodetectors: Materials and Devices VI, SPIE, San Jose, 47 (2001)
3. *Ion-implanted InP for ultrafast photodetector applications*, C. Carmody, H. Boudinov, H. H. Tan, C. Jagadish, L.V. Dao and M. Gal, Proceedings of 2000 Conference on Optoelectronics and Microelectronics Materials and Devices, IEEE Publishing Co. 153 (2001)
4. *Influence of cap layer on interdiffusion in InP/InGaAs quantum wells*, C. Carmody, H. H. Tan , and C. Jagadish, Proceedings of 15th Annual Meeting of the IEEE Lasers and Electro-Optics Society, **2** , 845 (2002)
5. *Evolution Of InGaAs/InP Quantum Well Intermixing As A Function Of Cap Layer*, C. Carmody, H. H. Tan, C. Jagadish, Proceedings of 2002 Conference on Optoelectronics and Microelectronics Materials and Devices, IEEE Publishing Co. (In press)
6. *Structural, Electrical And Optical Properties Of Mev As^+ Ion Implanted InP*, C. Carmody, H. H. Tan, C. Jagadish, J. Zou, L. Dao, M. Gal, Proceedings of 2002 Conference on Optoelectronics and Microelectronics Materials and Devices, IEEE Publishing Co. (In press)
7. *Ultrafast carrier trapping in high energy ion implanted indium phosphide*, C. Carmody, H. Boudinov, H. H. Tan, C. Jagadish, L.V Dao and M. Gal, Proceedings of 2000 IEEE Semiconducting

and Insulating Materials Conference, Bratislava, Slovakia, June 2002, IEEE Publishing Co. (In press).

CHAPTER 1

Introduction

Recent developments in III/V compound semiconductors have led to a revolution in fast optical communications systems; new optoelectronic devices such as lasers, modulators and photodetectors based on InP and InGaAs are widely used in both long and short haul communications networks. In these networks, of particular importance is the demand for faster data transmission rates, which are needed for a range of applications such as broad band internet and video on demand, and which require devices which can operate at much faster rates. In order to meet this demand, two main technologies have been proposed; one is based on optical time domain multiplexing, and the other on wavelength division multiplexing. The former technology achieves increased data transmission rates by sending and receiving the optical signals at higher frequencies. The latter produces the same effect by sending data at a slower rate, but over a range of wavelengths. The studies in this Thesis address both these technologies, using ion implantation and bandgap tuning techniques.

Although it may defy common sense, adding imperfections to semiconductors can actually improve their performance in devices used for everything from information technology to playing music. Creating defects on purpose (defect engineering)- or putting naturally occurring defects to good use - can have major implications for the future of optoelectronics and materials science.

Of the III/V semiconductors, InP and InGaAs are preferred for long - wavelength optoelectronic applications. Moreover, it is logical to study these materials in conjunction, since InGaAs layers are inevitably grown lattice matched to InP substrates. At room temperature, and with InGaAs lattice matched to InP (corresponding to a lattice spacing of ~ 5.87 Å) their bandgaps are ~ 1.35 and 0.78 eV, respectively. This

translates to emission/detection wavelengths of ~ 0.9 and 1.6 μm. Apart from the epitaxial layers, heterostructures can be made from these semiconductors with emission/detection wavelengths in the highly desirable 1.3 and 1.55 μm range, which is the operating wavelength used in long haul optical fibre communications.

The study into defects in InP and InGaAs offered here represents a contribution to the ongoing efforts into uncovering new ways of controlling, or even exploiting, these defects for optoelectronic device applications. The defects were created primarily by ion implantation, while a small section of work deals with defect injection via deposition of dielectric layers on the surface of samples. There are two main directions this work has taken. Firstly, the defects created by ion implantation are studied as causes of electrical and optical characteristics which, in bulk InP and InGaAs, could be very useful in fabricating devices with very fast optical response times that could be employed in increased bandwidth optical fibre communications, not to mention ultrafast long wavelength spectroscopic techniques. When a crystalline semiconductor is ion implanted, the incoming charged atom undergoes a series of collisions with elements in the target, causing cascades of 'knock on' collisions which dislodge target atoms from their usual lattice positions. As such, these 'out of place' atoms are defects which bond with the surrounding atoms in a variety of ways, existing as simple *point defects* such as vacancies, interstitials or antisites, or forming more complex clusters, loops, stacking faults or voids. Each of these defects have their own optical and electrical characteristics - they may act as carrier traps or donate excess carriers to the semiconductor - with energy levels that can exist in the valence or conduction band or within the band gap. Thus, they locally vary the electrical and optical characteristics of the material. Locally,

also, they induce strain into the matrix due to deviations from the usual lattice configuration. In large enough concentrations, they can vary these characteristics enough to modify the properties of an entire sample and be observable in optical and electrical experiments and also experiments which reveal the structural integrity of the material.

Secondly, the defects in these materials are used to drive a process called *interdiffusion* in InP and InGaAs based quantum wells, which means an exchange of elements at InP/InGaAs interfaces. This is a method which has been used to 'tune' emission/detection wavelengths in lasers and photodetectors made out of quantum semiconductor structures, and has been investigated for monolithic integration of optoelectronic devices. Point defects mentioned above are ideal for interdiffusion, since they are highly mobile in the semiconductor at elevated temperatures, and can diffuse large distances within a sample. In this way, they promote an exchange of elements across interfaces between two semiconductors. In the case of quantum wells, this results in a smoothing of the semiconductor composition across what was initially an abrupt interface, which also causes a smooth variation in bandgap where previously there was a sharp step between the adjacent materials. Thus, the sharp square potential of a quantum well can be modified, which leads to changes in the energy levels within the quantum well, and ultimately its emission/detection wavelength.

Chapter 2 discusses the various methods which were used to fabricate and modify samples, as well as the experimental techniques employed to assess the changes to the electrical, optical and structural properties of the material. Chapter 3 presents detailed investigations into the properties of ion implanted semi-insulating InP, and raises principal issues which are essential for interpretation of results in later Chapters. Chapter

4 discusses similar studies into the electrical properties of ion implanted InGaAs epilayers grown on InP substrates, and focuses in particular on methods of achieving electrical isolation in this material using the damage caused by the implantations. In these two chapters, the similarities as well as the differences of defective InP and InGaAs become apparent. Efforts to modify the properties of these materials are then described in the following Chapters. Chapter 5 looks at methods of obtaining implanted InP suitable for ultrafast optoelectronic applications, and Chapter 6 details similar studies using epitaxial InGaAs. In Chapter 7 and 8, the defects are put to a different use in promoting interdiffusion studies in InP/InGaAs and InGaAs/AlGaInAs quantum well structures. In the former Chapter, interdiffusion is driven by defects resulting from ion implantation, and in the latter, dielectric layer deposition is investigated as an equally powerful means for achieving tuning of emission/detection wavelengths of quantum structures made from InP and InGaAs. Finally, Chapter 9 details the main conclusions, and provides suggestions for further work.

CHAPTER 2

Experimental Techniques

2.1 Introduction

The experimental techniques used for both fabrication and analysis of samples studied in this Thesis will be presented here. Descriptions are restricted to providing a basic understanding of the methods and equipment employed, since a more comprehensive picture is best sought in the references provided at the end of this Chapter. Issues relating to each technique that are of particular interest to this Thesis will be covered in more detail in the appropriate sections. The main techniques have been categorized as follows

- Epitaxial growth (sample fabrication)
- Ion implantation and sample processing (sample modification)
- Material characterization (structural, electrical and optical analysis of samples)

2.2 Epitaxial Growth

The InP and InGaAs epilayers as well as quantum well structures used in this work were all grown by metalorganic chemical vapour deposition (MOCVD). MOCVD is a thin film deposition process using a vapour phase reaction between metalorganic compounds of the group III elements and hydrides of the group V elements; a detailed description of the processes involved can be found in several good books and reviews[1-4]. All samples were grown at the Australian National University using an AIXTRON AIX 200/4 horizontal flow (with rotation) reactor. The growth temperature was 650°C, pressure was 180 mb, and the semiconductor structures were all grown on (100) InP substrates supplied by American Xtal

Technology. *P*-type as well as *n*-type InP and InGaAs epilayers were grown by doping with Zn and Si, respectively. InGaAs was always grown with a nominal In composition of 53% and Ga composition of 47% such that the epilayers were lattice matched to the InP substrates. AlInGaAs used in quantum well structures in Chapter 7 used an Al composition of 20%, Ga composition of 27% and In composition of 53% for the same reason.

A summary of the structures used in this work is as follows:

Chapter 3:	InP semi-insulating (SI) substrates; undoped InP epilayers on n^+InP substrates; *p*- InP epilayers on SI substrates.
Chapter 4:	*n*- and *p*- type InGaAs epilayers
Chapter 5:	InP SI and *p*- type epilayers
Chapter 6:	undoped and *p*- type InGaAs epilayers
Chapter 7:	InP/InGaAs quantum wells with InP or InGaAs capping layers; AlGaInAs/InGaAs quantum wells with the same capping layers
Chapter 8:	InP/InGaAs quantum wells with InGaAs capping layers

More detailed descriptions of the samples are provided in the experimental section of each Chapter.

2.3 Sample Processing

2.3.1 Ion Implantation

Theory

Ion implantation[5-7] involves the irradiation of samples with ionized atoms (i.e. ions) which can be accelerated to energies from a few keV to several MeV. Such energetic ions, upon impact, lose their energy via a series of collisions with target nuclei and electrons. These collisions can result in displacements of atoms in the target, leaving lattice defects in crystalline solids. Such defects constitute the main focus of this work.

Ion ranges and atomic displacements produced by ion implantation can be calculated using Transport of Ions in Matter (TRIM) monte carlo simulations[8]. Implantation produces Gaussian-like (unimodal) damage (atomic displacement) profiles, as shown in Figure 2.1. The thickness of the layer altered by the implantation as well as the number of atomic displacements generated depends on ion mass and energy. Generally speaking, the greater the ion mass, the more damage is created. The TRIM code takes into account only ballistic processes and ignores effects such as *dynamic annealing* (defect migration and interaction processes). Moreover, this code does not have any scope for predicting the damage profiles

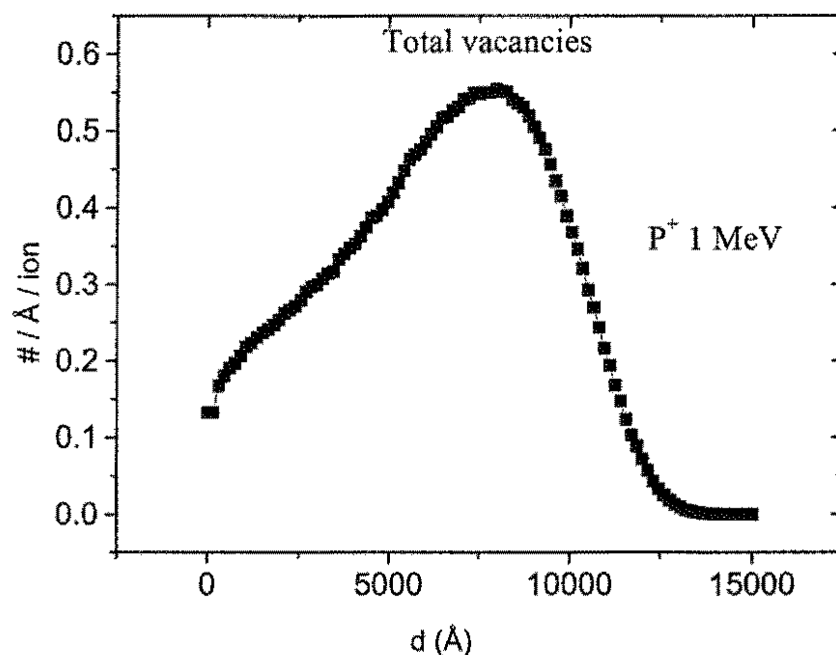

Figure 2.1 Profile of In vacancies as a function of depth for 1 MeV P^+ implantation into InP, as simulated by TRIM.

when implants are done at temperatures other than room temperature. Thus, actual damage caused in the sample by implantation must be verified experimentally. However, we have found that the depth of the maximum damage predicted by TRIM corresponds well to the values measured for implants into InP and InGaAs at elevated temperatures.

Experimental Details

In this work, ion implantation was performed on both the low and high energy ion implanters. Figure 2.2 shows a schematic of the ANU 1.7 MV tandem accelerator (NEC, 5SDH-4) used for high energy implants. Samples were mounted on the target holder in the implant chamber using metal clips. The ion source is a SNICS - type, (Source of Negative Ions by Cesium Sputtering) where a stream of Cs vapour is ionised into Cs^+ which are then attracted to a negatively biased cathode ($\leq$ 10 kV). The ions to be implanted are normally obtained from a powder source which is pressed into a Cu cathode. The list below shows (in order of increasing atomic mass) the source materials for the various ion species used.

Ions	*Atomic Mass (a.m.u)*[9]	*Source Material*
H	1.00	TiH_2 powder
Li	6.94	LiOH powder
C	12.01	Carbon powder
O	16.00	Al_2O_3 powder
P	30.97	Crushed InP wafer
Fe	55.85	Solid machined steel cathode
Ga	69.72	Ga_2O_3 powder
As	74.92	Crushed GaAs wafer
In	114.82	In_2O_3 powder

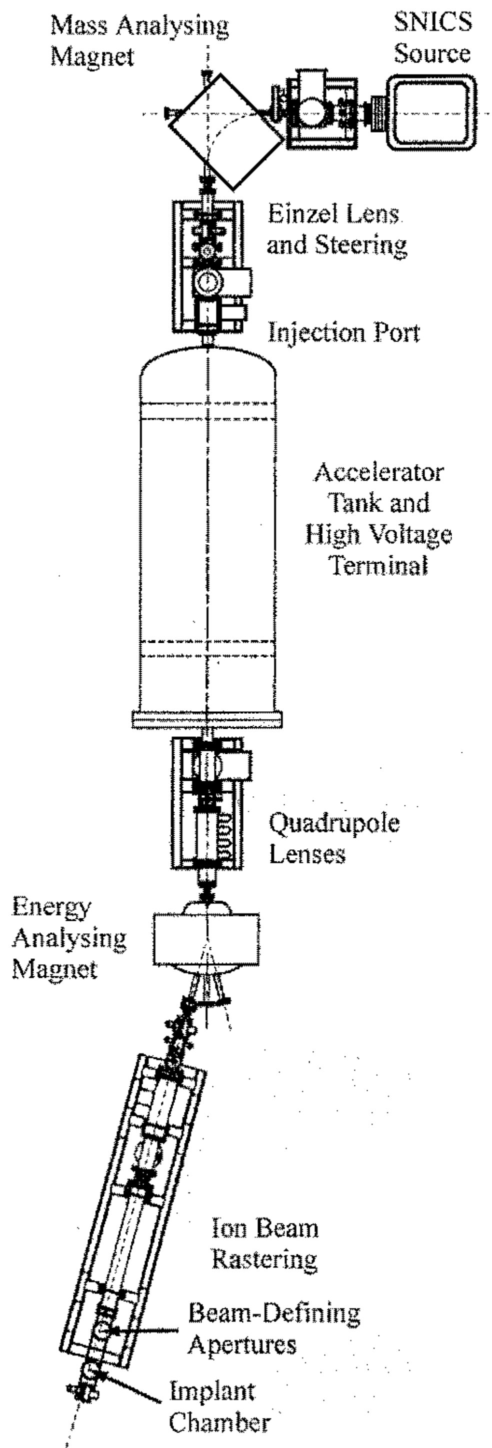

Figure 2.2 Schematic of the 1.7 MV tandem ion accelerator used for high energy ion implantation.

The positively-biased extractor ($\leq$ 15 kV) then attracts the sputtered negative ions, accelerating them further by a bias ($\leq$80 kV) into a 90° magnet, with a path radius R, for mass-filtering. By setting the magnetic field such that the magnetic force acting on the accelerating ions is equal to the centripetal force of the ions as they are deflected through a radius (R), the required ions with mass (m) and charge (n) will be singled out by being deflected towards the high voltage terminal, i.e.

$$B = 1/R\sqrt{2mV_i / qn} \qquad [2.1]$$

where B is the magnetic field, V_i is the potential of the ions and q is the electronic charge.

The high voltage terminal resides in the middle of a tank containing pressurised SF_6 gas for insulation purposes. Positive charge (up to 1.7 MV) is supplied to the terminal by two pelletron chains. The voltage applied to the high voltage terminal is sustained through a series of equi-potential rings separated by resistors, as the beam path at the two ends of the tank are kept at ground potential. The voltage stability of the terminal is ensured using a set of corona points which form a closed loop feedback system. The mass-filtered negative ions coming from the 90° magnet are electrostatically steered into the tank and accelerated towards the positive high voltage terminal. At this terminal, they are partially stripped of electrons in a nitrogen charge-exchange cell to become positive ions and as a result are further accelerated towards the other end of the tank (at ground potential). Thus, the final energy, V_f, of the ions is

$$V_f = q\,[V_i + (1+n)\,V_t] \qquad [2.2]$$

where V_t is the voltage at the terminal, V_i is the injected potential of the ions and n is the charge state of the ions. Typically, the final ion energy is in the range 0.2 - 10 MeV. If lower energies are required ($\leq$ 150 keV), the low energy ion implanter is used, which operates on a similar principle to the source end of the high energy implanter.

2.3.2 Rapid Thermal Annealing (RTA)

Rapid thermal annealing[10] is a crucial step in preparing samples for all aspects of this work. By annealing at different temperatures and times one can learn a great deal about the thermal stability and mobility of defects in semiconductors. Besides, high temperature process steps are part and parcel of the device fabrication techniques, and so were used routinely in this work. Annealing steps were also used to promote interdiffusion and damage removal. All the RTA processes were performed in an Ar ambient with temperature ramping at 100°C/s, were done in the proximity geometry, where samples were covered with sacrificial material to minimize material decomposition. For example, P has a strong tendency to evaporate from InP at annealing temperatures above 400°C, thus it is necessary to use sacrificial pieces of InP to maintain the P vapour pressure at the surface. Where InGaAs surfaces were concerned, sacrificial GaAs was used to prevent excess loss of As.

2.3.3 Plasma Enhanced Chemical Vapor Deposition (PECVD)

It was necessary to deposit dielectric layers of SiO_2 and/or SiN_x for the intermixing studies (impurity free vacancy disordering) in Chapter 8. This was done using an Oxford Plasmalab 80 Plus plasma enhanced chemical vapour deposition (PECVD) system.

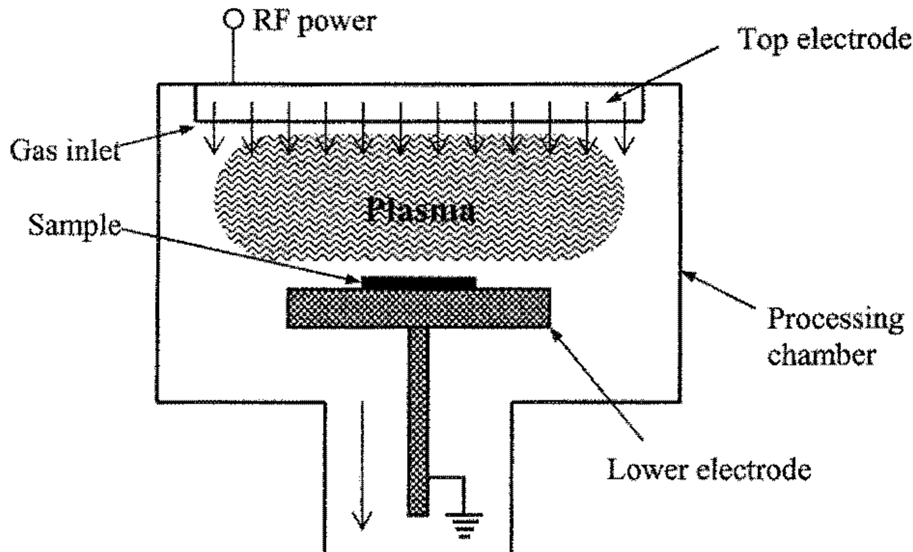

Figure 2.3 Configuration of the PECVD system. Courtesy of Dr. L. Fu.

PECVD uses the principle of nonequilibrium glow discharge[11], which is defined as a partially ionized gas containing equal volume concentrations of positively and negatively charged particles (mostly ions and electrons, respectively) existing in different concentrations of ground-state and excited states[12]. Nonequilibrium glow discharges are generated by subjecting the gas to a radio frequency (RF) electric field. The small concentration of free electrons initially present in the gas are accelerated by this electric field. At sufficiently high energies, the electron collisions with atoms in the gas excite and ionize them, in the latter case creating additional electrons which are also accelerated by the electric field. In this way an avalanche of accelerated electrons creates a steady state glow discharge. At steady state, a fraction of the ground-state parent atoms in the gas phase undergoes electron impact dissociation and excitation such that highly reactive species are created, which in turn diffuse towards the sample, adsorb on contact with the surface, undergo chemical reaction and surface

migration, and eventually form a solid film. Since the reactive species produced in the plasma have lower energy barriers to physical and chemical reactions than the parent species, they can react at lower temperatures, which is the major advantage of PECVD compared with other thin film deposition techniques.

The plasma is generated between two parallel, circular electrodes, with the sample being placed on the lower, electrically grounded electrode. The upper electrode is connected to a 13.56 MHz RF generator and the reactants (SiH_4, NH_3 and N_2O gases) are fed in from the gas inlet through the top electrode, entering the plasma region. The gases used were 5% silane (in N_2) and nitrous oxide for SiO_2 deposition and 5% silane (in N_2) and ammonia for SiN_x deposition.

2.3.4 Electron Beam Evaporation

Another method of forming films on the surface of samples is by electron beam evaporation. In this case, the heating of the material to be deposited is done using a focused beam of electrons, which has the advantage of being able to heat to very high temperatures a small region of the source material to such high temperatures that it evaporates. The material then recondenses on all the surfaces of the evaporation chamber, including on exposed samples.TiO_2, a dielectric used for interdiffusion studies in Chapter 8, was evaporated onto samples via this technique using a Temescal CV-8 electron beam evaporator.

2.3.5 Spin-on Glasses (SOGs)

Spin on glasses are another form of silica which can be deposited on the surface of samples. In this case the silica is initially suspended in a solvent, and the resulting solution spun onto the

sample using standard spin deposition techniques. Then the sample is baked for a reasonable time (such as 15 minutes) so that the solvent evaporates, leaving behind the amorphous silica. Different baking temperatures result in a different quality (e.g. porosity) of the silica. In this work, spin on glasses were used in addition to the other dielectric deposition techniques to promote interdiffusion in the quantum well samples. Undoped as well as P -, Ga - and Ti - doped spin on glasses were used.

2.4 Material Characterisation

2.4.1 Double Crystal X-ray Diffractometry (DCXRD)

DCXRD is a non-destructive technique widely used for measurements of compositions, layer thickness and strain in epitaxial structures[13,14]. In this work its use has primarily been to gauge the strain profile introduced into epilayers as a result of ion implantation. A Bede QC2a diffractometer was used, where a beam of Cu K_{α} X-rays is collimated to a reference crystal of the same material and orientation as the specimen which also acts as a monochromator. When the planes of the specimens are parallel to those of the reference crystal, Bragg conditions are satisfied, i.e.

$$n\lambda=2d\sin\theta_B \qquad [2.3]$$

where d is the spacing of the Bragg planes, λ is the X-ray wavelength, θ_B is the Bragg angle (31.668° for (004) InP) and n is the order of diffraction (n=1, 2,...). A slit is positioned in front of the detector to limit the angular divergence and improve the resolution. A small

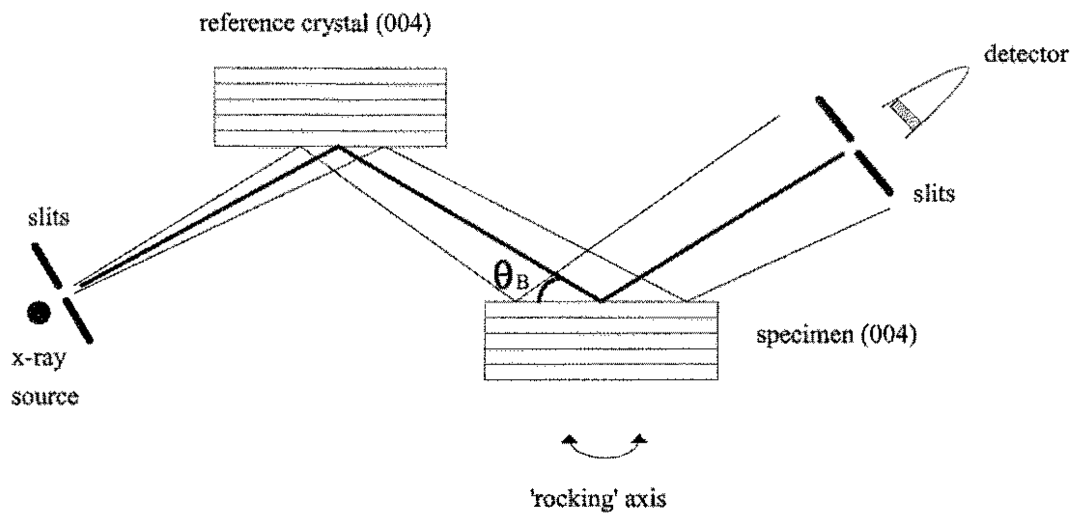

Figure 2.4 Schematic of a double-crystal X-ray diffractometer (DCXRD). Courtesy Dr. H. H. Tan.

rotation of the specimen with respect to the reference crystal will result in a loss of intensity from the substrate. For one of the implanted samples, Dr. Manuela Buda at the Department of Electronic Engineering, ANU, kindly performed modeling using the Takagi-Taupin Theory[15].

2.4.2 Cross- sectional Transmission Electron Microscopy (XTEM)

Cross-sectional transmission electron microscopy (XTEM) is a well established technique to study defects and microstructure of materials. It is routinely used to image and analyse damage and defects in ion implanted materials. An XTEM sample may be investigated in several modes, most commonly the diffraction mode (such as selected area diffraction and convergent beam diffraction) and imaging mode (such as bright-field, dark-field and weak beam imaging). These methods allow a vast array of crystalline defects to be imaged and analysed. Details of the operation of a XTEM and the analysis of the images are beyond the scope of this work but

may be found in several good publications[16-18]. XTEM analyses were carried out by Dr. Zou Jin at the Electron Microscope Unit at the University of Sydney. Samples were prepared by mechanical grinding followed by ion-beam thinning and then examined in a Philips CM 12 operating at 120 kV.

2.4.3 Rutherford Backscattering-Channeling Spectrometry (RBS-C)

Rutherford backscattering spectrometry (RBS) is a quantitative ion beam analysis technique, commonly used to analyse structural damage and composition of target samples. With this technique, a beam of monoenergetic light ions (such as H or He) is bombarded onto the specimen to be analysed. The backscattered ions are then collected and analysed for their energy distribution which will yield information about the atomic constituents and also a depth profile of the target. If the incident ions are aligned along a low index crystallographic direction of a crystalline target (axial channeling), then most of the ions are steered into the 'channels' of the crystal, causing a significantly reduced backscattered ion yield. On the other hand, if the target is randomly oriented with respect to the incident ions, then fewer ions are channeled along the crystallographic axes and more direct scattering will occur. The aligned technique is generally referred to as ion channeling or RBS-channeling (RBS-C). If defects are present in the sample, such as displaced atoms in the channeling paths, then the yield of the backscattered ions will increase. In this way, the channeling spectrum can give a depth and concentration profile of defects present in the material, and is ideal for analysis of crystalline materials such as the semiconductors studied in this work.

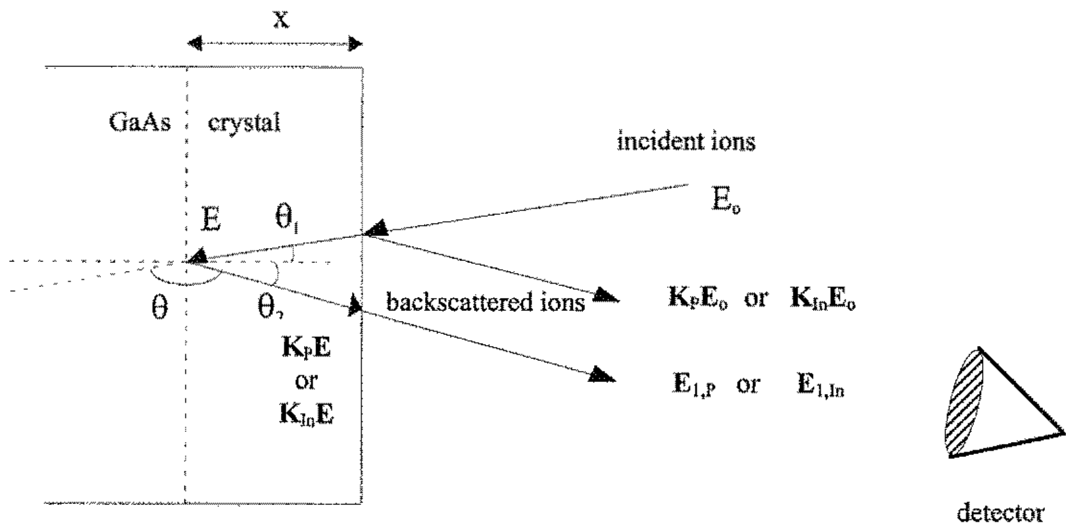

Figure 2.5 Schematic representation of the backscattering process for a specific geometry.

The RBS-C measurements done in this Thesis were conducted on an ANU 1.7 MV tandem accelerator (National Electrostatics Corporation, U.S.A., model 5SDH), which has a similar design to the 1.7 MV implanter depicted in Figure 2.2. In this case, a rubidium ion source is used (not a SNICS) and a high voltage tank with only one nylon chain.

The geometry of the RBS detection system is important in the quantitative analysis of the results, such as the depth profile. The energy loss of an incident ion with energy E_o in traversing a distance x from the surface and backscattered by a P atom is related to the following expression, as illustrated in Figure 2.5

$$\Delta E_P = K_P E_o - E_{1,P} = [S]_P x \qquad [2.4]$$

$$[S]_P = \frac{K_P}{\cos\theta_1}\frac{dE}{dx}\Big|_{in} + \frac{1}{\cos\theta_2}\frac{dE}{dx}\Big|_{out} \qquad [2.5]$$

where K_P is the kinematic factor of P, $E_{1,P}$ is the energy of the ion backscattered off a P atom at x, $[S]_p$ is the energy loss factor of P and $dE/dx|_{in}$ and $dE/dx|_{out}$ are the rate of energy loss evaluated at the inward and outward paths, respectively. For regions near the surface, the depth x is small and hence, the relative change of the ion energy along an incident path is also small. Thus, it is sufficient to use a surface energy approximation which reduces the latter expression to

$$[S]_P = \frac{K_P}{\cos\theta_1}\frac{dE}{dx}\Big|_{E_o} + \frac{1}{\cos\theta_2}\frac{dE}{dx}\Big|_{K_P E_o} \qquad [2.6]$$

Similar expressions are true for an ion scattering off an In atom. Further treatment of RBS and ion channeling can be found in references 19 and 20.

2.4.4 X-ray Photoelectron Spectroscopy

X-ray photoelectron spectroscopy (XPS)[21,22] operates on the principle irradiation of a sample under vacuum with monoenergetic soft X-rays (typically Mg K_α (1253.6 eV) or Al K_α (1486.6 eV) produced by electron bombardment of Mg or Al targets), which interact with the surface atoms such that electrons are emitted by the photoelectric effect. An electron spectrometer collects the photoelectrons and analyses their energy. The kinetic energy of an emitted electron, referenced to an appropriate zero of energy, is related to the binding energy of an

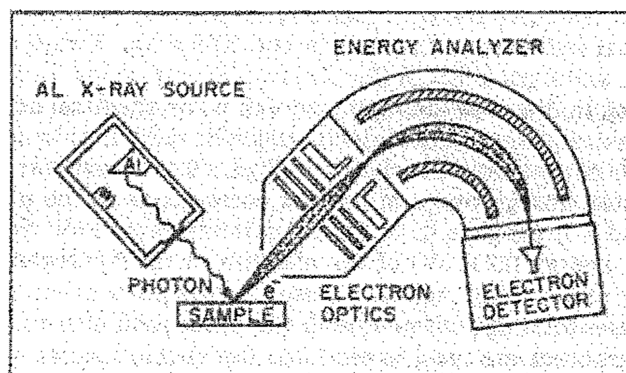

Figure 2.6 Schematic of the basic apparatus used in X-ray photoelectron spectroscopy. X-rays are produced at the Al anode by bombardment of electrons created at the filament. The X-rays impinge on a sample producing photoelectrons which are detected after analysis in the electron energy analyzer.[21]

electron in the target atom. Because each element has a unique set of binding energies, XPS can be used to identify and determine the concentration of elements in the surface. Variations in the elemental binding energies (chemical shifts) are caused by differences in the chemical potential and polarizability of the compounds in the sample, and allow identification of the chemical state of the elements in the sample. Measurements were carried out by Dr. Bill Bin Gong at the University of New South Wales, on a ESCALAB220i-XL (VG Scientific, UK) X-ray photoelectron spectrometer. Standard conditions used a vacuum better than 2×10^{-9} mbar. The source used a monochromated Al K_α beam, with source power 10 kV x 12 mA = 120 W. The spot size was ~0.5 mm across and the pass energy was 100 eV for wide scans and 40 eV for narrow scans (resulting in depth profiles). The Ar ion beam used for sputtering into samples (thus providing depth profiles) had an energy of 5 keV. Samples were analysed as received.

2.4.5 Sheet Resistance

Sheet resistance (R_s) is the resistance between the opposite edges of a square of arbitrary dimensions. Sheet resistance is independent of the size of the square and is determined by material resistivity and sample thickness. Thus, R_s is a property of the sheet. For R_s measurements, rectangular samples were cut from InP and InGaAs-on-InP wafers. On two opposite sides of each sample, ohmic contacts were fabricated. In the case of both InP and InGaAs, it is relatively easy to make ohmic contacts: indium wire is pressed onto the surface and then the sample heated at 200°C until the metal is observed to have melted and oxidized (indicating a reaction with the semiconductor surface). Sheet resistance measurements of ion implanted InGaAs were done *in situ* (without breaking vacuum in the target chamber of the implanter) with a specially designed sample holder. Measurements were performed several minutes after each ion dose had been delivered.

2.4.6 Hall Effect

Hall effect[23], as a characterization tool, has been used throughout the history of semiconductors to provide a direct measure of free carrier type and density, and, when combined with a resistivity measurement on the same sample, carrier mobility. A standard explanation of the physics of the Hall effect uses a uniform bar sample, as shown in Figure 2.6, where positive carriers flow under the influence of an electric field ξ_z along the bar. A uniform magnetic field B_x is applied normal to the top surface, resulting in a force $F_B = eB_xv_z$, which pushes the positive carriers in the positive *y* direction to the edge of the bar, where v_z is the

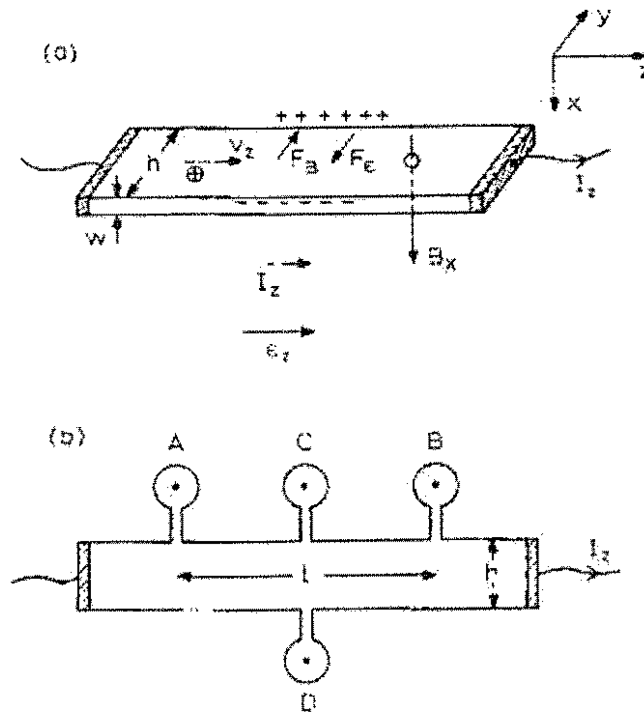

Figure 2.6 Schematic diagram to illustrate the Hall effect on a semiconductor sample in the form of a "Hall bar". In (a) the coordinate system is defined and the forces acting on positive holes which flow from left to right under the influence of an applied electric field ξ_z are shown. The magnetic field B_x is applied normal to the sample surface and to the direction of current flow. In (b) we show the plan view of a practical sample with side arms A and B which are used to measure the applied field ξ_z and C and D which allow measurement of the Hall field ξ_y. Taken from Blood *et al.*[23]

Since the Hall field ξ_y is proportional to both B_x and the current density J_z:

$$-\xi_y = R_H J_z B_x \quad (J_y = 0) \qquad [2.8]$$

which can be rewritten as

$$R_H = \frac{-\xi_y}{B_x J_z} = \frac{v_z}{J_z} = \frac{1}{ne} \quad [2.9]$$

using equations [2.7] and [2.8] as well as the relation J_z =env$_z$. The proportionality constant R_H is known as the Hall coefficient. The Hall mobility μ_H can be expressed as

$$\mu_H = \frac{\sigma}{en} = \frac{R_H}{\rho} = \frac{|V_C - V_D|}{(V_A - V_B)} \cdot \frac{1}{B_x} \cdot \frac{l}{h} \quad [2.10]$$

where the resistivity is $\rho = 1/\sigma$, l and h are the length and width of the bar as shown in Figure 2.6, and V_x is the voltage measured at contact x = A, B, C, or D.

In practice, averages of the voltage differences are obtained for both current directions (when measuring R_H) and magnetic field, in order to minimize errors. Although the bar sample ensures a uniform current distribution and a well-defined electric field, the majority of Hall effect measurements are made in the van der Pauw[24] geometry. Measurements using this configuration require far less geometrical accuracy than in the bar sample. The van der Pauw configuration used in this work, consisting of four ohmic contacts placed in the corners of a ~5 x 5 mm^2 sample is illustrated in Figure 2.7. Van der Pauw published a theorem in 1958 which applies to the measurement of resistivity in a sample of uniform thickness and doping level but otherwise of arbitrary shape, where four contacts A, B, C and D are placed along its edge. The theorem can be expressed in terms of the resistances:

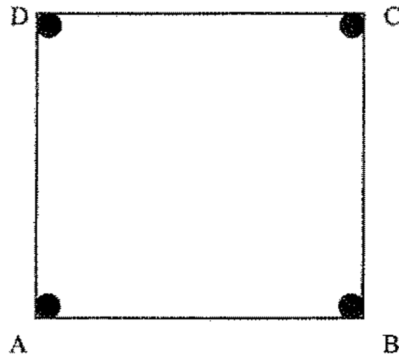

Figure 2.7 Schematic diagram to illustrate the van der Pauw configuration with ohmic contacts A, B, C and D.

$$R_{ABCD} = \frac{V_{AB}}{I_{CD}} \qquad [2.11]$$

where V_{AB} is the voltage measured between contacts A and B when a current I_{CD} is passed between C and D. Van der Pauw also showed that the Hall coefficient is given by:

$$R_H = \frac{W}{B_x} \Delta R_{BDAC} \qquad [2.12]$$

where ΔR_{BDAC} is the change in R_{BDAC} produced by applied magnetic field B_x (R_{BDAC} is measured using diagonal pairs of contacts rather than adjacent pairs). It is standard practice to reverse the current and magnetic field and interchange current and voltage contacts, obtaining the Hall coefficient from an average of eight readings.

2.4.7 Scanning Spreading Resistance Microscopy (SSRM)

Scanning Probe Microscopy based electrical characterisation methods have emerged as promising techniques for two-dimensional mapping of electrical properties at the nanometer scale[25]. Application of Scanning Capacitance Microscopy (SCM) and Scanning Spreading Resistance Microscopy for characterisation of both Si and III-V based materials and devices, has already been reported[26-30]. The obtainable lateral resolution (20-50nm) is typical of probe tips diameter used in Atomic Force Microscopy (AFM). SCM and SSRM are complementary techniques and very well suited to characterisation of electrical properties of ion implanted InP. Particularly, investigation of sample cross-sections provides such information at different locations.

In scanning spreading resistance microscopy[23,31], an electrical resistance is measured between a conductive probe tip and a large current-collecting back contact while the probe is scanned in the contact mode across the cross section of the sample. When the applied force exceeds a certain threshold force, the measured resistance is dominated by the spreading resistance. This resistance R_s, associated with a single probe of contact radius a, results from current crowding close to the contact region in the semiconductor; R_s is therefore determined by the resistivity ρ of a small volume of material within a hemisphere of radius $\sim 2a$. For a plane, uniform contact making perfect ohmic contact at the surface of a semi-infinite semiconductor,

$$R_s = \rho / 4a. \qquad [2.13]$$

In practice, real contacts form a potential barrier R_b at the probe-semiconductor interface, thus

$$R_c = (R_s + R_b) = k\rho/4a, \qquad [2.14]$$

where the factor k is a slowly varying function of ρ which must be calibrated for each individual probe. The spreading resistance depends inverse proportionally on the local carrier concentration underneath the probe-sample contact. The SSRM measurements presented in this work were performed with a Digital Instruments Nanoscope Dim 3100 microscope equipped with a SSRM module by Kestas Mastutis at the Department of Microelectronics and Information Technology, Royal Institute of Technology, Sweden. Commercial Boron-doped diamond coated tips (NanoSensors GmBH) were used. Sample cross-sections were obtained by manual cleaving. The current was measured using a logarithmic amplifier with the dc bias applied to the sample. In this case, the samples consisted of epitaxial InP, about 1.5 μm thick, grown on n^+ InP substrates, which were subsequently implanted with the different ion-species.

2.4.8 Scanning Capacitance Microscopy (SCM)

In a scanning capacitance microscope[31], a tip (such as is used in atomic force microscopy) is covered with a thin dielectric layer such that the tip-sample contact forms a metal-insulator-semiconductor (MIS) capacitor, whose capacitance voltage behaviour is determined by the local carrier concentration in the semiconductor sample. As the probe scans across the sample surface, a 2D carrier concentration profile can be measured. No signal is measured if the

probe is positioned over a dielectric or metallic surface since these regions cannot be depleted. Generally, the tip-sample capacitance is large with respect to the capacitance variations due to different carrier concentrations; thus, capacitance variations are usually measured rather than absolute capacitance values. As for the SSRM measurements, the scanned surface is the cleaved edge of the sample, such that capacitance variations as a function of depth into the samples could be scanned. The SCM measurements presented in this Thesis were carried out with a Digital Instruments Nanoscope Dim 3000 microscope provided with capacitance measurement electronics using commercial Pt-Ir5 coated tips (NanoSensors GmBH) by Olivier Douhéret at the Department of Microelectronics and Information Technology, Royal Institute of Technology, Sweden. The capacitance was measured using a sensor operating at 915 MHz with the tip-sample bias controlled separately by low-frequency ac and dc voltages. As for the SSRM measurements, the sample cross-section was obtained by manual cleaving. The native oxide formed on the cleaved surface by air exposure served as a thin oxide between the tip and the sample.

2.4.9 Photoluminescence (PL)

Photoluminescence[32,33] is a very powerful and non-destructive spectroscopic technique for studying the intrinsic and extrinsic properties of semiconductors. This technique requires only a small amount of material and is particularly useful for semi-insulating materials where electrical contact is difficult. A reasonably monochromatic optical excitation source (such as a laser) is used to create electron-hole pairs in the sample. These photoexcited carriers then diffuse and recombine to generate photons (luminescence) with characteristic energies related to the bandgap. The resulting luminescence can generally be classified into three categories:

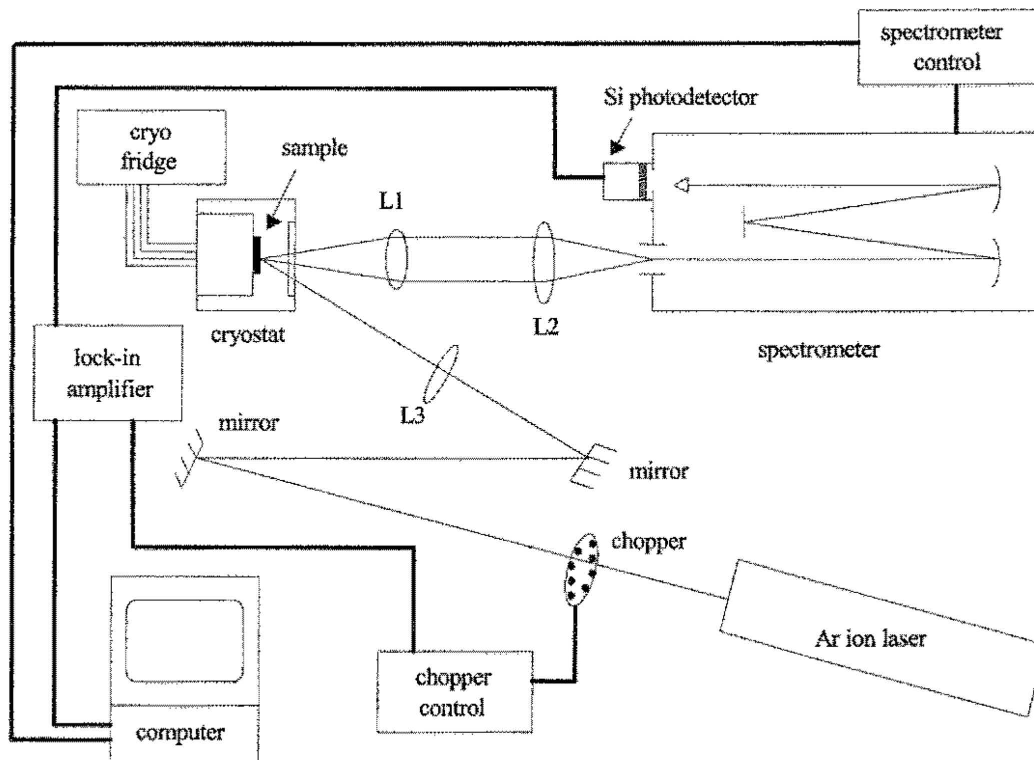

Figure 2.8 Schematic representation of the photoluminescence setup. Courtesy H. H. Tan.

(i) near band-gap transition, which is due to exciton or electron-hole pair recombination

(ii) shallow impurity transition, which is due to the recombination of related shallow donor and/or acceptor levels

(iii) deep level transitions, in which the recombination at deep impurities/defects occurs (typically >100 meV from the bottom of the conduction band)

By using light of different energies (above or below the band gap), different energy levels may be probed. In standard PL measurements, light with an energy greater than the

band gap is used, and in good quality materials, transition (i) dominates. The photoexcited carriers then diffuse and recombine to emit photons. Due to the lower energy states in quantum wells, the diffusing photoexcited carriers are preferentially trapped in the wells and the recombination of the electron-hole pairs generates photons with energies characteristic of the quantised energy levels of the wells which can then be collected and analysed. Detailed theory and aspects of PL and optical processes in semiconductors may be found in references 32 and 33.

For photoluminescence measurements performed at the University of New South Wales, a schematic of the setup is shown in Figure 2.8. In this case, a 4 W Coherent Innova 70 Ionpure water-cooled Ar ion laser is used as the excitation source. The laser has several lines but in this work an excitation wavelength of 514.5 nm is used. The specimens for PL measurements are mounted with vacuum grease on a closed-cycle liquid He cryostat. The laser beam is directed onto the sample through a chopper operating at a few hundred Hz. The resulting luminescence is then collected by a Si photodiode with a built in preamplifier via a set of lenses and a 0.75 m SPEC 1702/04 spectrometer. The signal from the photodetector is analysed by a lock in amplifier, which is tuned to the frequency of the chopper. A desktop computer is then used to control the spectrometer for a wavelength scan and also records the PL signal.

For PL measurements done at the Australian National University, a red diode laser operating at 670 nm, and an InGaAs photodetector through a 0.5 m monochromator were used.

2.4.10 Time Resolved Photoluminescence (TRPL)

Time resolved photoluminescence[34] measurements done for this work used luminescence upconversion spectroscopy in the pump-probe configuration. The output pulse train from an ultrafast laser is divided into two. The semiconductor sample under investigation is excited by one pulse train (pump) and the luminescence from the sample is collected using standard means and focused on a nonlinear crystal. The second pulse train (probe), which is delayed with respect to the pump by introducing an optical delay in its path, is also focused on the nonlinear crystal, overlapping the spot from the luminescence. The angle between the two beams and the angle of the nonlinear crystal are adjusted for phase matched sum-frequency generation at a given luminescence photon energy. The time resolution is limited by the laser pulse width, and the group velocity dispersion in the nonlinear crystal. The luminescence is then monitored to observe the changes in the sample produced by the pump. The time resolution obtained at the nonlinear crystal is detected in a time integrated manner by photon counting electronics after being dispersed by a spectrometer. If the relative delay between the two beams is scanned, the time evolution of the luminescence at a given photon energy can be acquired. Time resolved luminescence spectra can be obtained by keeping the delay fixed and synchronizing the scanning angle of the nonlinear crystal and the spectrometer. Analysis of samples using this technique was done both at the University of New South Wales and the Royal Institute of Technology in Sweden. Those measurements performed at the former were done by Dr. L. V. Dao at the School of Physics, The University of New South Wales, using a femtosecond self-mode locked Ti:sapphire laser. The laser was tunable between 750 and 900 nm, the pulse width was 80 fs, the repetition rate 85 MHz, and the output power was 200 mW at λ=780 nm. Measurements performed at the latter location were done at the Department of

Microelectronics and Information Technology by A. Gaarder and Prof. S. Marcinkevičius, using an upconversion set-up with excitation at 800 nm and PL detection at the band gap wavelength, also with a femtosecond Ti:sapphire laser.

2.4.11 Time Resolved Differential Reflectance (TRDR)

A pump-probe setup similar to the time resolved photoluminescence is used in this technique, where, by chopping the pump beam and using a lock-in amplifier, the changes in the reflected probe as a function of the time delay between pump and probe pulses are measured. Typically the probe is much weaker than the pump. The data are typically presented in the form of normalized Differential Reflectance given by $\Delta R/R_o = (R - R_o)/R_o$, the change in reflection $\Delta R = R - R_o$ induced by the pump pulse divided by the reflection of the probe in the absence of the pump, R_o.

The dynamics in a pump probe reflection experiment are determined by coherent and incoherent effects. Interpretation of differential reflectance results is more difficult than for luminescence measurements since this is a nonlinear technique while the latter is a linear technique. When the time scale is comparable to or shorter than the dephasing times of the system, the pump-probe signal can be viewed as the diffraction of the pump beam in the probe direction. Thus, the semiconductor Bloch equations are required to calculate the third order nonlinear polarization radiating in the probe direction (which corresponds to the pump-probe signal). Incoherent effects can be divided into many-body effects and occupation effects. Many body effects include changes in the energy band structure (such as band gap renormalization or a change in the exciton binding energy), broadening of energy levels, etc., and depend strongly on the photoexcited density as well as whether the system consists of

excitons or free carriers. Occupation effects are due to changes in the optical properties or transition rates brought about by the nonequilibrium occupation of certain states. For further details regarding the interpretation of the reflectance measurements, the reader is directed to Ref. 24. Samples were analysed at the Australian National University and the Royal Institute of Technology in Sweden. In the former location, measurements were done by Dr. M. J. Lederer and V. Kolev at the Laser Physics Centre, in the Research School of Physical Sciences and Engineering. 75 MHz, 100 fs pulses from a mode-locked Ti:Sapphire laser were tuned to a wavelength of 895 nm, exciting the samples with pump fluences (F_{pump}) of 50 $\mu J.cm^{-2}$ or 5 $\mu J.cm^{-2}$. In the latter location, A. Gaardner and Prof. S. Marcinkevičius also did degenerate TR experiments at the Department of Microelectronics and Information Technology, Royal Institute of Technology, with a central pump and probe wavelength of 1600 nm and an optical parametric oscillator providing pulses of 80 – 150 fs duration, where the probe intensity was 0.01 of the pump intensity.

References

1. T.F. Kuech, "*Metal-organic vapor phase epitaxy,*" Mat. Sci. Rept. **2**, 1 (1987).
2. G. B. Stringfellow, *Organometallic Vapor-Phase Epitaxy: Theory and Practice*, Academic Press, San Diego (1989).
3. J. J. Coleman and P. D. Dapkus, "*Metalorganic chemical vapor deposition*", in III –V Semiconductor Materials and Devices, R. J. Malik, editor, North Holland Publishers, Amsterdam (1989).
4. M. J. Ludowise, J. Appl. Phys. **58**, R31 (1985)
5. G. Dearnaley, J. H. Freeman, R.S. Nelson and J. Stephen, *Ion Implantation*, North-Holland Publishers, Amsterdam (1973)
6. J. W. Mayer, L. Eriksson and J. A. Davies, *Ion Implantation in Semiconductors*, Academic Press, New York (1970)
7. J. S. Williams and J. M. Poate, editors, *Ion Implantation and Beam ProcessingI,* Academic Press, Sydney (1984)
8. J.P. Biersack and L.G. Haggmark, "*A Monte Carlo computer program for the transport of energetic ions in amorphous targets*", Nucl. Instrum. Meth. **174**, 257 (1980)
9. D. R. Lide, Editor, *Handbook of Chemistry and Physics*, 73rd ed., CRC Press, Florida (1992)
10. R. B. Fair, *Rapid Thermal Processing*, Academic Press, San Diego (1993)
11. B. Chapman, *Glow Discharge Processes*, John Wiley, New York (1980)
12. R. Reif, in *Handbook of Plasma Processing Technology: Fundamentals, Etching, Deposition and Surface Interactions,* edited by S. M. Rossagnel, J. J. Cuomo, and W. D. Westwood, Noyes Publications, Westwood (1990)
13. B. K. Tanner, J. Crystal Growth, **99**, 1315 (1990)
14. B. K. Tanner and D. K. Bowen, J. Crystal Growth, **126**, 1 (1993)

15. S. Takagi, Acta Cryst., **15**, 1311 (1962), S. Takagi, J. Phys. Soc. Japan, **26**, 1239 (1969);D. Taupin, Bull. Soc. Fr. Mineral. Cristallogr., **87**, 469 (1964)

16. P.B. Hirsch, A. Howie, R.B. Nicholson, D.W. Pashley and J.M. Whelan, *Electron Microscopy of Thin Crystals*, Butterworths, London (1967).

17. P.J. Goodhew and F.J. Humphreys, *Electron Microscopy and Analysis*, Taylor and Francis Ltd., London (1988).

18. J.W. Edington, *Monographs in Practical Electron Microscopy in Materials Science*, vols. 1-4, Philips Technical Library, Eindhoven (1974).

19. W.-K. Chu, J.W. Mayer and M.-A. Nicolet, *Backscattering Spectrometry*, Academic Press, New York (1978).

20. J.S. Williams and R.G. Elliman, "Channeling," in *Ion Beams for Material Analysis*, J.R. Bird and J.S. Williams, editors, Chp. 6, 261-333, Academic Press, Sydney (1989).

21. L. C. Feldman and J. W. Mayer, *Fundamentals of Surface and Thin Film Analysis*, Elsevier Science, New York (1996)

22. D. Briggs, Ed., *Handbook of X-ray and Ultraviolet Photoelectron Spectroscopy*, Heydon and Son, London (1977)

23. P. Blood and J. W. Orton, *The Electrical Characterization of Semiconductors: Majority Carriers and Electron States*, Academic Press London(1992)

24. L. J. Van der Pauw, Philips Res. Rep. **13**, 1 (1958).

25. R. C. Barret and C. F. Quate, J. Appl. Phys. 70, 2725 (1991).

26. C. C. Williams, Ann. Rev. Mater. Sci. **29**, 471 and references therein, (1999).

27. S. Anand, IEEE Circuits and Devices, **16**, 12 (2000).

28. P. de Wolf, T. Clarysse, W. Vandervost, L. Hellemans, Ph. Niedermann, and W. Hänni, J. Vac. Sci. Technol. B. **16**, 355 (1998).

29. P. De Wolf, M. Geva, C. L. Reynolds, T. Hantschel, W. Vandervorst, R. B. Bylsma, *J.* Vac. Sci. Technol. A. 17 (4), 1285 (1999).

30. R. P. Lu, K. L. Kavanagh, St. J. Dixon-Warren, A. Kuhl, A. J. Spring Thorpe, E. Griswold, G. Hillier, I. Calder, R. Arés and R Streater, J. Vac. Sci. Technol. B. 19, 1662 (2001).

31. P. De Wolf, R. Stephenson, T. Trenkler, T. Clarysse, T. Hantschel and W. Vandervorst, J. Vac. Sci. Technol. B. 18, 361 (2000)

32. H. B. Bebb and E. W. Williams, "Photoluminescence I: Theory," Chp 4, 182-320 and E. W. Williams and H. B. Bebb, "Photoluminescence II: Gallium Arsenide," Chp 5, 321 in *Semiconductors and Semimetals, Vol. 8, Transport and Optical Phenomena,* R. K. Willardson and A. C. Beer, editors, Academic Press, New York (1972)

33. J. I. Pankove, *Optical Processes in Semiconductors,* Dover Publications Inc., New York (1971)

34. J. Shah, *Ultrafast Spectroscopy of Semiconductors and Semiconductor Nanostructures*, Springer-Verlag, Berlin (1996)

CHAPTER 3

Structural, Electrical and Optical Properties of Ion Implanted InP

3.1 Introduction

Indium phosphide (InP), and its derivatives, is one of the top material science fields on today's compound semiconductor scene. It constitutes the fourth wave in semiconductor materials, the first of which started with germanium based transistors, which was surpassed in the early 1960s by silicon device technology, and which was then followed by the emergence of GaAs in the late 1980s. Si technology continues to dominate the semiconductor industry, while GaAs is the material of choice for high performance, high volume commercial applications. InP offers many advantages over GaAs in fibre-optic, millimeter wave and wireless applications. In fibre-optics, InP is the only semiconductor technology that allows photodetectors and lasers to be integrated on the same substrate with other analog and mixed signal functionality, yielding advances in integration and cost reduction. In the wireless industry, InP-based amplifiers provide significant performance improvements, such as lower power consumption, high linearity and low temperature sensitivity, that significantly enhance battery life and reception. In millimetre-wave applications that are beyond the capabilities of GaAs or Si, InP devices can easily be fabricated for passive imaging and other applications that are just emerging in the marketplace. Noted especially for its incredible operating speeds, the industry's key systems integrators of broadband fibre-optic and wireless components are moving rapidly in the direction of employing InP based components for their next generation communication systems. Silicon technologies are being displaced by InP at the heart of many leading edge applications.

In spite of this, there continues to be a significant lack of InP processing experience while companies attempt to move the InP process from the research lab into the production line. Establishing correlations between material characteristics and device performance for InP

is crucial for stable and successful fabrication. With this in mind, thorough investigations are presented here into the characteristics of ion implanted InP.

Ion implantation into InP is not a new topic for study, although a comprehensive investigation into the effects of implantation, correlating structural, optical and electrical measurements, has not been presented before. An initial motivation for a study of the effect of ion implantation on InP was the interest already displayed in low temperature grown (LT-) and ion implanted GaAs, which had been found to have ideal properties for the fabrication of ultrafast photodetectors[1-5]. A more thorough discussion of the considerations for achieving this particular aim in InP, as well as in InGaAs, is provided in Chapters 5 and 6. Here we focus on a general study into the damage resulting from ion implantation into InP as a function of dose, annealing and implant element, and the corresponding optical and electrical properties. P, As, Ga and In were chosen as implant elements because they were either group III or group V and were not known dopants in InP, thus it was hoped that any chemical effects would be minimised. Interestingly, we find that the amount and type of damage induced in InP by implanting with different elements does not scale with ion mass. The defect accumulation and agglomeration was specific to each element and played an important role in determining the electrical and optical properties of the material. The electrical characteristics of ion implanted InP are dominated by the formation of shallow donor-like defect levels, while the optical characteristics are controlled by deeper levels within the bandgap.

3.2 Experimental

The implantations for this work were carried out on SI (100) InP substrates (doped with Fe) at 200°C because of the known sensitivity of this material to amorphisation when implanted at

room temperature, with the sample tilted at 7° from the normal direction of the beam to minimise channeling effects. Initial dose dependent studies were carried out using P ions with doses ranging from between 10^{12} and 10^{16} cm^{-2}. A comparison with the results of these studies was done using In ions, where doses were scaled in order to yield approximately the same maximum damage as for the previous P ion implants. For studies into the effect of implantation with different elements, the dose was kept at 10^{16} cm^{-2}, and apart from P and In, As and Ga ions were also implanted. The energies of these elements were 1, 3.3, 2 and 2.1 MeV, respectively, as chosen from Transport of Ions in Matter (TRIM) simulations, such that the peak damage was located approximately 1 μm from the surface. For studies into the effect of post-implant annealing, temperatures ranged from 400 to 700°C, and the annealing time was 30s. Samples were rapid thermally annealed in an Ar atmosphere with InP proximity capping to minimise out-diffusion of P and a corresponding In buildup at the surface.

Structural studies used double crystal X-ray diffractometry (DCXRD) and cross-sectional transmission electron microscopy (XTEM). Electrical characteristics of the samples were determined by Hall effect measurements using the van der Pauw geometry, with sintered indium metal ohmic contacts, as well as scanning spreading resistance microscopy (SSRM) and scanning capacitance microscopy (SCM). The samples for SSRM and SCM consisted of epitaxial InP, about 2 μm thick, grown on n^+ InP substrates, which were then implanted with the different ion species.

Optical characteristics were measured with time resolved photoluminescence (TRPL) and time resolved differential reflectance (TRDR). Some of the measurements were perfomed on p -InP epilayers (free carrier concentration ~3.4 x 10^{17} cm^{-3}) grown on SI InP substrates. The former technique used a femtosecond self-mode locked Ti:sapphire laser, with a $LiIO_3$ nonlinear crystal. The laser was tunable between 750 and 900 nm, the pulse width was 80 fs,

the repetition rate 85 MHz, and the output power was 200 mW at λ=780 nm. The latter technique used a standard wavelength-degenerate pump-probe setup. 75 MHz, 100 fs pulses from a mode-locked Ti:Sapphire laser were tuned to a wavelength of 895 nm, exciting the samples with pump fluences (F_{pump}) of 50 $\mu J.cm^{-2}$ or 5 $\mu J.cm^{-2}$.

3.3 Structural Studies

Observing the changes in the InP lattice structure resulting from implantation, both in terms of induced strain as well as the defective nature of the material - apart from being an interesting study into the kinetics of damage in this particular semiconductor compound - also gives a great deal of information which can help explain the resulting optical and electronic properties. After investigating the effect of implanting at different doses, the effects of implanting with different ions and subsequently annealing at different temperatures are explored.

3.3.1 Dose dependence

Figure 3.1 shows the DCXRD rocking curves for 1 MeV P ion implantation at 200°C for implants to different doses. The main peak located at 0 arcsec corresponds to the signal from the substrate, and features on either side of this are caused by layers of in-plane compressive (expansion in the growth direction) and tensile strain (compression in the growth direction) in the sample. A thicker strained layer will in general increase the amplitude of the peak, while

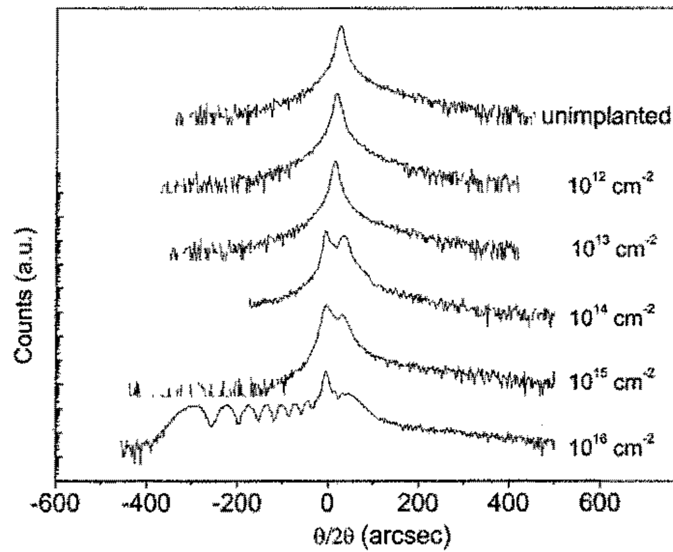

Figure 3.1 DCXRD spectra of 1 MeV P ion implanted into SI InP at 200°C as a function of dose. Spectra vertically shifted for clarity.

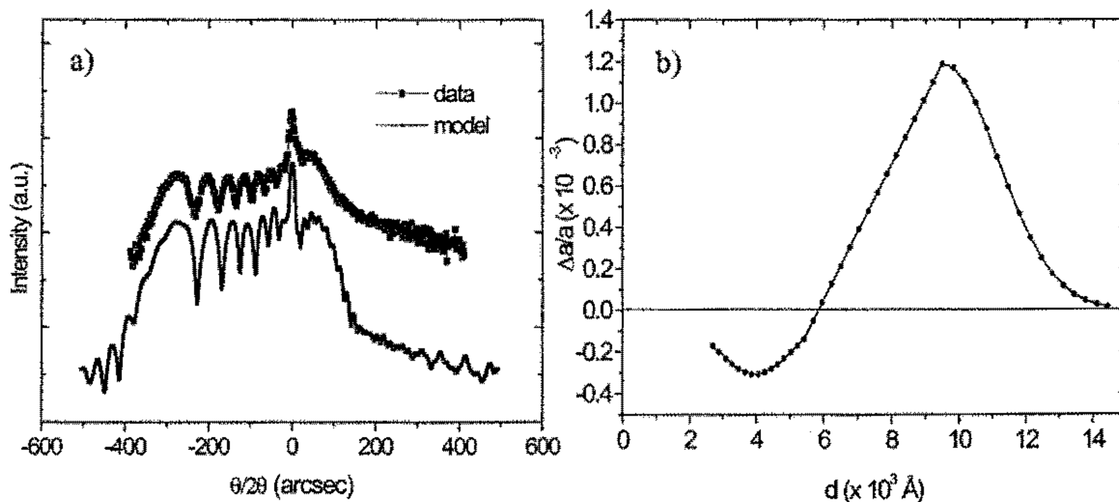

Figure 3.2 Measured and simulated DCXRD spectrum for 10^{16} cm^{-2} implant of 1 MeV P ions in InP at 200°C (a); (b) strain profile corresponding to simulated spectrum in (a).

the distance from the central peak gives an indication of the difference in lattice spacing (or % strain) with respect to the substrate. The lowest dose produces a rocking curve essentially the same as an unimplanted sample. The strain increases as the dose is increased, and for implantation to a dose of 10^{16} cm^{-2}, extensive damage has occurred in the sample. A transition in the type of damage has occurred between the doses of 10^{15} and 10^{16} cm^{-2}. Hypothetical strain profiles can be used to simulate these DCXRD spectra, using the Takagi-Taupin theory[6]. For example, Figure 3.2 (b) shows a strain profile that has produced a spectrum similar to that of the 10^{16} cm^{-2} P ion implanted case, as shown in Fig 3.2 (a). The shape of this simulated profile is taken from the known damage profiles induced by ion implantation, where the peak damage region is expected to experience expansion in the growth direction (in the case of 1 MeV P ion implants into InP, at a depth of approximately 1 μm), and thus in-plane compressive strain. The expansion results from excess atoms (interstitials) that have migrated there after being 'kicked out' of their original lattice positions, not to mention the presence of the implanted ions themselves. Nearer the surface, the damage is expected to consist mainly of vacancies, which would cause compression in the growth direction, thus in-plane tensile strain. As far as the simulations in Fig 3.2 are concerned, the periodic fringes on the negative angle side of the rocking curve were created by the layer of in-plane compressive strain (positive $\Delta a/a$), while the broader feature for $\theta/2\theta$ between 0 and 100 arcsec was created by a layer of in-plane tensile strain (negative $\Delta a/a$). This modeling tells us that the features in the rocking curves are, in particular, very sensitive to the strain gradient. A fairly shallow gradient as illustrated in Fig 3.2 (b) will result in periodic fringes, while a steeper gradient will approximate well defined layers and produce a single peak (for each layer), such as for the 10^{14} and 10^{15} cm^{-2} implant case in Fig 3.1.

Figure 3.3 shows the rocking curves for 3.3 MeV In ions at 200°C as a function of dose, where the doses in this case were scaled so that the same level of damage was created as for the P ion implants in Figure 3.1. Essentially a similar trend with dose is observed, suggesting that it is the amount of damage that determines the strain in the sample, thus also the DCXRD features, and not any chemical effects which might be caused by implantation with different elements. Differences in the spectra for the highest In and P ion dose implants are mainly due to the differences in the strain gradient.

3.3.2 Implant element and annealing dependence

Figure 3.4 shows the DCXRD spectra for 200°C 10^{16} cm^{-2} implants with P, As, Ga and In ions as a function of annealing temperature. P and As ion implantation produce similar spectra - and presumably similar types of damage – whilst slightly different behaviour is observed for the Ga and In ion cases. From the previous dose dependence studies it could be assumed that these differences in behaviour are ultimately due to the different levels of damage that are created by implantation to the same dose for each element. However, predictions of the extent of damage rely principally on the atomic mass of each element. It would then be logical to assume that implantation with Ga and As ions, whose atomic masses are very close together (~69 and 75 amu, respectively, when compared to 31 for P and 115 for In) would produce DCXRD spectra with the greatest similarity. Instead we find that the similarity is closest between P and As ion implanted samples. This is the first indication that more complicated damage accumulation processes are occuring during the implantation of InP with different elements. The spectra for Ga implantation show the same periodic fringes as those for P and

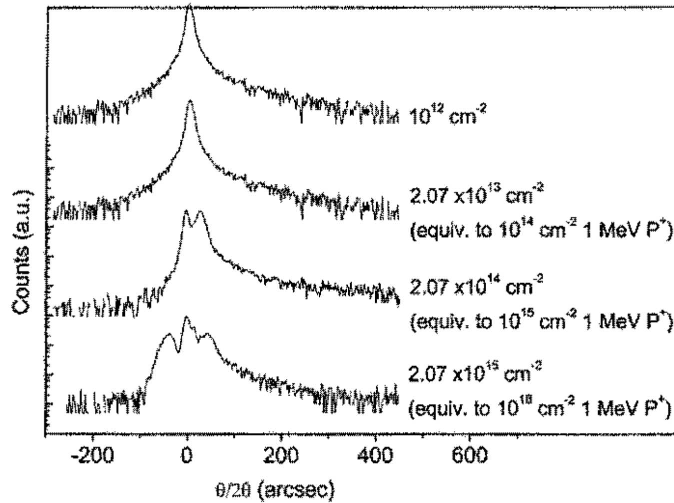

Figure 3.3 DCXRD spectra of 3.3 MeV In ion implanted SI InP at 200°C at different doses corresponding to the damage created by 10^{14}, 10^{15} and 10^{16} cm^{-3} 1 MeV P ion implants at the same temperature. Spectra vertically shifted for clarity.

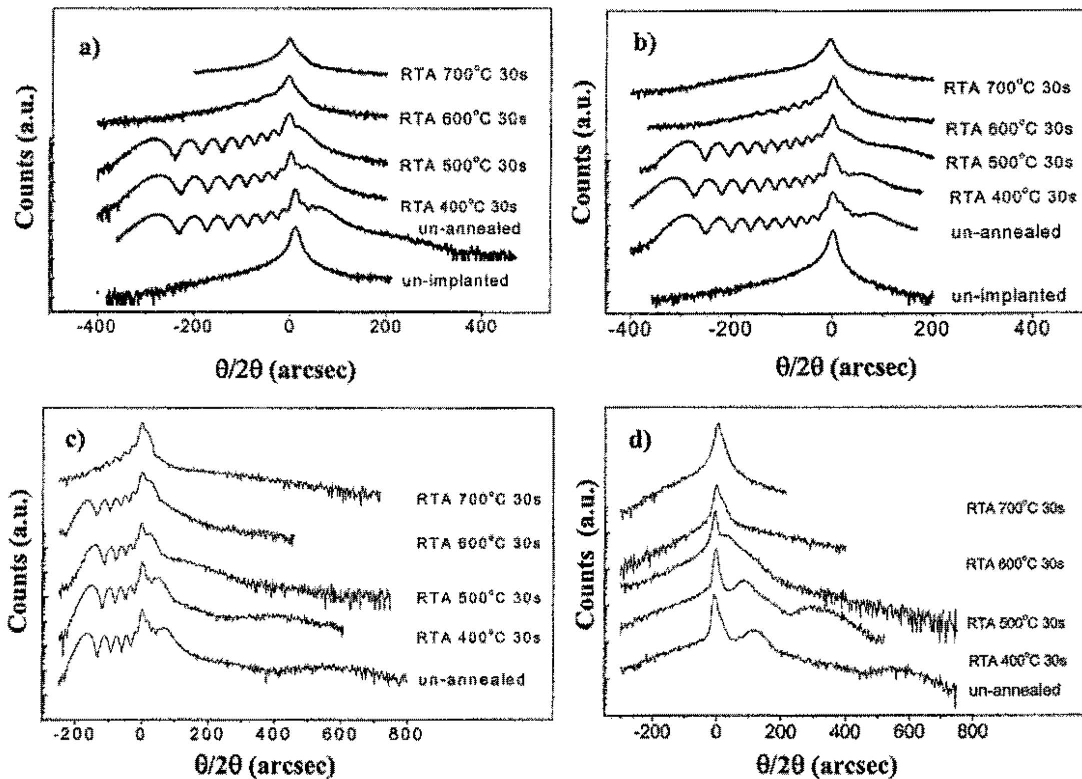

Figure 3.4 X-ray rocking curves from InP implanted with various ions at 200°C to a dose of 10^{16} cm^{-2}. (a) 1 MeV P, (b) 2 MeV As, (c) 2.1 MeV Ga and (d) 3.3 MeV In. Spectra vertically shifted for clarity.

As ion implantation, but over a narrower angle range. These fringes are still present after annealing at 700°C, when for all other samples evidence of major damage has been annealed out at 600°C. Possibly, the recrystallisation processes during annealing are being affected by the implanted Ga atoms. In implantation does not yield periodic fringes at all; moreover, there is no peak corresponding to a compressively strained layer. From these results, since the Bragg condition for diffraction is no longer satisfied, it could be concluded that the region of maximum damage in these samples is amorphised (and hence not detected in DCXRD), or else so defective that the signal from this region is not distinguishable from the general noise in the spectrum. Unlike the case for As and P ion implants, both Ga and In ion implants result in broad features at $\theta/2\theta$ ~ 600 arcsec, which are assumed to be due to in-plane tensile strain resulting from the vacancy-rich region close to the surface. The larger FWHM of the main peak observed in all the samples when annealed at the highest temperatures, compared to that of the unimplanted sample, is indicative of residual defects in the material.

Etching as well as XTEM measurements allow more precise identification of the depth and types of damage which generate these features in the DCXRD measurements. Figure 3.5 (a) shows X-ray rocking curves for InP implanted with 2 MeV As ions to a dose of 10^{16} cm^{-2}, and then etched with 100% HCl in successive 10 second intervals. Clearly, the in-plane strain tensile features close to the substrate peak come from the 0.8 μm nearest the surface, while the periodic in-plane compressive strain structures result from a narrow layer ~ 1 μm into the sample. Figure 3.5 (b) shows the results for a similar experiment performed on a 10^{16} cm^{-2} In ion implanted sample. These measurements show that the broad features at large positive angles come from within the first 0.2 μm from the surface, and again that the in-plane tensile strain features closer to the substrate peak are generated in the first 0.8 μm from the surface.

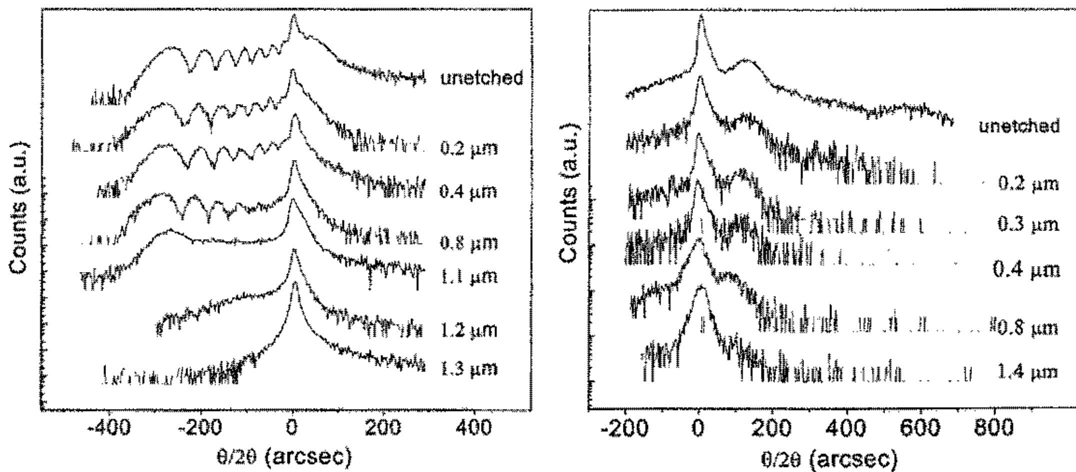

Figure 3.5 DCXRD spectra for (a) 2 MeV As and (b) 3.3 MeV In ion implanted InP at 200°C to a dose of 10^{16} cm^{-2} as a function of etch depth. Spectra vertically shifted for clarity.

Figure 3.6 shows the XTEM images for SI InP samples implanted with As, Ga and In ions, both prior to and after annealing at 700°C for 30 s. The contrast in the images is caused by strain resulting from lattice defects, although point defects or small clusters, which produce only a small amount of strain, are not detectable. A thin layer of damage is visible ~ 1 μm from the surface in all of the as-implanted samples, which corresponds to the depth of maximum damage/ion range predicted by the TRIM simulations. In combination with the information already gleaned through the DCXRD/etching experiments described above, this points to the layer of maximum damage as being the region responsible for the periodic fringes. Annealing causes the visible damage to 'spread' vertically. This phenomenon suggests that the majority of lattice defects in the as-implanted samples are in the form of point defects or small clusters. During the annealing process, agglomeration of these small lattice defects ensues.

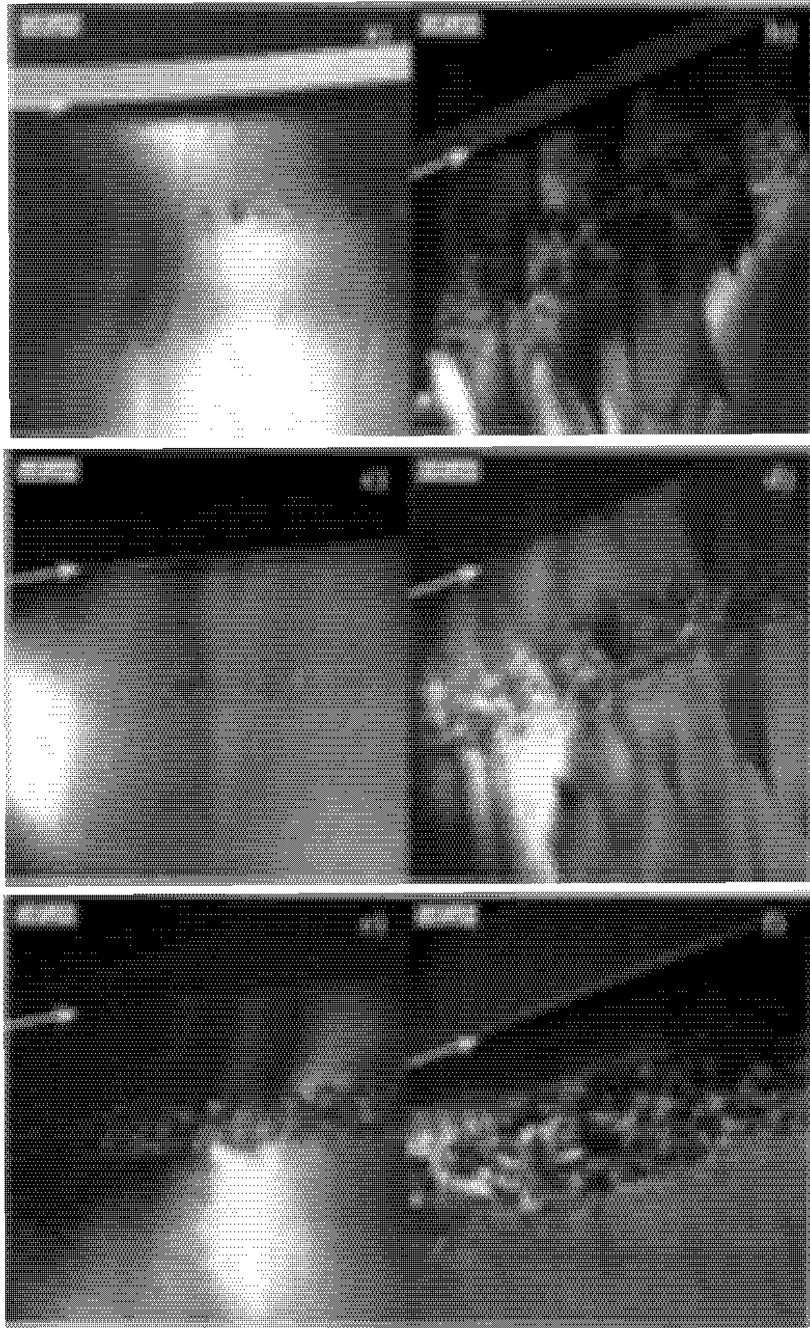

Figure 3.6 Cross sectional TEM images of As ion as-implanted (a) and annealed (b), Ga ion as-implanted (c) and annealed (d), and In ion as-implanted (e) and annealed (f) semi-insulating InP. Annealing was for 30 seconds at 700°C. Arrow indicates surface.

It is clear from the images that the In ion implantation has not resulted in amorphisation in the sample, but the damage is greater than for implantation with the other elements. Importantly, the type of damage is dependent on implant species: As ion implantation results in a thin layer of loops and clusters which spreads into a thicker layer of larger loops after annealing; Ga ion implantation results in a similarly thin layer of loops and clusters which spreads into a thicker layer of high density loops and clusters after annealing; and In implantation results in a thick layer of damage including stacking faults and loops, which spreads into a thicker layer of large loops and defects after annealing. The XTEM scans provide the strongest evidence that the atomic mass of the implant species is not the only factor in determining the degree and type of damage produced in InP, and that the defect accumulation and annihilation mechanisms during implantation and annealing are different for each implant species.

Summary

We have seen how single MeV implants into semi insulating InP using P, As, In and Ga ions have resulted in a layer of defects 1 μm from the surface corresponding to the maximum damage/ion range as predicted by TRIM simulations. This layer is responsible for in-plane compressive strain features in DCXRD measurements. In plane tensile strain occurs in the region between the peak damage and the surface, and is probably due to the creation of large amounts of vacancies there. Damage increases as the dose is increased, and annealing at high temperatures allows for formation of more extended complex defects such as loops which spread along the growth direction. The strain profiles and types of damage were similar for P and In ion implants when the doses were scaled using TRIM to give the same maximum damage. For implants at the same dose, As and P ion implants resulted in similar damage,

whereas damage was different for Ga and In ions, clearly illustrating that damage did not scale with implant ion mass.

3.4 Electrical Studies

With the ultimate aim of producing optoelectronic devices from implanted InP, it is important to study the implant-induced changes in the electrical properties of this semiconductor. As it turns out, the electrical characteristics of this damaged material play a crucial role in determining its feasibility for devices, due to certain defects which cause highly conductive regions, where in other semiconductors, under the same implant conditions, highly resistive materials are formed.

3.4.1 Dose dependence

In Fig 3.7, Hall effect measurements on the samples implanted with P and In ions at 200°C, whose DCXRD spectra were shown in Figs 3.1 and 3.3, illustrate a similar evolution of electrical characteristics as a function of equivalent doses. The equivalent doses are defined as the doses at which the same number of atomic displacements were created for 1 MeV P and 3.3 MeV In ion implants (simulated using TRIM). An unimplanted, semi-insulating (SI) InP wafer has a mobility μ_{eff}, of approximately 2000 $cm^2V^{-1}s^{-1}$, sheet carrier concentration N_s of 10^7 cm^{-2} and sheet resistance R_s of 3×10^8 Ω/□. Implanting at the lower doses changes the material from SI to *n*-type, reducing R_s to the 10^6 Ω/□ range, increasing N_s to $\sim 10^{10}$ cm^{-2} and

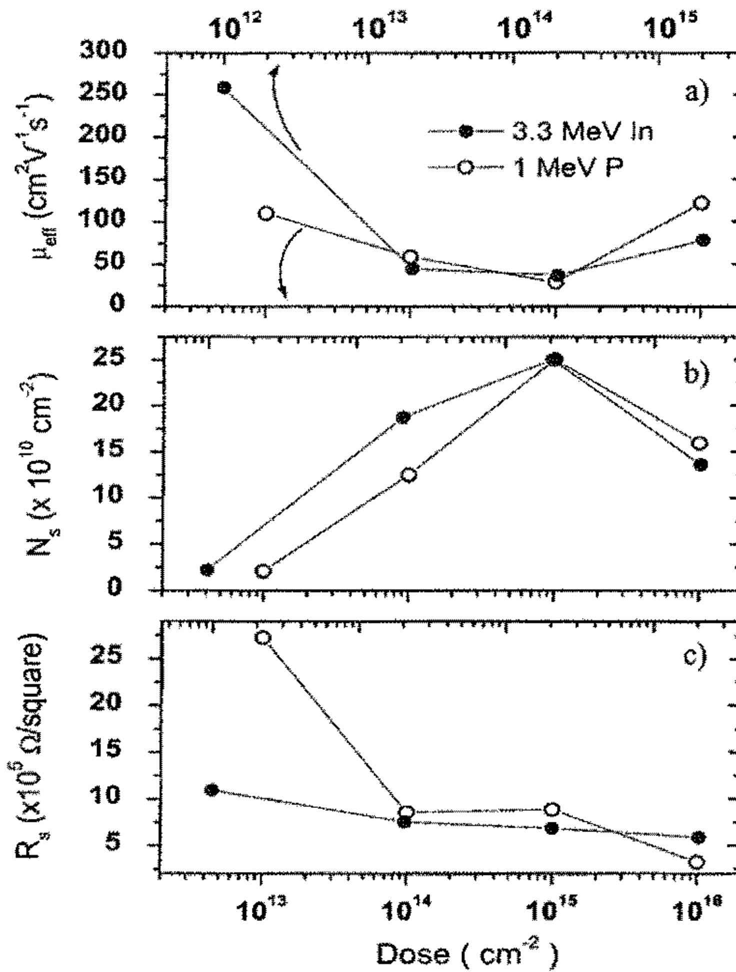

Figure 3.7 Effective mobility μ_{eff} (a), sheet carrier concentration N_s (b) and sheet resistance R_s (c) as determined by Hall measurements, for implants at 200°C into SI InP.. Bottom scale: as a function of 1 MeV P dose; top scale:as a function of 3.3 MeV In dose. Top and bottom dose scales are aligned to indicate equivalent atomic displacements for P or In ion implants, as calculated by TRIM.

reducing the effective mobility to the hundreds of $cm^2V^{-1}s^{-1}$. As the dose is increased, R_s becomes progressively smaller, sinking to ~5 x 10^5 Ω/□ for the highest dose. The sheet carrier concentration increases to a maximum of ~2.5 x 10^{11} cm^{-2} for a 1 MeV P dose of 10^{15} cm^{-2} (equivalent to 2.07 x 10^{14} cm^{-2} for In ion implantation), before decreasing at the highest

dose. The effective mobility, μ_{eff}, decreases to the tens of $cm^2V^{-1}s^{-1}$ for a 1 MeV P ion dose of 10^{15} cm^{-2}, and does not exceed 100 $cm^2V^{-1}s^{-1}$ at the highest dose. These changes must of course be attributed to the implantation induced defects.

As illustrated in the earlier XTEM images, the damage created by ion implantation into InP at elevated temperatures consists of point defects and their complexes[7,8], as well as more extended defects such as clusters and loops. Of the point defects, the most common in InP are phosphorus and indium vacancies, as well as interstitials, which often form pairs with vacancies and antisite defects. Some of these point defects have donor levels very close to the conduction band. In particular, these are the phosphorus vacancy, the phosphorus antisite, and the indium interstitial. The antisite defects in III-V materials have been intensively studied, and particularly in defective GaAs, the arsenic antisite was found to be responsible for its semi-insulating behaviour[9]: in As ion implanted GaAs, the main carrier traps were found to be mid gap As-antisite defects, similarly as in low temperature grown (LT-) GaAs.[10]

In InP, the presence of these defects has a different character, creating n-type free carriers[11]. LT- grown InP provides a useful source of comparison when attempting to explain the electrical behaviour of ion implanted InP, in the same way that implanted GaAs was found to behave similarly to LT-GaAs. It has been found[9] that LT-InP epilayers were highly conductive and that a dominant intrinsic deep level defect was present in concentrations as high as 10^{19} cm^{-3}. The mechanism responsible for the n-type conductivity was attributed to an abundant presence of P_{In} antisites, which are known shallow donors[12], introduced during off-stoichiometric InP growth at low temperature.

Being smaller than indium, phosphorus can easily migrate at high annealing temperatures and occupy In vacancies produced during implantation, thereby creating P antisites and P vacancies. While the P antisite is a shallow donor, the P vacancies are deep

donors[13]. Overall, this is a strong indication that in implanted InP, the electrical properties are determined by phosphorus related defects, as was the case for LT InP.

Apart from these point defects, the implantation and annealing will also result in extended defects such as loops and clusters, whose overall electrical configuration is unknown, but which ultimately could be playing a significant role in determining the electrical properties of the material.

The results shown in Figure 3.7 can therefore be explained in terms of production of shallow donors as well as other defects which act as carrier traps. Implantation reduces the sheet resistance and mobility and increases the sheet carrier concentration when compared to the original SI values, due to the production of shallow donor levels. As the dose is increased this trend continues until a 1 MeV P ion dose of 10^{15} cm^{-2}, or a 3.3 MeV In ion dose of 2.07 x 10^{14} cm^{-2}, above which the sheet carrier concentration reduces and the effective mobility increases, while R_s continues to decrease slightly. At this highest dose, as was shown in the DCXRD measurements of Figures 3.1 and 3.3, there appears to be a transition in the type of damage created in the sample, presumably causing a different distribution of the different types of defects, which results in a variation from the general trend. Indeed it would be expected at the higher doses that a greater concentration of extended defects would form, while at the lower doses point defects would predominate.

3.4.2 Implant element and annealing dependence

The post implantation evolution of Hall effect measurements as a function of annealing temperature for the samples which were implanted to 10^{16} cm^{-2} with all four ions is shown in Figure 3.8. Prior to annealing, the sheet resistance is reduced from the SI values to ~4 x 10^5

Ω/□, and the mobility is reduced to 180, 40, 45 and 113 $cm^2V^{-1}s^{-1}$ respectively for implantation with P, As, In and Ga ions. For annealing temperatures above 500°C, R_s is further reduced to tens or hundreds of Ω/□ and N_s becomes very large, indicating the presence of shallow donor-like levels. Annealing at temperatures above 600°C has generally increased mobilities to ~ 1.5 times the unimplanted value, with the exception of Ga ion implantation. As for the DCXRD results, P and As ion implanted samples have practically identical electrical behaviour as a function of annealing temperature. Annealing at 600 and 700°C, for Ga and In ion implantation, yields materials with higher sheet resistances and lower carrier concentrations than for P and As ion implantation.

Disruption of the Fe doping sites, whose role in the substrate is to compensate for inevitable shallow donor formation during crystal growth, may have allowed the intrinsic donors to re-activate and contribute to the large sheet carrier concentration. The presence of this effect is also indicated by the very high mobility values for annealing at 700°C. However, the typical Fe doping concentration is 10^{16} cm^{-3}, resulting in a sheet concentration of 10^{12} cm^{-2} in a 1 μm thick layer of InP. Thus, even if all the Fe acceptors were deactivated, the maximum increase in N_s that could be achieved by this mechanism is of the order of 10^{12} cm^{-2}. At annealing temperatures greater than 500°C, N_s is in excess of 10^{13} cm^{-2}. This provides further evidence that the shallow donor-like levels are created by defects in the crystal structure itself, as a result of the implantation and annealing process.[14,15] Annealing, by allowing for defects to migrate, be annihilated or form complexes with other defects, seems to provide the conditions for more shallow donor levels to form, as evidenced by the low values of R_s.

In order to glean more information about the effect of the non-uniform damage profile caused by the implantation, scanning spreading resistance microscopy (SSRM) and

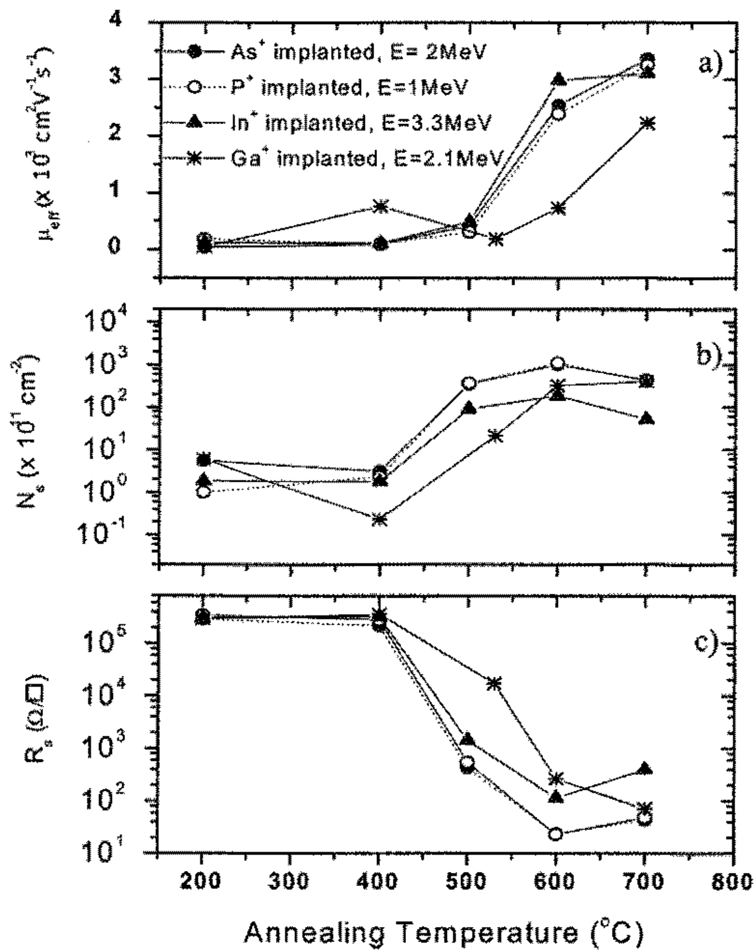

Figure 3.8 Mobility (a), sheet carrier concentration (b) and sheet resistance (c) as a function of annealing temperature, for P, As, Ga and In ion implanted SI InP.

scanning capacitance microscopy (SCM) measurements were performed on all four samples. Fig.3.9 (a) shows a typical SCM image obtained in the dC/dV-mode for Ga implanted InP annealed at 600°C. At this annealing temperature - as was illustrated in the structural measurements of Figs. 1-3 - significant defect migration and agglomeration is expected to have occurred in the samples, thus causing highly resistive regions with thicknesses that are different to what is expected for a 2 μm InP epilayer grown on an n^+-InP substrate. In this mode, the

SCM signal monotonically increases with decreasing carrier concentration. That is, a brighter contrast corresponds to regions of lower carrier concentration and darker contrast to regions of higher carrier concentration, for example the substrate ($\sim 10^{18}$ cm^{-3}). The contrast band (R1) is attributed to the epi/substrate interface region at a depth of ~ 2 μm. The reduced carrier concentration in this region could be due to defects at the interface or migration of defects from the implanted region. The dark band (R2), from about 1 to 2 μm, shows a low SCM signal and corresponds to a free carrier concentration value comparable to the substrate. In region R3, the bright band followed by a dark region close to the surface is indicative of strongly decreasing carrier concentration.

Fig. 3.9(b) shows a typical image obtained with SSRM for Ga ion implanted InP annealed at 600°C. The dc bias applied to the sample was -1 V. The contact between the diamond coated tip and InP is known to be Schottky-like, nevertheless, it is possible to relate the sample doping to the measured resistances[16]. Compared to the SCM image, a shift in the features R1, R2 and R3 towards the surface can thus be observed. The substrate appears dark due to low resistance. The contrast at the epi/substrate interface region is not as pronounced as in SCM, but section analysis of the image shows a decreasing carrier concentration. The contrast in region R2 consists of a bright narrow band (high resistance) at about 1 μm and dark bands on either side, i.e. a low resistance comparable to the substrate. The location of this narrow band corresponds to the expected location of the implantation peak. Contrast in region R3 is indicative of increasing resistance towards the surface, consistent with the SCM image. Thus, the observed inhomogeneity in the electrical properties is qualitatively consistent with XTEM results. Below, we compare the results obtained for the different samples, that is, for different implantation species and different annealing temperatures.

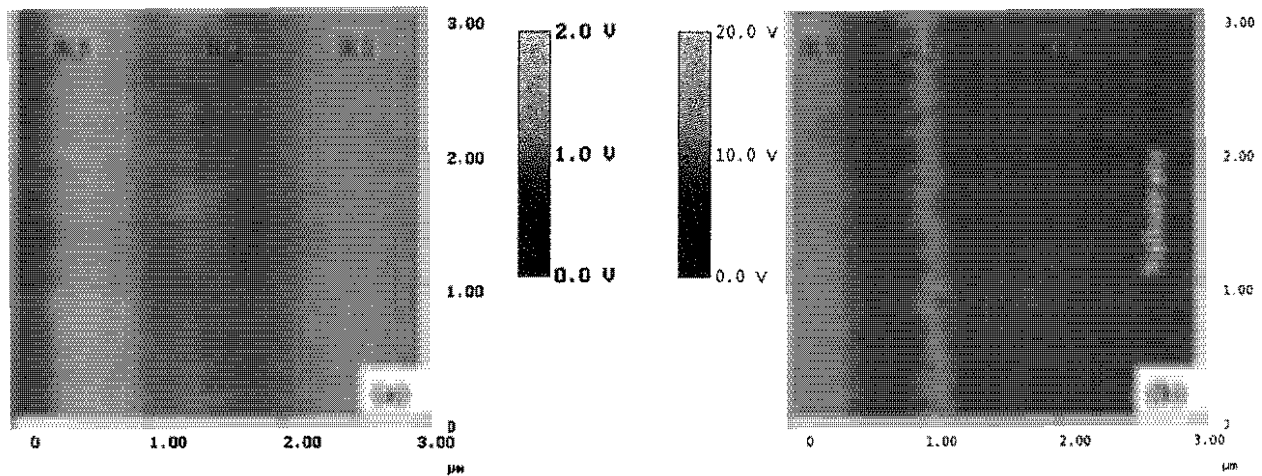

Figure 3.9 Ga ion implanted InP annealed at 600°C: (a) Representative SCM (dC/dV mode) image. The ac and dc biases were respectively 2V and 0V and (b) Representative SSRM image. The dc bias was −1V.

Typical SSRM and SCM results (line scans) obtained on P, As, Ga and In ion implanted InP (dose = 10^{16} cm^{-2}) annealed at different temperatures are presented in Figures 3.10 – 3.13 (a) and (b), respectively. Scanning across the sample edge was avoided so as not to have adverse effects on the measurements. The position of the zero of the distance-axis does not coincide for all the curves, but the origins are still within a maximum of 200 nm from the edge.

Both SSRM and SCM data show that the epilayer is highly resistive for all the samples annealed at 400°C, which is consistent with the Hall effect measurements. For Ga and As ion implants, a small peak in resistance is observed approximately 1 μm into the epilayer and its location corresponds with the expected maximum implantation depth. Correspondingly for this region, the SCM signals (Figs. 3.11 and 3.12(b)) are uniformly zero and near 1 μm no special feature could be distinguished. For intrinsic doping levels, due to the very large Debye

lengths, the SCM signal remains close to zero irrespective of the ac bias applied[16]. Beyond the epi-substrate interface region, approximately 2 μm – 3 μm, the resistance drops by two orders of magnitude, to the substrate level of about 10^5 Ω. As discussed earlier, the SCM signal shows a peak in this region. In the P and In ion implanted samples, the sharp high resistance peak appearing at the 1 μm depth is not observed.

As the annealing temperature is increased (500°C and 600°C), dramatic changes are observed. Defect diffusion and agglomeration such as have been illustrated in the XTEM scans will occur; the consequences of annealing on the electrical properties in the sample will therefore depend on the resulting spatial distribution of the defects. For the Ga and As ion implanted samples, the SSRM profile still shows a pronounced high-resistance region at about 1 μm. The observed location of this peak for the different samples is within 200 nm, which, as mentioned earlier, is within the error in the origin. On either side of this region the resistance is lower - forming two conductive layers above and below the main damaged region - and finally in the Ga ion implanted sample annealed at 600°C it is comparable to that in the substrate. For the As ion implanted sample, annealing at 600°C has resulted in only one, thicker, conductive layer, showing how the defect migration and agglomeration mechanisms vary for implants with each of the four ions.

Towards the surface the resistance is seen to increase, especially at the higher annealing temperatures. Because the defects in this surface region are not expected to exist in great concentrations (due to being in the 'tail' of the damage profile), and probably mainly consist of vacancies and other point defects, the annealing temperatures used here are most likely sufficient to anneal out all of these defects, resulting in a highly resistive surface region. By contrast, the resistance progressively decreases in substrate/epilayer interface region. In the XTEM scans of Fig 3.6, defects were shown to extend deeply into the sample after annealing

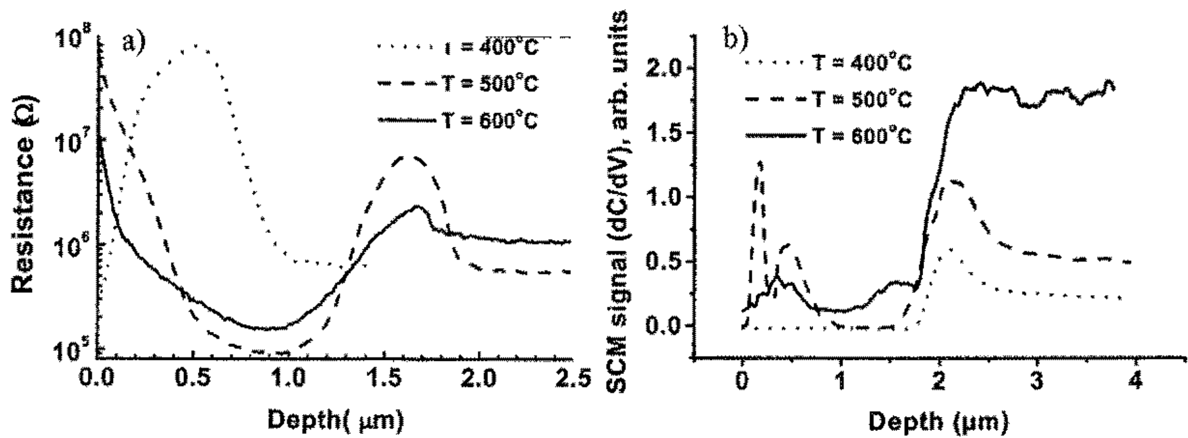

Figure 3.10 SSRM and SCM line scans obtained for the P ion implanted InP samples annealed at 400°C, 500°C and 600°C. (a) SSRM resistance profiles. (b) SCM profiles (dC/dV mode).

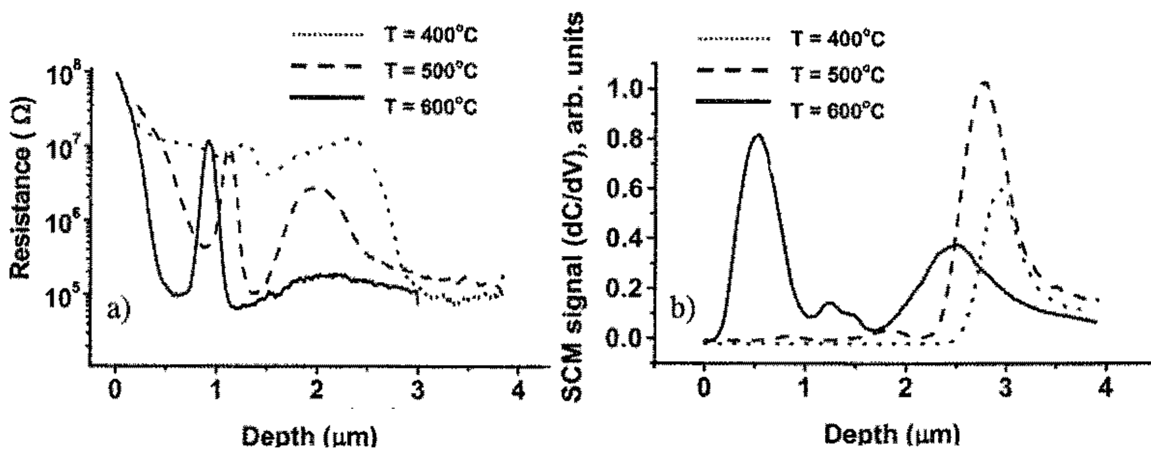

Figure 3.11 SSRM and SCM line scans obtained for the Ga ion implanted InP samples annealed at 400°C, 500°C and 600°C. (a) SSRM resistance profiles. (b) SCM profiles (dC/dV mode).

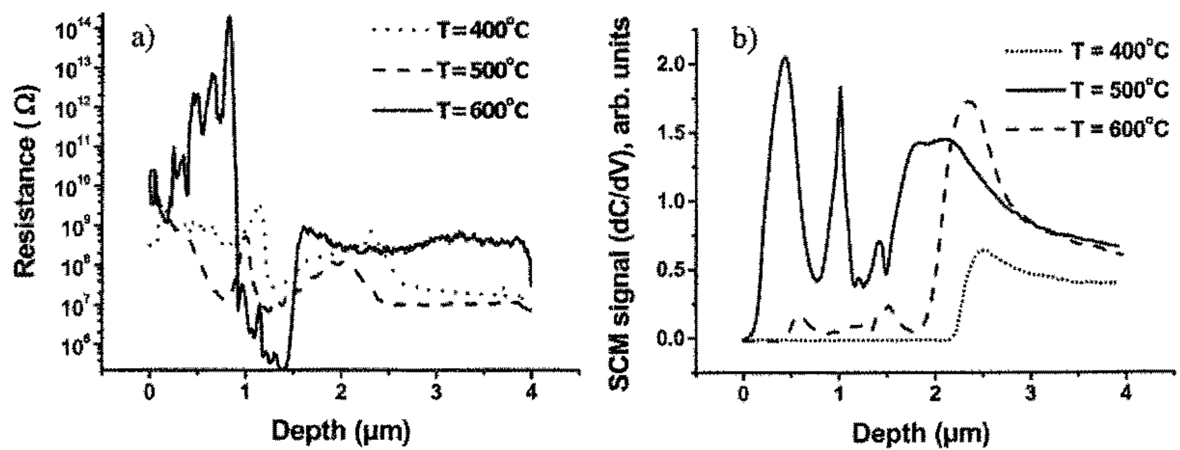

Figure 3.12 SSRM and SCM line scans obtained for the As ion implanted InP samples annealed at 400°C, 500°C and 600°C. (a) SSRM resistance profiles. (b) SCM profiles (dC/dV mode).

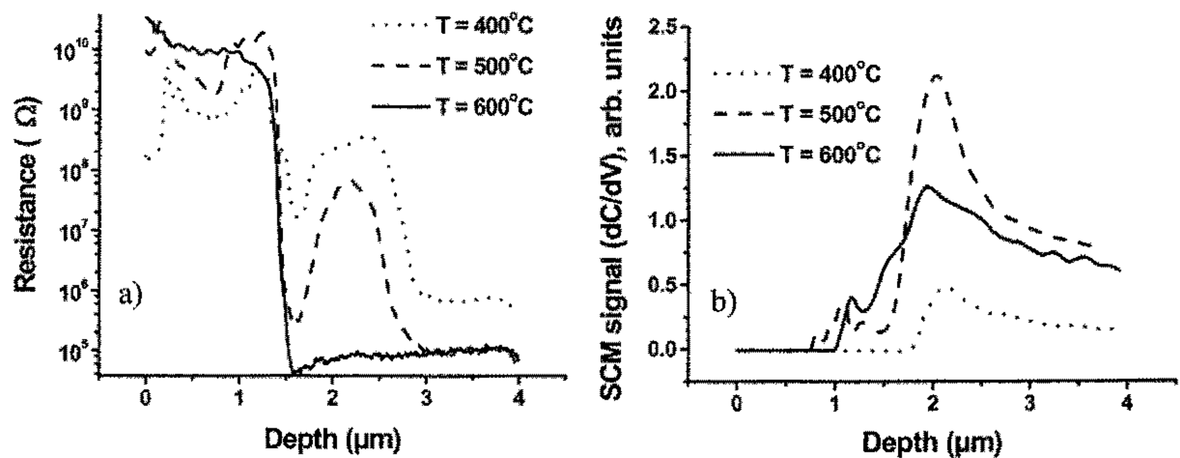

Figure 3.13 SSRM and SCM line scans obtained for the In ion implanted InP samples annealed at 400°C, 500°C and 600°C. (a) SSRM resistance profiles. (b) SCM profiles (dC/dV mode).

at high temperatures, thereby smoothing out the interface as far as electrical properties are concerned. The trends seen in the SCM data are also consistent with the overall conclusions obtained from SSRM. From these measurements it is clear that the recovery of electrical properties after annealing is highly (spatially) non-uniform. In the corresponding samples where Hall measurements have been performed, one can conclude that the measured mobilities would correspond primarily to the low resistance regions.

Similar measurements were performed on InP samples implanted with As, P and In ions. Although the overall features in the SSRM and SCM profiles obtained for the As ion implanted InP are similar to those found for Ga ion implanted samples, the latter case was invariably more resistive. For example, for 600°C annealing, the resistance in regions framing the maximum implantation peak was much lower in the As ion implanted sample compared to the Ga ion implanted sample; the observed resistances in these regions were nearly one order of magnitude lower than the doped substrate. This is consistent with the higher conductivity in Hall measurements obtained for the As ion case.

For the P ion implanted samples - at 500°C annealing and above - both SCM and SSRM show that most of the epitaxial layer, except close to the surface, is highly conducting. In this case there is only one (thicker) conducting layer, which is more or less centred around the depth of peak damage at 1μm. Thus, damage produced by implantation with P ions is sufficient to produce high concentrations of donors, whose auto-ionised electrons are not impeded even in the region of peak damage.

Drastically different results were obtained for the In ion implanted samples. Even at 600°C, the characteristic zero signal was obtained in the majority of the epilayer in SCM. Correspondingly, SSRM measurements show very high resistance. This appears to be in contradiction to Hall measurements. However, close to the implantation peak, a very low

resistance region was observed; its resistance is about five times lower than the substrate level. Such a region would form a highly conducting channel and explains the resistance data obtained in Hall measurements.

These results give detailed information about how the electrical characteristics are locally modified after annealing and how this modification depends on the implanted species. It would appear that the most conductive region is at a depth of 1.5 - 2 μm. This depth corresponds to the interfacial region in the samples prepared for SSRM and SCM.

These results give detailed information about how the electrical characteristics are modified by annealing or implantation with different elements. We see that for samples annealed at 400°C the epilayer is behaving like an insulator. For P ion implantation, annealing at 500°C creates a conductive layer which occurs at a depth of approximately 1 μm into the sample, and for annealing at higher temperatures this conductive region expands (which is consistent with the broadening of the defective regions after annealing seen in the XTEM scans). For Ga and As ion implantation, annealing at higher temperatures results in intriguing electrical characteristics, in that a double layer of conductivity is formed above and below the 1 μm mark; again for the highest annealing temperature these layers broaden and become more conductive. Given the known shallow donor formation in implanted and annealed InP, it is expected that the highest concentration of these donors would exist in the region of maximum damage. Thus, it makes sense that a layer of high conductivity would be formed at this depth, as is the case for P ion implants. The double conductive layer seen in the Ga and As ion implanted samples could be explained as follows: the donors are created in the highest concentration in the region of peak damage, but due to the large amount of scattering and trapping centres caused by implants with this ion, the mobility and carrier concentration at a depth of 1 μm is very low and thus the paths of least resistance lie above and below the

damage peak. For Ga ion implants, the overall resistance of the epi-layer remains relatively high and is consistent with the sheet resistances obtained from Hall measurements. In the case of In ion implants, the high resistance regions seen in SSRM (and SCM) in the majority of the epi-layer together with a very low resistance (narrow) region close to the implantation peak is once again consistent with the observed trends in Hall data.

Summary

Electrical characteristics measured by Hall effect followed the trends found in the structural studies, where similar behaviour was observed when P and In ion implants were done using doses scaled to give the same maximum damage; also similar characteristics were observed for P and As ion implants at doses to 10^{16} cm^{-2}. Logically, the electrical characteristics depend on the type and quantity of defects created by implantation with the various ions. Increasing the dose or annealing the damaged material caused the resistivity to drop sharply, due to the phenomenon of shallow-donor formation which was identified as being one of the most important characteristics of implanted InP. Amongst other native defects, it is most likely that this shallow donor takes the form of a P antisite. SSRM and SCM measurements have shown how a single conductive layer positioned at the depth of peak damage is created by implantation with P and annealing at 600°C. Two conductive layers centered around the region of maximum damage are created for implants with As and Ga ions, although annealing at 600°C in the former case causes these two conductive layers to merge into a single one. The double layers are explained by the high scattering of carriers in the region of maximum damage - which are otherwise produced at this same location – causing conduction to occur in the paths of least resistance which exist above and below this region. Damage produced by In

ion implants is greater and causes high resistivity throughout the region affected by the implanted ion.

3.5 Optical Studies

The optical properties of implanted InP can provide a great deal of information about traps within the material, as well as being of interest for potentially useful characteristics in optoelectronic devices. The implanted InP samples were studied both using time resolved photoluminescence (TRPL) and time resolved differential reflectance (TRDR). Time resolved photoluminescence allows us to obtain characteristic times for the removal of carriers from the conduction and valence bands (which is important for ultrafast photodetector applications). The damage caused by ion implantation results in a great number of traps within the bandgap, which, apart from enhancing the possibilities for nonradiative recombination, allow for much faster radiative recombination of the photogenerated carriers - via cascade mechanisms - than for undamaged material. Generally speaking, as-implanted material contains too many defects, resulting in recombination which is dominated by nonradiative processes, or else radiative recombination with characteristic lifetimes well below the detection limit of the experiments. Annealing allows for some recovery of the lattice, and hence, only those samples which had been annealed at the higher temperatures were chosen for optical analysis.

3.5.1 Dose dependence

Figure 3.14 shows the TRPL decay time of P-implanted p -type InP (carrier concentration ~ 3.4×10^{17} cm^{-3}) for different ion doses after annealing at 600°C for 30 seconds. The PL

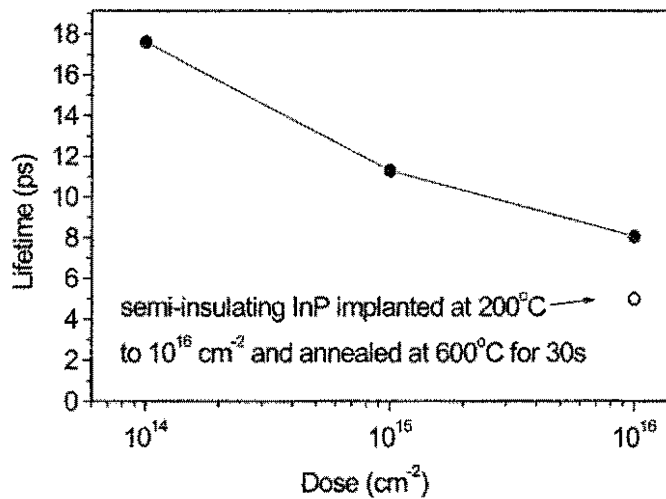

Figure 3.14 Plot of time resolved photoluminescence decay times as a function of dose for 1 MeV P ion implantation of p-InP (~3.4 x 10^{17} cm^{-3}) at 200°C, and subsequently annealing by RTA at 600°C for 30s. The value for 200°C 1 MeV P ion implantation into SI InP to a dose of 10^{16} cm^{-2} implantation into SI InP is also shown for comparison.

magnitude is proportional to the product of the free electrons and holes at the band edges, and its decay gives the most direct picture of carrier trapping. Time resolved photoluminescence on undoped or Fe:InP has yielded electron lifetimes of the order of hundreds of ps[17]. P-type material was used in this case as part of a study which will be presented in Chapter 6, however the decay times measured on this material are of a similar magnitude to the SI material, as shown in Figure 3.14. As the ion dose is increased, thereby causing more damage and creating a greater concentration of traps, the carrier lifetime decreases.

3.5.2 Implant element and annealing dependence

The relationship between the measured carrier lifetimes and implant ion mass, after annealing at 600°C and 700°C for 30 seconds, is depicted in the TRPL measurements on SI InP samples of Figure 3.15. Annealing at 700°C results in longer decay times than for annealing at the lower temperatures, as more defects are annealed out and consequently there are fewer trapping centres. In general, the lifetime does decrease with increasing ion mass, as would be expected since greater concentrations of defects have been correlated with shorter lifetimes, however the Ga ion implantation does not fit this pattern. Implantation with Ga ions produces the shortest decay times (0.66 ps at RTA 600°C), even though the mass of this ion is similar to As. The shorter decay time is consistent with the evidence of greater structural damage in the DCXRD spectra at these annealing temperatures, the high concentration of small clusters observed after annealing in the XTEM images, and the corresponding fact that the mobility at the same annealing temperatures does not reach the high values that it does for the other samples. Figure 3.15 once again illustrates the fact that the characteristics of the implanted material, in this case the decay times, do not scale with ion mass. A drawback in TRPL measurements is the high, compared to the band gap, excitation energy. This establishes long times for electron relaxation to the bottom of the band, which, in turn, results in long PL rise times and prolonged PL decay times. In a study on LT GaAs it was shown that, for ultrashort electron lifetimes, the process of electron scattering to the bottom of the band affects the PL transient, and the PL decay becomes considerably longer than the electron trapping time.[18]

Figure 3.16 presents the time evolution of normalised differential surface reflectivity (dR/R) of P and As ion implanted SI InP samples, for annealing at 700°C for 30 seconds.

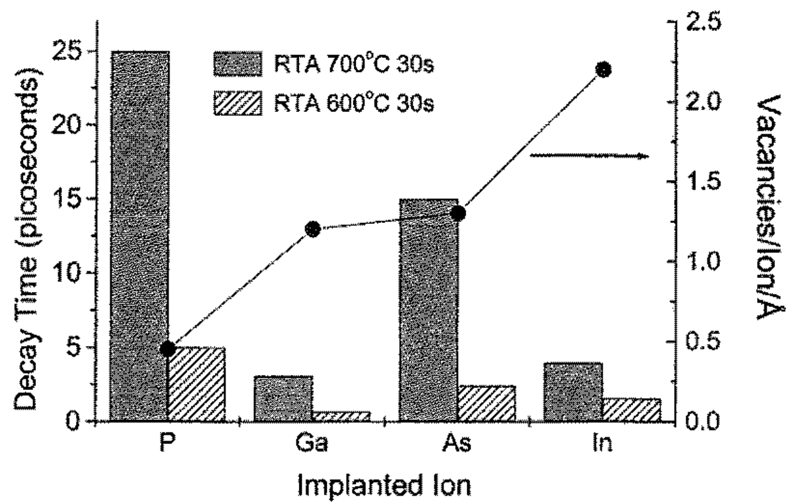

Figure 3.15 TRPL decay times measured at 300 K and simulated peak atomic displacements (TRIM) produced for P, As, Ga and In ion implanted SI InP.

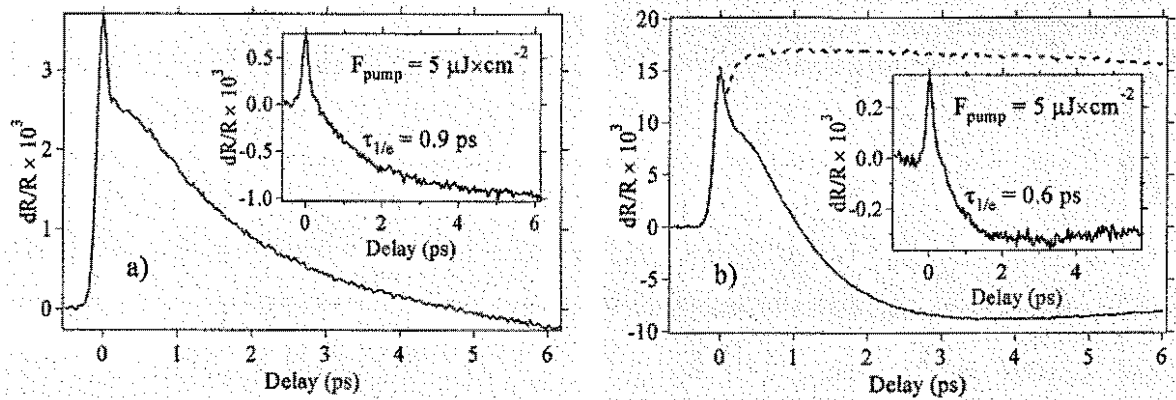

Figure 3.16 dR/R signals of P ion implanted (a), and As ion implanted (b) samples annealed at 700°C (unimplanted trace shown by dotted line). F_{pump} = 50 μJ x cm^{-2} corresponding to an injection density of ~2 x 10^{18} cm^{-3}. Insets show traces for F_{pump} = 5 μJ x cm^{-2}.

These measurements are done with an excitation energy equivalent to the bandgap, thus removing electron scattering considerations. Typically, these differential signals originate in the refractive index change Δn, induced by the optically generated carriers. Since the measurement wavelength (λ = 895nm) is shorter than the band gap wavelength (λ_{BG} = 917nm), Δn and dR/R are both positive. Comparing the signal from the unimplanted sample (dashed curve in 3.16(b)) with those from implanted samples illustrates the drastic change induced by ion implantation and annealing.

The initial peak in all cases corresponds to the pump-probe correlation, after which carriers thermalise, undergo cooling and trapping, and for long delay times (tens of ps - not shown), undergo recombination processes[19,20]. In the data, taken with a pump fluence of 50 μJ x cm^{-2}, there is a slight 'shoulder' visible following the pump-probe correlation peak. This may be attributed to hot carrier dynamics, induced by two photon absorption at high pump fluences (compare insets for low fluence excitation). Figure 3.16 clearly shows that even at high annealing temperatures traps still exist, in agreement with the DCXRD results. The data for low pump fluence (5 μJ x cm^{-2}) were normalised after the background values were subtracted, and the delays at which the dR/R value fell to 1/e were taken as characteristic trapping related response times. These were 0.9 ps in the P ion implanted case and 0.6 ps in the As ion implanted case.

In spite of the abovementioned advantages over TRPL, interpretation of TRDR transients is much more complicated than that of TRPL because the reflectivity is sensitive to changes both in the absorption coefficient and refractive index. In addition, TRDR measurements are sensitive not only to the bleaching effect induced by the band-to-band absorption, but also to changes in carrier concentration, free carrier absorption etc. On the

other hand, studies on LT GaAs have shown that the initial fast decay of TR transients is mainly determined by the carrier trapping.[21,22]

Summary

Response times for the implanted material, whether measured by time resolved photoluminescence or differential reflectance, decreased with decreasing annealing temperature and increasing dose. Unlike the electrical characteristics, the optical measurements provided information regarding deep trap formation as a result of implantation. As for the structural and electrical studies, it was found that the optical response times did not scale with ion mass. The shortest response times were for Ga ion implantation for annealing at 500°C, which corresponded well with the high density of small clusters observed in XTEM scans as well as the decreased mobility observed for implanting with this element in the Hall effect measurements.

3.6 Conclusion

As the X-ray and TEM experiments in this Chapter have revealed, a large density of defects exists in the samples after implantation that are arranged in layers, as expected from a non-uniform implant damage profile. The strain profile of these layers is modified by annealing, which allows for recrystallisation and agglomeration into clusters as well as migration of the original defects. The resulting defect profile is responsible for the optical and electrical properties measured in ion implanted and annealed InP. We have seen how the damage created in the samples depends critically on the implant species, and that Ga ion implantation,

with its production of closely spaced small clusters, results in unique electrical and optical characteristics.

One of the main electrical consequences of implantation into InP has been the formation of shallow donor-like levels, in particular the level associated with the P antisite. After implantation, the samples turn n-type and experience a decreased sheet resistance as the implantation dose and annealing temperature are increased, and at high doses and annealing temperatures exhibit electrical properties similar to LT InP. Thus both implantation and subsequent annealing allow for ever greater concentrations of shallow donors to form. The layered damage in the samples has in some cases resulted in multiple conductive paths through the samples, as was shown by SCM and SSRM measurements. Extended defects in the regions of maximum damage coincided with regions of high resistivity where conduction does not take place, though it is likely that these more complex defects correspond to a high concentration of deep traps. As far as the optical characteristics are concerned, it is these deep traps which control the response times, due to their role as recombination centers. For annealing at 600°C, it was possible to obtain subpicosecond lifetimes in the implanted samples.

References

1 F. W. Smith, A. R. Calawa, C.-L. Chen, M. J. Manfra, and L. J. Mahooney, IEEE Electron Device Lett. 9, 77(1988).

2 S. Gupta and J. F. Whitaker, IEEE J. Quantum Electron. **28**, 2464 (1992).

3 M. Kaminska and E. R. Weber, Mater. Sci. Forum **83-87**, 1033 (1992).

4 A. Claverie, F. Namavar, and Z. Lilienthal-Weber, Appl. Phys. Lett. **62**, 1271 (1993).

5 A. Krotkus, S. Marcinkevicius, J. Jasinski, M. Kaminska, H. H. Tan and C. Jagadish, Appl. Phys. Lett **66**, 3304 (1995).

6 S. Takagi, Acta Cryst., **15**, 1311 (1962), S. Takagi, J. Phys. Soc. Japan, **26**, 1239 (1969); D. Taupin, Bull. Soc. Fr. Mineral. Cristallogr., **87**, 469 (1964)

7 A. Gasparotto, A. Carnera, C. Frigeri, F. Priolo, B. Fraboni, A. Camporese, and G. Rosetto, J. Appl. Phys. **85**, 753 (1999).

8 E. Wendler, T. Opfermann, and P. I. Gaiduk, J. Appl. Phys. **82**, 5965 (1997).

9 W. M. Chen, P. Dreszer, A. Prasad, A. Kurpiewski, W. Walukiewicz, E. R. Weber, E. Sörman, B. Monemar, B. W. Liang, and C. W. Tu, J. Appl. Phys. **76**, 600 (1994).

10 S. Marcinkevičius, C. Jagadish, H. H. Tan, M. Kaminska, K. Korona, R. Adomavičius, and A. Krotkus, Appl. Phys. Lett. **76**, 1306 (2000).

11 B.W. Liang, P. Z. Lee, D. W. Shih, and C. W. Tu, Appl. Phys. Lett. **60**, 2104 (1992).

12 B.W. Liang, P. Z. Lee, D. W. Shih, and C. W. Tu, J. Appl. Phys. **76**, 600 (1994).

13 M. Alatalo, R.M.Nieminen, M. J.Puska, A. P.Seitsonen, and R. Virkkunen, Phys. Rev. B **47**, 6381 (1993).

14 S. Radautsan, I. Tiginyanu, and N. Pyshnaya, Phys. Stat. Sol. (a), **108B**, K59 (1988).

15 K. Kuriyama, S. Satoh, K. Sakai and K. Yokoyama, Nucl. Instr. And Meth. in Phys. Res. B **127/128**, 456 (1997).

16 C. C. Williams, Ann. Rev. Mater. Sci. **29**, 471-504 and references therein, (1999).

17 A. Gaarder, S. Marcinkevicius, E. Rodriguez Messmer, and S. Lourdudoss, J. Crystal Growth, **226**, 451 (2001)

18 B. Mari, M. A. Hernandez-Fenollosa, and F. J. Navarro, J. Appl. Phys., **89**, 7772 (2001)

19 B. M. Keyes, D. J. Dunlavy, R. K. Ahrenkiel, G. Shaw, G. P. Summers, N. Tzafaras, and C. Lentz, J. Appl. Phys. **75**, 4249 (1994)

20 J. Shah, "Ultrafast Spectroscopy of Semiconductors and Semiconductor Nanostructures." Heidelberg, Germany: *Springer*, (1996).

21 J.-F. Roux, J.-L. Coutaz, and A. Krotkus, Appl. Phys. Lett. **74**, 2462 (1999).

22 A. Krotkus, K. Bertulis, M. Kaminska, K. Korona, A. Wolos, J. Siegert, S. Marcinkevicius, J.-F. Roux, and J.-L. Coutaz, IEE Proc. Optoelectronics, **149**, 111 (2002).

CHAPTER 4

Electrical Isolation of *n*- and *p*-InGaAs

4.1 Introduction

A study into the nature of defective InGaAs is essential for accumulating a base of knowledge from which defect engineering in this material can be developed. This Chapter focuses on the electrical characteristics of implanted InGaAs, and deals with the issues that are encountered when trying to maximise the resistivities using this technique of damage creation. Devices such as photoconductive detectors, guard rings and field-effect transistors are some examples of the applications where high resistivity InGaAs could be put to good use[1,2]. However, the electrical properties of defective InGaAs pose some problems when it comes to creating a highly resistive material. Similarly to InP, undoped InGaAs is n -type with 10^{14}-10^{16} cm^{-3} inadvertent donors[3], and Fe doping during wafer growth is necessary to make the material semi-insulating (SI). Apart from doping, high resistivities can also be achieved at the post-growth stage by using light ion implantation, where free carriers can be trapped by implant-induced deep levels that are not thermally ionised at device operating temperatures. Ion implantation provides a method whereby regions on a wafer or device can be electrically 'isolated' with precise depth control, and offers an alternative to mesa etch technology while also being compatible with planar technology. Studies into isolation have already investigated GaAs[4-7], AlGaAs[8], GaN[9] and InP[10,11], and provide quite different results in terms of the maximum achievable resistivity depending on the intrinsic characteristics of each semiconductor. In the case of GaAs, resistivities greater than 10^7 ohm.cm have been produced by implanting n - or p - type layers with ions such as H, B or O[12]. Isolation of n -InP has achieved maximum resistivities of the order of 10^4 ohm.cm[13-15]. p -InP has been isolated with maximum resistivities of 10^7 ohm cm, although the implant dose was found to be critical because above the maximum isolation dose, the implant induced donor levels reduce the

resistivity to the 10^3 to 10^4 ohm.cm range[13,16,17]. To explain this limiting value that occurs for both n - and p -InP, it has been postulated that donors and acceptors are created by the ion bombardment[13,18].

Qualitatively similar results have been obtained with implant damage in InGaAs[19-22]. Because of its small band gap (0.74 eV at 300K), resistivities as high as in GaAs or p - InP are not expected to be achievable in InGaAs. The highest attainable room temperature resistivity in Fe or Cr doped InGaAs is only of the order of 10^3 ohm cm due to this low band gap and high intrinsic carrier concentration (n_i ~9 x 10^{11} cm^{-3} at 300K, considering m^*_e/m_o=0.0041 and m^*_h/m_o=0.5)[22]. Arsenic antisites in InGaAs create shallow donors and, together with other intrinsic defects such as an As vacancy and a group III (In or Ga) interstitial, prevent fabrication of highly-resistive InGaAs layers by low-temperature growth[23]. Steeples *et al.*[24] reported resistivities greater than 10^4 ohm.cm in $In_{0.53}Ga_{0.47}As$ as a result of proton or deuteron bombardment, but otherwise efforts to isolate InGaAs using multiple ion bombardments have resulted in resistivities which do not exceed the value of the Fe doped material.

Multiple implants have been used extensively in isolation studies because of the 'box' damage profile which can be created with this method. An alternate method is to use single implants at ion energies which place the peak of the damage profile well into the substrate, such that the epilayer of interest lies in the relatively uniform 'tail' of the profile. There are advantages to both methods. Single implants, in their simplicity, are ideal from a device manufacturing point of view. Moreover, this technique allows for *in situ* measurement of resistivities as a function of cumulative dose, whereby the optimum dose for isolation can be pinpointed. This technique is ideal when the substrate material remains semi-insulating after implantation. Multilayer implants have been used exclusively, and with good reason, when investigating InGaAs epilayers, because the InP substrates they are inevitably grown on

become n-conductive when implanted. Thus the multiple implants have been done at energies which locate all of the damage in the InGaAs epilayer. However, this method does not allow for thorough *in situ* studies of dose dependence. Annealing can be used to modify the post-implant resistivities, but is complicated by the added shallow donor formation which occurs when implanted InGaAs is annealed (similarly to InP).

Keeping the above issues in mind, we have chosen in this work to apply the single implant technique into n- and p- InGaAs epilayers grown on InP substrates.

4.2 Experimental

Three 0.5 μm p-$In_{0.53}Ga_{0.47}As$ epilayers were grown with free carrier concentrations of ~3.5 x 10^{17}, 8 x 10^{17} and 7.8 x 10^{18} cm^{-3} on semi-insulating (100) InP substrates. Similarly, three n-$In_{0.53}Ga_{0.47}As$ epilayers were grown with carrier concentrations of ~5 x 10^{16}, 2.7 x 10^{17} and 1.2 x 10^{18} cm^{-3}. The room temperature sheet resistance of the samples was measured *in situ* in the absence of light after ion irradiation of C, O, Li and H ions with energies of 2, 2, 0.7 and 0.6 MeV respectively, with the samples tilted at 7° from the normal direction of the beam to minimise channeling effects. At these implant energies, the peak damage lies 2 μm below the surface for C, O and Li, and 6 μm for H ion implantation; in other words the ions penetrated through the InGaAs and well into the InP substrate, thereby creating a uniform damage distribution in the epilayer. Using the data from these experiments, new samples were irradiated at specific doses and then underwent a cumulative annealing process to analyse the thermal stability of the electrical defects.

4.3 *p* - InGaAs

Figure 4.1 (a) shows the evolution of the sheet resistance, R_s, in *p* -InGaAs samples with an initial free carrier concentration of $\sim 8 \times 10^{17}$ cm^{-3}, during implantation with O, C, Li and H ions. As the mass of the implanted ion is decreased, the dose required to isolate the material increases.

For implants with O, C and Li ions, there is a sharp rise in R_s to its maximum at the critical dose, D_{Cr}, with a steep drop off for higher doses. Rao *et al.*[22] also found a very close compensation trend when implanting H, He and B ions into *p* - InGaAs, although their maximum values of R_s were one or two orders of magnitude lower than what we have achieved here. Moreover, Rao *et al.* showed that for implants with these three ions, a kind of parallel decrease in R_s occurred beyond the critical dose which can also be seen for implants with O, C and Li ions in Figure 4.1. This is unlike typical isolation work done on other semiconductors such as GaN or AlGaAs[8,9], where beyond the critical dose, there is a dose range where the sheet resistance remains fairly constant as the dose is increased. Such a plateau in sheet resistance can be achieved when implanting into semiconductors whose implant-induced defects act solely as carrier traps, and the value of the measured resistance in the plateau region results from the parallel association of the isolated layer resistance and that of the SI substrate. The similarity between this work, and that of others where multiple-energy implants were done such that the substrate was not damaged, excludes contributions from the InP substrate as a possible explanation for the results. Besides, in work done on implanted InP by Boudinov *et al*[10]., a plateau with high sheet resistivities was seen in both *n* - and *p* - type

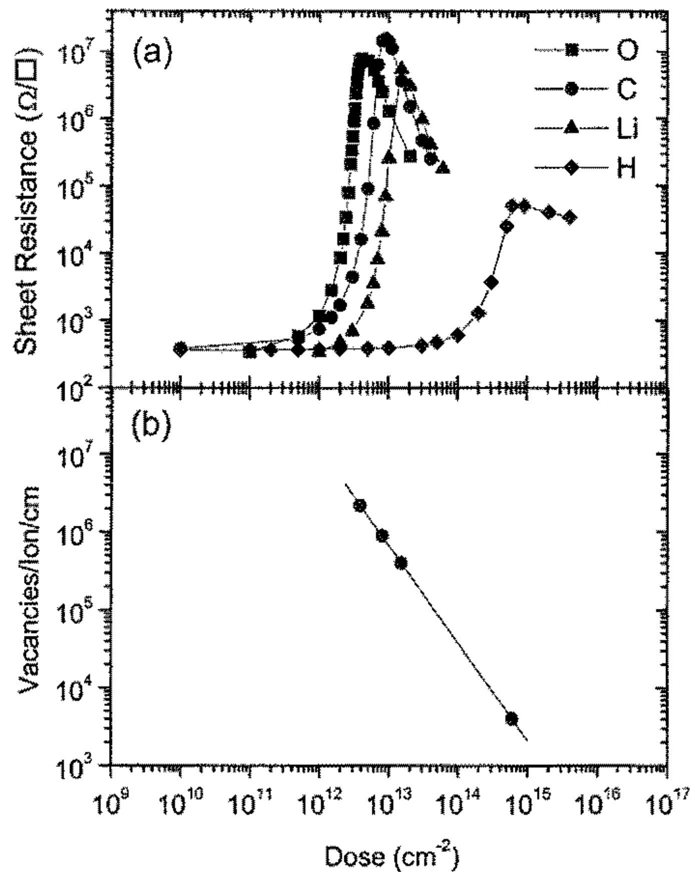

Figure 4.1 (a) Dose dependence of sheet resistance of *p*-InGaAs samples with an initial free hole carrier concentration of ~ 8 x 10^{17} cm^{-3}, irradiated with 2 MeV C, 2 MeV O, 0.7 MeV Li and 0.6 MeV H ions, with a beam flux of 24 nA/cm^2. (b) The estimated vacancies/ion/cm calculated using TRIM vs critical dose obtained from data in (a), with a linear best fit of slope ~0.8.

material for much higher doses than D_{Cr}, which indicates that contributions from a conducting region located deep in the InP substrate are unlikely. Rao *et al.*, via mobility measurements and measurement of the carrier concentration profiles as a function of depth, concluded that the sharp decrease in R_s was due to swamping of the *p*-InGaAs with electrons caused by shallow donors. Our calculations indicate that the damage created in InGaAs, which

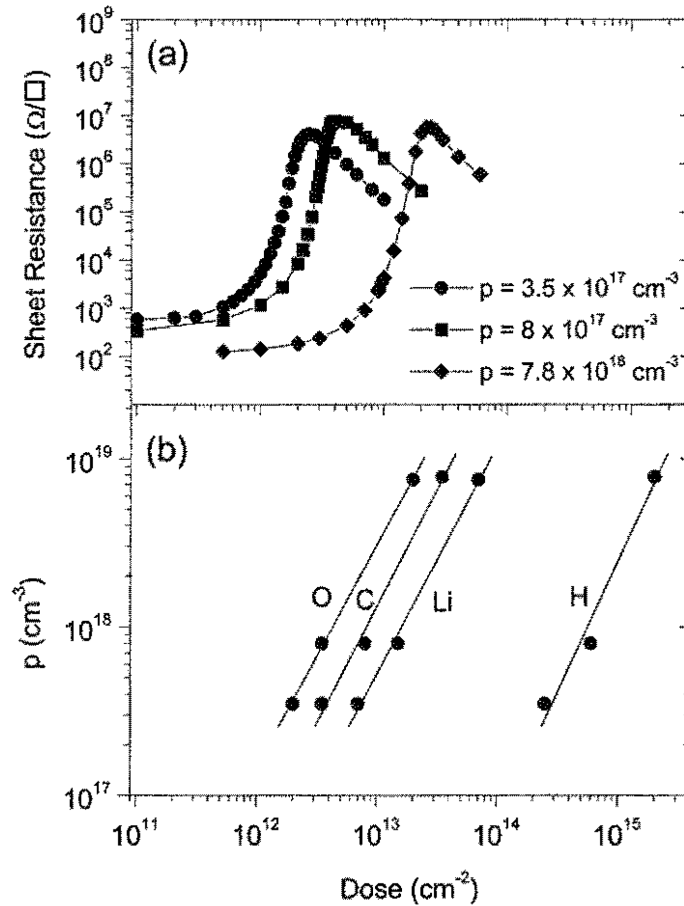

Figure 4.2 (a) Dose dependence of sheet resistance of p -InGaAs samples with different initial free hole carrier concentrations, irradiated with 2 MeV O ions with a beam flux of 24 nA/cm^2. (b) Original free carrier concentration of the samples vs critical dose obtained from data in (a), as well as for similar implants done with 2 MeV C, 2 MeV O 0.7 MeV Li and 0.6 MeV H ions (including linear fits with slopes of ~0.7 for C, O and Li ions, and ~0.6 for H ions).

sits in the tail of the profile for implants with O, C and Li ions, is similar to what would have been created using the multiple implant scheme of Rao *et al.* Hence we conclude that n-carrier swamping in the epilayer is the likely cause of the decrease in R_S.

H ion implantation presents a slightly different case. As expected for such a light ion, D_{Cr} has a very high value, with a maximum value of R_s that is more than two orders of magnitude less than what can be achieved by implantation with the other ions. The decrease in sheet resistance beyond D_{Cr} is much gentler as well. The different dependence of R_s on dose beyond D_{Cr} may be due to a different type of damage induced by the higher doses that are needed to achieve isolation with this ion. On the one hand, at the higher doses, it is expected that clusters and other complex defects would be created in abundance, while at the lower doses it is expected that point defects are the main type of damage. On the other hand, H is such a light ion that dynamic annealing is expected to be very strong in the semiconductor, which may mean that complex defects are prevented from forming except at extremely high doses. It is interesting to note that in previous work on both GaAs and InP, there were indications that hydrogen-induced damage is different and less effective than damage produced by medium mass ions such as deuterium, helium, boron and beryllium[14,24,25-27]. For example, for H ion doses as high as 10^{17} cm^{-2}, no extended defects were observed by transmission electron microscopy in GaAs prior to annealing[28,29].

Figure 4.1 (b) plots the estimated vacancies/ion/cm (as calculated from TRIM simulations) vs critical dose, D_{Cr}, and gives an indication of the linear relationship between the mass of the implanted ion and D_{Cr}. The slope calculated from the best fit is approximately 0.83. This value differs slightly from the slope of ~ 1 that was calculated by Boudinov *et al.*[10], but again this difference is expected to be due to the contribution from the shallow donors.

Figure 4.2 (a) depicts the dose dependence of the sheet resistance R_s of p -InGaAs samples irradiated with 2 MeV O ions only. If the initial free carrier concentration is increased, a higher dose is required to isolate the material. Figure 4.2 (b) plots the linear relationship between initial free carrier concentrations of the samples and D_{Cr} as determined from the C, O,

Li and H ion implants. For C, O and Li ion implantation, the slope calculated from the best fit is ~0.7, and for H ion implantation it is ~0.6.

Figure 4.3 shows the thermal stability of defects introduced by H, Li, C and O ion implantation at a variety of doses around the D_{Cr} for each ion, as determined by cumulative rapid thermal annealing. All anneals were carried out for 60 second intervals. The maximum annealing temperatures for which R_s remained high were 350°C for O ion implantation, 300°C for C and Li ion implantation, and 200°C for H ion implantation. At the higher doses, more complex defects, having a higher thermal stability, are created, thus electrical isolation of the samples is more thermally stable when created by implanting at higher doses. In keeping with this picture, the thermal stability of the defects responsible for isolation decreases with decreasing ion mass, as once again it is expected that ions of greater mass will produce more complex defects than those of smaller mass such as H.

As has been found for isolation of GaAs and InP, both donor and acceptor levels are created during implantation, which, depending on whether the material is initially p - or n - type, provide the carrier traps and cause the isolation. In the case of InGaAs, the types of point defects caused by the disordered lattice and which could be donors are: an arsenic vacancy, group III (In or Ga) interstitials, or an arsenic antisite[22]. Energy levels associated with the As antisite have been measured approximately 0.032 eV below the conduction band (0/+) in InGaAs[23] and in analogy with GaAs a deeper donor level is expected approximately 0.26 eV below that. An increase in n - conductivity which has been found for ion implanted InGaAs can be associated with the formation of shallow donors such as the 0.032 eV level due to the As antisite. The deeper donor levels created by these same point defects will be the ones

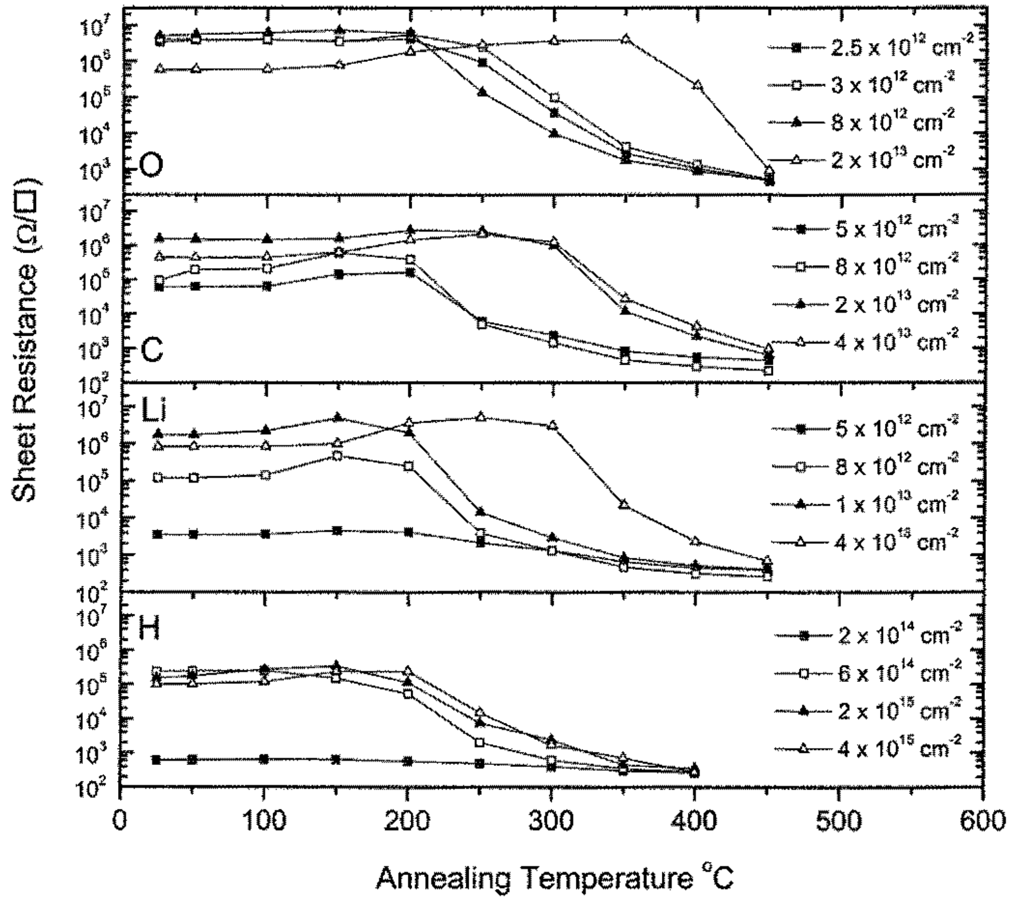

Figure 4.3 Isochronal annealing stability of sheet resistance for *p*-InGaAs (*p* ~8 x 10^{17} cm^{-3}) epilayers implanted at a range of doses above and below D_C for 2 MeV O, 2 MeV C, 0.7 MeV Li, and 0.6 MeV H ion implantation.

behaving as hole traps in the case of *p*-InGaAs. A DLTS study by Pelloie *et al.*[30] of a *p*-$In_{0.53}Ga_{0.47}As$ layer found a majority carrier trap (hole trap) with activation energy 0.08 eV. Rao *et al.*[22] and Kunzel *et al.*[23] have both reported the presence of a donor with an energy of ~43 - 50 meV below the conduction band edge for low temperature grown InGaAs, which has been associated with excess As and therefore could also be due to the As antisite.

In addition to point defects, more complex defects such as clusters and loops are expected to be produced in abundance during ion implantation, especially for the higher doses; these will also play a role in the trapping of majority carriers. Unfortunately such defects have been too complex to treat with modelling techniques at the time of writing, and any deep levels measured in studies such as DLTS and caused by these defects have remained unidentified.

Summary

Isolation of *p*-InGaAs epilayers achieved maximum resistivities of ~ 10^7 Ω/□ for single implants with O, C and Li, after which R_s decreased due to the onset of *n*- carrier swamping. This effect also had the characteristic of a parallel decrease in R_s beyond the critical dose. H ion implants achieved much lower maximum values for the sheet resistance because isolation was truncated by a different *n*- carrier swamping at the high doses. The linear dependence of the vacancies/ion/cm on threshold dose had a slope of ~0.8, and that of the initial free carrier concentration had a slope ~ 0.7 (O, C and Li ion implants) or ~ 0.6 (H ion implant), respectively. The thermal stability of defects responsible for the isolation was much lower than was found for isolation in other materials such as GaAs, and increased with increasing dose and also implant ion mass.

4.4 *n* - InGaAs

A similar series of experiments was performed for 0.5 μm *n* - InGaAs epilayers with carrier concentrations of 5×10^{16}, 2.7×10^{17} and 1.2×10^{18} cm^{-3}. Figure 4.4 shows the corresponding results for implantation with O, C and Li and H ions into samples with $n \sim 2.7 \times 10^{17}$cm^{-3}. Once again, decreasing the implant ion mass results in a higher threshold dose. The maximum values of R_s achievable by implantation into *n* - InGaAs are of the order of 6×10^4 Ω/□, which is three orders of magnitude less than with *p* – InGaAs. This is due to the shallow donor formation within the epilayer. This behaviour is similar to what was found in isolation experiments with InP[10]. The increase of R_s with increasing implant dose is much more gradual than for isolation of *p* - InGaAs, as is the decrease of R_s beyond the critical dose (except for H). This is because the isolation of *n* - InGaAs is purely dependent on the formation of deep acceptors, which must also trap the electrons caused by shallow donor formation. Of the possible point defects, cation vacancies and antisites are expected to play a role in this regard[31,32]; acceptor levels can also be formed by more complex defects (as yet unidentified in the literature). $D_{C\alpha}$ is higher by approximately an order of magnitude for implantation with the same ion at the same energy when comparing *n* - InGaAs to *p* -InGaAs, reflecting the slower accumulation of deep acceptors with increasing dose. The slope calculated from a linear fit of the vacancies/ion/cm versus threshold dose depicted in Figure 4.4 (b) in this case is slightly above 1, but again the effect of the shallow donors is expected to be influencing the results.

We have seen that for *p* -InGaAs, a sharp decrease in R_s for heavier ion implants was associated with hopping conduction, and a shallow decrease for H ion implants was associated with *n* - carrier swamping. It would seem that for *n* - InGaAs the opposite effect has occurred,

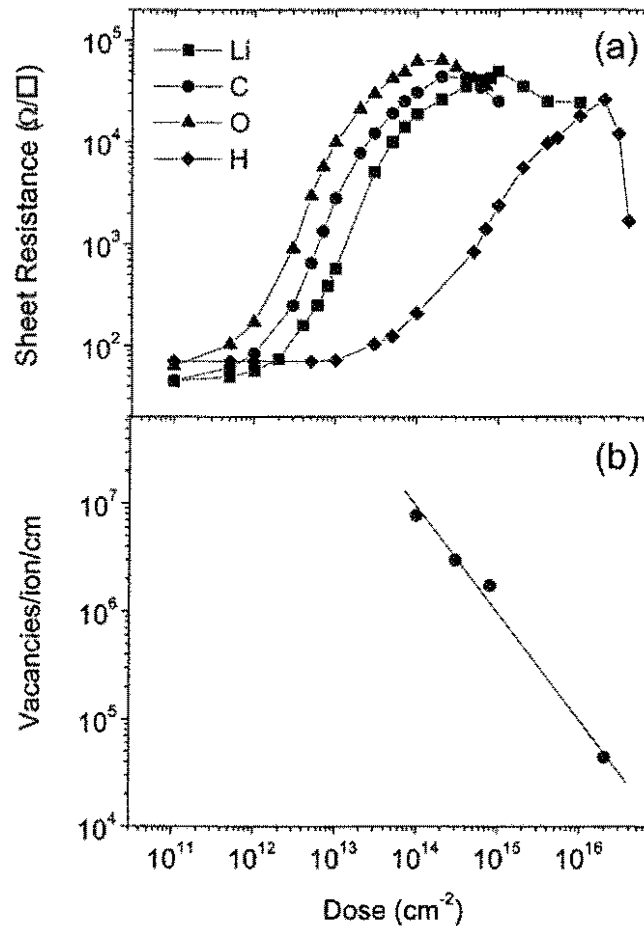

Figure 4.4 (a) Dose dependence of sheet resistance of n-InGaAs samples with an initial free electron carrier concentration of ~ 2.7 x 10^{17} cm^{-3}, irradiated with 2 MeV C, 2 MeV O, 0.7 MeV Li and 0.6 MeV H ions, with a beam flux of 24 nA/cm^2. (b) The estimated vacancies/ion/cm calculated using TRIM vs critical dose obtained from data in (a), with a linear best fit of slope ~1.

with a shallow decrease in R_s for heavier ion implants, and a sharper decrease for H ion implants. H ion implantation resulted in similar maximum values of R_s at the critical dose as for p - type material, and this maximum value is comparable to that achieved by implantation with the medium mass ions. Extremely large doses are required to achieve isolation in n -

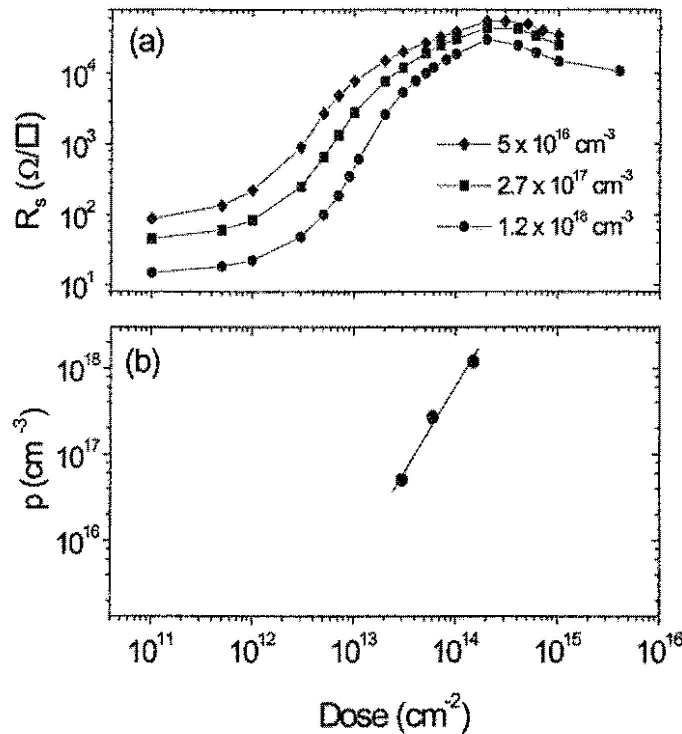

Figure 4.5 (a) Dose dependence of sheet resistance of *n*-InGaAs samples with different initial free electron carrier concentrations, irradiated with 2 MeV C^+ ions with a beam flux of 24 nA/cm^2. (b) Original free carrier concentration of the samples vs threshold dose obtained from data in (a).

InGaAs by H ion implantation; above a dose of 10^{16} cm^{-2}, R_s drops off sharply. At such large doses it is likely a very large concentration of defects has been created and possibly a hopping conduction mechanism has dominated the electrical characteristics at these doses.

Figure 4.5 shows the results of C ion implantation into *n*- InGaAs layers with differing initial free carrier concentration. The critical dose increases very slightly and the maximum value of R_s decreases with increasing initial free carrier concentration. The slope calculated from the linear best fit in Figure 4.5 (b) is 0.5.

Figure 4.6 shows the effect of cumulative annealing on samples that were implanted at specific doses above and below the critical value. As for *p*- InGaAs, the thermal stability of

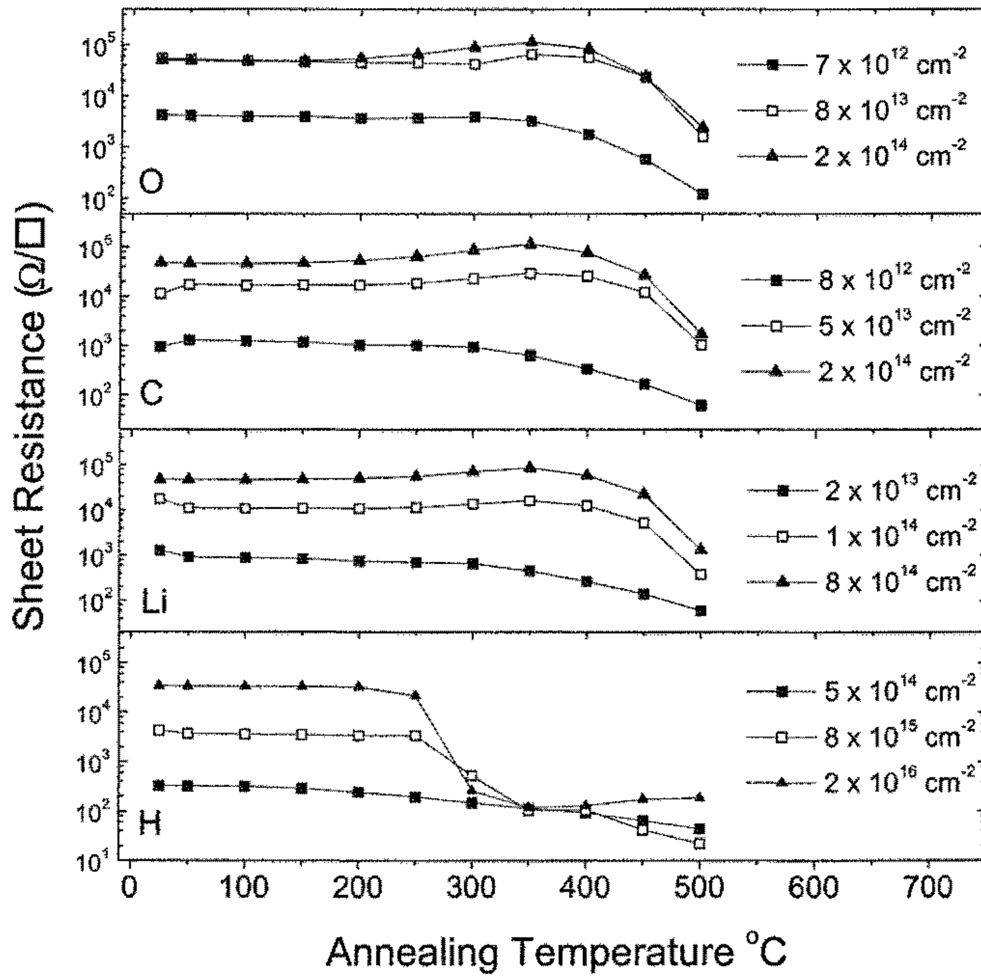

Figure 4.6 Isochronal annealing stability of sheet resistance for *n*-InGaAs (*n* ~ 2.7 x 10^{17} cm^{-3}) epilayers implanted at a range of doses above and below D_{Q} for 2 MeV O, 2 MeV C, 0.7 MeV Li, and 0.6 MeV H ion implantation.

defects created by implantation with ions of low atomic mass is less than for implantation with ions of high atomic mass. For implantation with the same ion, the thermal stability is greater for *n* - InGaAs, but this also reflects the higher doses required to achieve isolation. Defects were stable up to 450°C for O, 400°C for C and Li and 250°C for H ion implants.

Summary

Isolation of *n* -InGaAs epilayers achieved maximum resistivities of ~10^4 - 10^5 Ω/□ for single implants with C, O Li ions and after which R_s decreased due to the onset of shallow donor swamping; the samples remained *n* - type for all doses. Higher doses were required to isolate the material when compared to *p* - InGaAs. H ion implantation required doses exceeding 10^{16} cm^{-2} to isolate the material, above which the material became heavily damaged and R_s decreased sharply, most likely due to hopping conduction. The linear dependence of the vacancies/ion/cm on threshold dose had a slope of ~ 1.1 and that of the initial free carrier concentration has a slope of ~ 0.5. The thermal stability of defects was similar to that for implants into *p* -InGaAs, though slightly higher due to the higher doses required for isolation in this case.

4.5 Conclusion

Higher resistivities are achievable by implantation into *p* -InGaAs as compared to *n* -InGaAs epilayers on InP, due to the shallow donor formation which occurs when implanting into these materials. In general the thermal stability of defects responsible for isolation is much lower than for isolation of GaAs or *p* - InP, although this does not present a serious issue at normal device operating temperatures. While slightly higher thermal stability can be achieved for

implanting into the *n* - type material, better electrical isolation is obtained in the *p* - type material. Interestingly, the values of R_s obtained here are an order of magnitude greater than those measured by many others[11,19,22] who have used multiple energy implantation techniques. This shows the advantage of the single energy implant scheme, where the peak damage is located in the substrate, since the possibility of *in situ* resistance measurements allows optimization of the implant dose for maximum isolation in both *n* - and *p* - InGaAs epilayers. All indications are that a contribution from the InP substrate is not significant. Using this method has allowed us to thoroughly investigate the dose dependence of implant induced isolation in the InGaAs-on-InP system.

References

1. C. Y. Chen, and G. C. Chi, Appl. Phys. Lett. **45**, 1083 (1984)
2. P. M. Downey and B. Tell, J. Appl. Phys. **56**, 2672 (1984)
3. B. Tell, U. Koren, and B. I. Miller, J. Appl. Phys. **61**, 1172 (1986)
4. P.N.K. Deenapanray, Q. Gao, and C. Jagadish, J. Appl. Phys. **93**, 9123 (2003).
5. J. P. de Souza, I. Danilov and H. Boudinov, J. Appl. Phys. **81**, 650 (1997) and **84**, 4757 (1998)
6. S. Ahmed, R. Gwilliam, and B. J. Sealy, Semicond. Sci. Technol. **16**, L28 and L64 (2001)
7. S. Ahmed, R. Gwilliam, and B. J. Sealy, Nucl. Instrum. Methods B. **188**, 196 (2002)
8. T. von Lippen, H. Boudinov, H. H. Tan, C. Jagadish, Appl. Phys. Lett. **80**, 264 (2002).
9. S.O. Kucheyev, H. Boudinov, J. S. Williams, C. Jagadish, G. Li, J. Appl. Phys. **91**, 4117 (2002).
10. H. Boudinov, H. H. Tan, C. Jagadish, J. Appl. Phys. **89**, 5343 (2001)
11. S.J. Pearton, C. R. Abernathy, M. B. Panish, R. A. Hamm, and L. M. Lunardi, J. Appl. Phys. **66**, 656 (1989)
12. J. P. de Souza, I. Danilov, and H. Boudinov, Appl. Phys. Lett. **68**, 535 (1996)
13. J. P. Donnelly and C. E. Hurwitz, Solid-State Electron. **20**, 727 (1977)
14. P. E. Thompson, S. C. Binari, and H. B. Dietrich, Solid-State Electron. **26**, 805 (1983).
15. M.C. Ridgway, R. G. Elliman, M. E. Faith, P. C. Kemeny, and M. Davies, Nucl. Instrum. Methods Phys Res. B **96**, 323 (1995)
16. M. W. Focht and B. Schwartz, Appl. Phys. Lett. **42**, 970 (1983)
17. M. C. Ridgway, C. Jagadish, R. G. Elliman and N. Hauser, Appl. Phys. Lett. **60**, 3010 (1992)

18. J. D. Woodhouse, J. P. Donnelly and G. L. Tseler, Solid-State Electron. **31**, 13 (1988)

19. B. Tell, K. F. Brown-Goebeler, T. J. Bridges, and E. G. Burkhardt, J. Appl. Phys. **60**, 665 (1986)

20. J. Barnard, C. E. C. Wood, and L. F. Eastman, IEEE Electron. Device Lett. **EDL-2**, 193 (1981)

21. B. Tell, T. Y. Chang, K. F. Brown-Goebeler, J. M. Kuo and N. J. Sauer, J. Appl. Phys. **64**, 3290 (1988)

22. M. V. Rao, R. S. Babu, H. B. Dietrich, and P.E. Thompson, J. Appl. Phys. **64**, 4755 (1988)

23. H. Künzel, J. Böttcher, R. Gibis, and G. Urman, Appl. Phys. Lett. **61**, 1347 (1992).

24. K. Steeples, I. J. Saunders, and J. G. Smith, IEEE Electron Device Lett. **EDL-1**, 72 (1980)

25. M. W. Focht, A. T. Macrander, B. Schwartz, and L. C. Feldman, J. Appl. Phys **55**, 3859 (1984)

26. P. M. Downey and B. Tell, J. Appl. Phys. **56**, 2672 (1984)

27. P. M. Downey, R. J. Martin, R. E. Nahory, and O. G. Lorimor, Appl. Phys. Lett. **46**, 396 (1985)

28. H. C. Snyman and J. H. Neethling, Radiat. Effects **60**, 147 (1982); **69**, 199 (1983)

29. D. K. Sadana, J. M Zavada, H. A. Jenkinson, and T. Sands, Appl. Phys. Lett. **47**, 691 (1985)

30. J. L. Pelloie, G. Guillot, A. Nouailhat, and A. G. Antolini, J. Appl. Phys. **59**, 1536 (1986)

31. A. Amore Bonapasta and P. Giannozzi, Phys. Rev. Lett. **84**, 3923 (2000)

32. W. Pötz and D. K. Ferry, Phys. Rev. B **31**, 968 (1985)

CHAPTER 5

Ion Implanted InP for Ultrafast Photodetector Applications

5.1 Introduction

Ultrafast processes in semiconductors hold the key to the development of next generation optoelectronic devices. Ever since the fabrication of the first terahertz laser sources in 1983, photodetectors with the capacity to process pulses within picoseconds have been needed. Terahertz imaging is a field which continues to grow rapidly because of its large number of uses, which include high-resolution spectroscopy, atmospheric and astrophysical remote sensing, and imaging with unique contrast mechanisms. Apart from this, optical communications, the internet, broadcasting and computing now demand enormous bandwidths such that future devices will need to respond on picosecond (10^{-12}s) or even femtosecond (10^{-15}s) timescales.

The potential of defective semiconductors as materials for use in ultrafast photodetectors was first realised in 1988, when it was discovered that low temperature grown GaAs (LT- GaAs), after annealing, had sub-picosecond optical responses as well as high sheet resistivities and good mobilities[1-3].

Good mobilities within a photodetector are necessary for transport of carriers from the region where they are photogenerated, to the region where they are collected as electrical signals. High sheet resistivities are essential for making devices with low leakage or dark currents, which will then be more sensitive to low intensity optical signals and less susceptible to heat fatigue.

Naturally, InP is one of the ideal semiconductors to choose for the latter application, because its bandgap allows operation at infrared wavelengths (~900 nm, which can be used in plastic optical fibre communications for metropolitan and access networks) and because it is widely used as a substrate for InGaAs photodetectors. However, for ion implanted InP to be

useful as a material for ultrafast photodetectors, its shallow donor-like levels discussed in Chapter 3 must be compensated for, while maintaining the characteristics of high electron mobility and very short carrier lifetimes. Two ways of achieving exactly that are described in this chapter.

5.2 Experimental

Both semi-insulating (SI) InP and p -type InP wafers were used for this work. In the former case, samples were implanted with 2 MeV Fe^+ ions at 200°C to doses between 10^{13} and 10^{16} cm^{-2}, followed by annealing at temperatures between 500 and 900°C for 30 seconds. In the latter case, a 1.5-μm thick p -InP (p ~ 1.3×10^{18} cm^{-3}) layer was grown on a similar semi-insulating (100) InP substrate, and implanted at 200°C with 1 MeV P^+ ions to doses between 10^{12} and 10^{16} cm^{-2} and also annealed at 500 and 600°C for 30 seconds. As for previous experiments, the ion energies were selected to locate the peak damage 1 µm below the surface.

Structural, electrical and optical properties were measured using the same techniques as described in the experimental section of Chapter 3, however the setup for the optical measurements was slightly different. Time resolved photoluminescence measurements were performed at room temperature using an up-conversion set-up based on a self mode-locking Ti: sapphire laser (80 fs, 95 MHz, 770 nm). The average excitation intensity was between 1 and 100 mW, a spot diameter ~ 20 μm, which corresponds to a photoexcited carrier density between 1.1×10^{17} and 1.1×10^{19} cm^{-3}, respectively, when reflection losses and averaging over one absorption length are taken into account. The temporal resolution of the measurements was 130 fs. The PL transients were measured within a spectral window of 20 nm centered at the band gap wavelength of 920 nm.

5.3 MeV Fe ion implants into SI-InP

Nominally undoped InP is n- type[4], and one way of compensating for donor levels to produce semi-insulating InP is by using a known dopant, such as Fe. When Fe ions occupy In vacancy positions[5] and/or form complexes with P vacancies,[6] they produce electrically active deep acceptors, thus providing an effective trapping centre for any free n- carriers.

Apart from doping during wafer growth, ion implantation can be used to introduce Fe atoms into the matrix. A preliminary study into the dose dependence of the electrical characteristics of InP implanted with Fe is shown in Figure 5.1. A competition between the shallow donors and trapping centres leads to the observed changes in N_s, μ_{eff} and R_s. The effective mobility initially decreases with dose as the amount of damage is increased, but is quite large for the highest dose of 10^{16} cm^{-2}. The sheet carrier concentration follows essentially the opposite trend: increasing with dose, presumably due to the production of donor levels, and decreasing beyond 10^{15} cm^{-2}. The large amount of damage created at the highest dose may be causing the decrease in sheet carrier concentration due to the large number of trapping centres. The increase in mobility at a dose of 10^{16} cm^{-2} is unusual, although the mechanism responsible for this is not easily identified, since it is likely that multiple conduction paths are present in the sample, as illustrated in Chapter 3. R_s initially increases and is largest for a dose of 10^{14} cm^{-2} at approximately 1.1×10^6 $\Omega/\square$. Implantation reduces the initially semi-insulating value of the sheet resistivity from $\sim 10^8$ to 10^5-10^6 $\Omega/\square$, due to the shallow donor formation. For the two higher doses, the Fe ion implantation produces values of R_s which are similar to those for P, As, Ga and In ion implantation already discussed in Chapter 3. Figure 5.1 can be compared to Figure 3.7, where the larger values of R_s are obtained for the lower doses; in this regime there is not sufficient damage for creating large concentrations of donor-like defects.

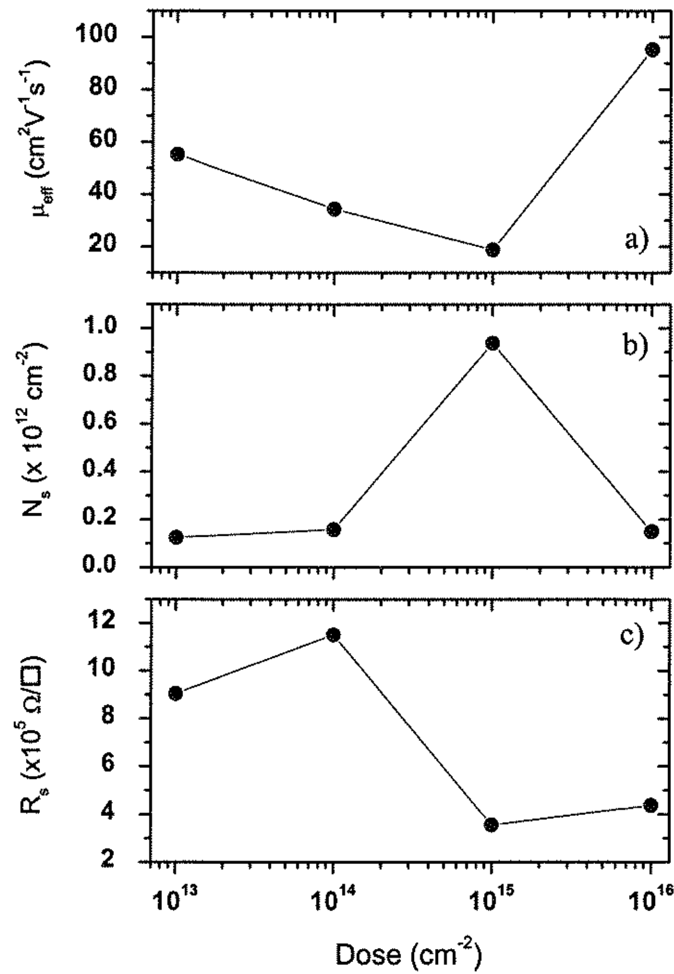

Figure 5.1 Effective mobility, μ_{eff}, sheet carrier concentration, N_s and sheet resistance R_s as a function of dose for 2 MeV Fe ion implantation into SI InP at 200°C, as determined by Hall effect measurements.

Because these measurements were done prior to annealing, it is assumed in all cases that Fe activation has not occurred and that the electrical characteristics are due to native defects caused by disorder within the lattice itself. The maximum values of R_s reported here are in good agreement with previous work into isolation of InP by ion irradiation[7].

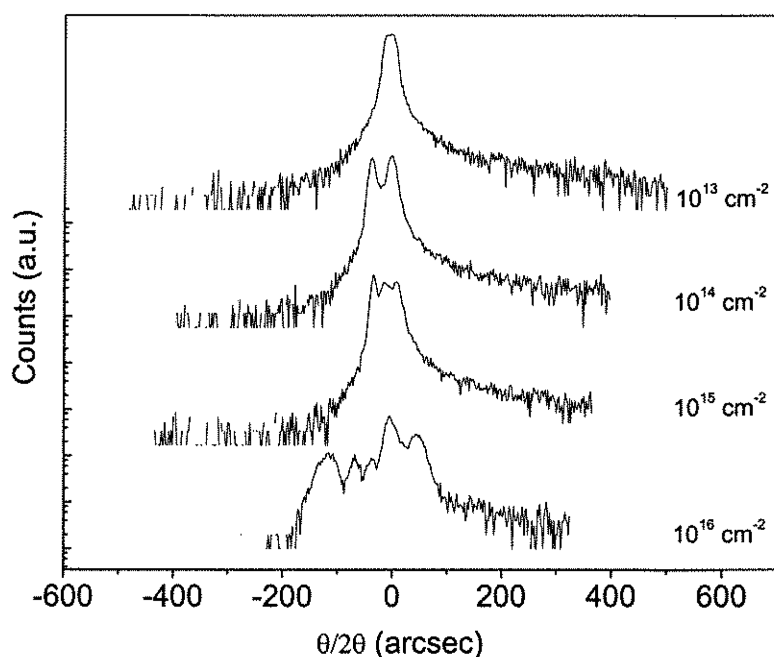

Figure 5.2 X-ray rocking curves as a function of dose for 2 MeV Fe ion implantation.

For this same dose range, we can look at the structural effects of the damage using DCXRD and XTEM. Figure 5.2 shows the relevant X-ray rocking curves. When compared with Figure 3.1, the evolution of the strain profile for Fe ion implants into InP appears to be quite similar to the case for implanting with P or In ions. XTEM scans in Figure 5.3 provide a different picture, however, and at the highest dose implantation results in an amorphised layer which is approximately 210 nm thick. Hence, the amorphisation threshold is lower for Fe ion implantation than for implantation with P, As, Ga or In ions. Once again a simple correlation between atomic mass and amount of damage or amorphisation threshold cannot be made, since Fe in fact has a lower atomic mass than In, although the latter element produced no amorphisation for implants at a dose of 10^{16} cm^{-2}. In a related finding, Gasparotto *et al.*

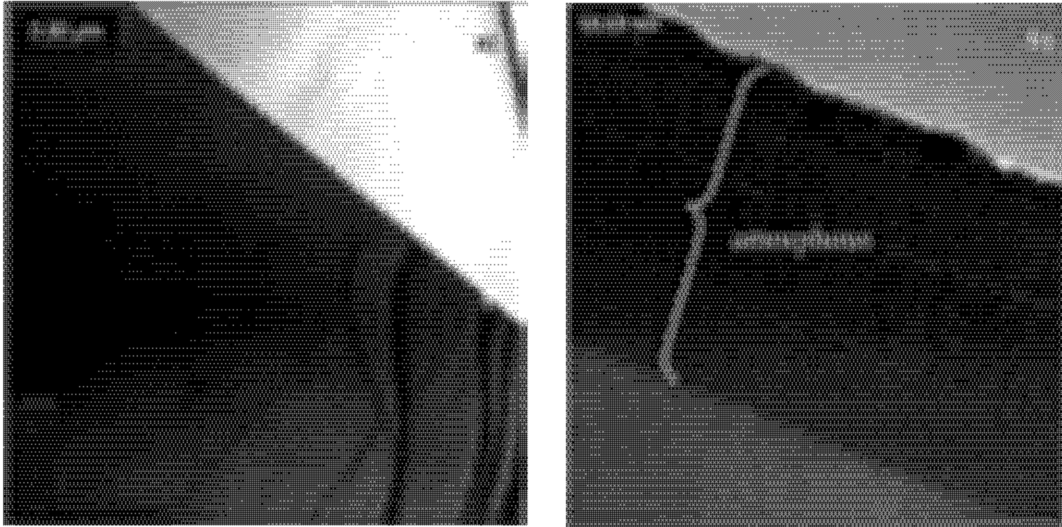

Figure 5.3 XTEM of Fe implanted InP to doses of (a) 10^{14} and (b) 10^{16} cm^{-2} at 200°C. Arrow indicates surface.

reported that low Fe solubility in InP and a high Fe reactivity with the implantation induced defects resulted in strong Fe redistribution and precipitation effects.

Given that the highest value of R_s is obtained for a dose of 10^{14} cm^{-2}, and that the structural damage was found to be extreme for the higher doses, annealing studies were pursued only on samples implanted to this particular dose.

Fig. 5.4 shows the corresponding Hall effect results for annealing of 10^{14} cm^{-2} Fe ion implanted InP at temperatures up to 900°C. Without annealing, the sample is n-type, and R_s has been reduced from the original semi insulating value of $\sim 3 \times 10^8$ Ω/□ to $\sim 10^6$ Ω/□. Increasing the annealing temperature causes R_s to decrease further, until at 600 - 700°C the conductivity changes to p-type. The sheet carrier concentration, N_s, at low annealing temperatures is similar to that produced by P ion implantation with P and In, As and Ga ions. For annealing at 600 and 700°C, N_s reaches a maximum of 1.2×10^{12} cm^{-2}.

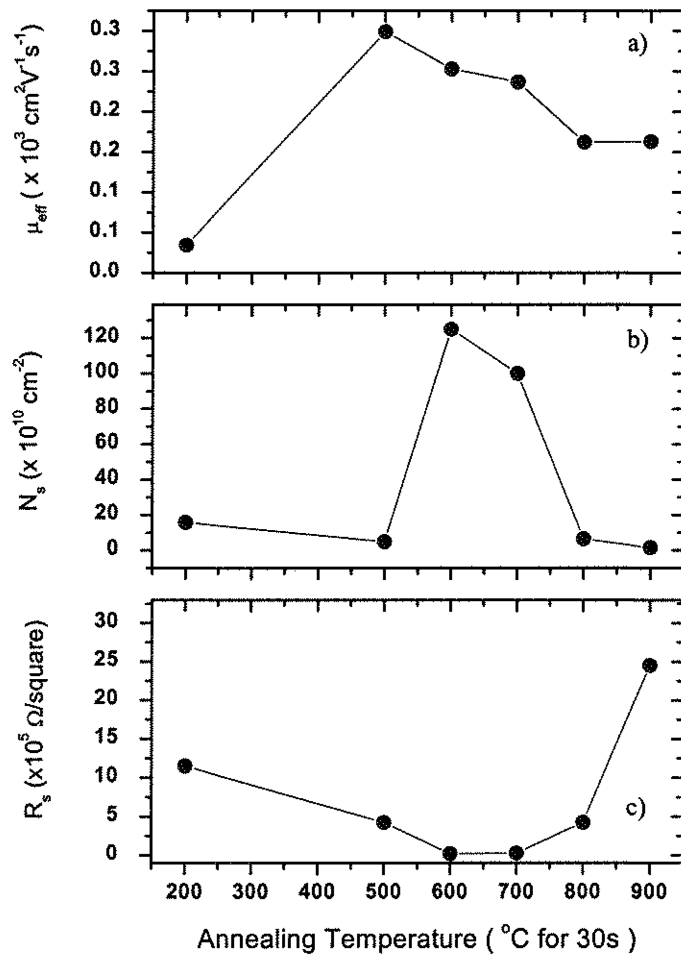

Figure 5.4 Dependence of effective mobility (a), sheet carrier concentration (b) and sheet resistance (c) on annealing temperature for SI InP samples implanted with 2 MeV Fe ions at a dose of 10^{14} cm^{-2}.

As for all single-energy implants, the Fe distribution profile in these samples is nonuniform,[8] and it is more than likely that several layers with different conductivity are present. The samples probably have a layer of n-type conduction near the surface, but, at appropriate annealing temperatures, are fully compensated or p-type in the region where the peak concentration of implanted Fe lies. Hence the Hall effect measurements will reflect a

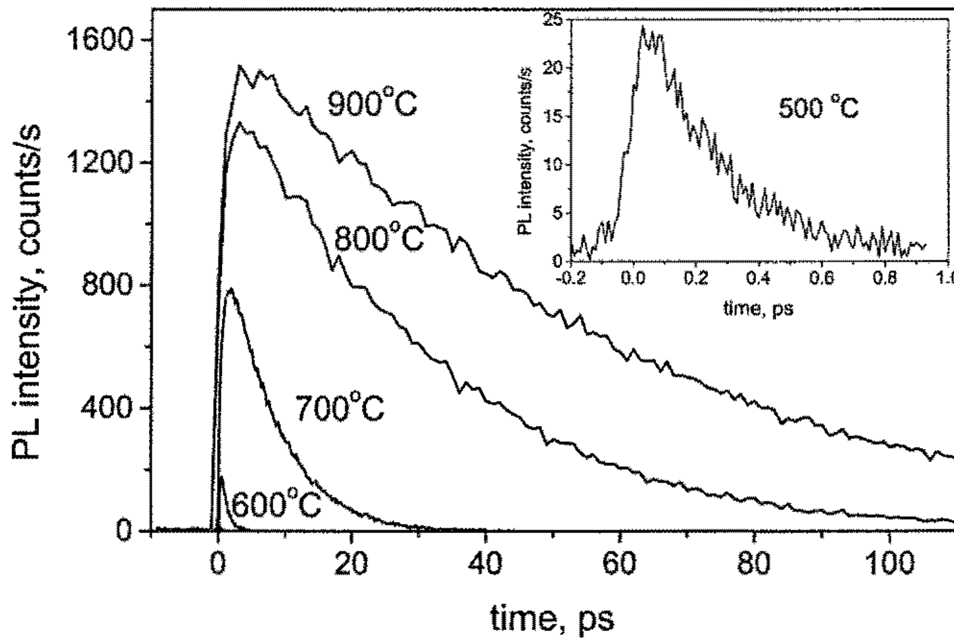

Figure 5.5 Photoluminescence transients for Fe-implanted InP (dose: 10^{14} cm^{-2}) annealed at different temperatures.

combination of the properties of these layers, or else the properties of a particular layer that constitutes the path of least resistance.

The results of time resolved photoluminescence on 2 MeV Fe ion implanted InP samples to a dose of 10^{14} cm^{-2} as a function of annealing temperature are shown in Figure 5.5. Time-resolved PL measurements provide information on the rate of carrier trapping into deep centers and, under certain experimental conditions, of carrier recombination. In combination with the electrical properties just mentioned, these measurements have allowed some insight into the origin of the active traps.

On the time scale of interest, the temporal changes in electron and hole concentrations occur mainly due to carrier trapping, because radiative recombination is a much slower process and occurs in nanoseconds. Figure 5.5 shows that the decay times vary with annealing temperature. Since the concentration of Fe in all the samples is the same, the PL dynamics

must therefore be determined by photoexcited carrier trapping to residual defects left after annealing rather than Fe-related defects (possibly Fe^{3+}/Fe^{2+} centers), which, otherwise, are efficient carrier recombination centers with similar electron and hole trapping rates.[9] The PL decay times, extracted from the exponential fits to the PL transients, are in the range from 130 fs to 46 ps for the samples annealed at 500 to 900°C. For the 500°C sample, the decay time was obtained after initial deconvolution of the PL transient with the pulse cross-correlation trace. No signal could be obtained for the unannealed sample for which the decay time is probably even shorter.

For all the Fe ion implanted samples, the PL decay times are basically independent of the photoexcitation power. The excitation power dependence often allows us to distinguish between trapping and recombination centers: at carrier densities higher or similar to trap densities, saturation of traps occurs, increasing the PL decay times. For the recombination centers, no such saturation is expected. For the 500°C sample, judging from the ultrashort trapping time, the trap concentration may be too large to reach saturation even for the highest photoexcited carrier densities. For the other samples, the independence of the decay times on excitation power suggests that the defects, where carrier trapping occurs, are efficient recombination centers.

The defects responsible for the electrical and optical behaviour of the samples discussed in this Chapter will have two sources: the native defects already discussed in detail in Chapter 3, and defects associated with Fe incorporation into the InP lattice. For these Fe ion implanted samples, the conductivity type changes from *n* to *p*, and the sheet resistance, lowest for the intermediate annealing temperatures, increases sharply for annealing temperatures above 800°C. These results can be explained by a competition between shallow P_{In}-related

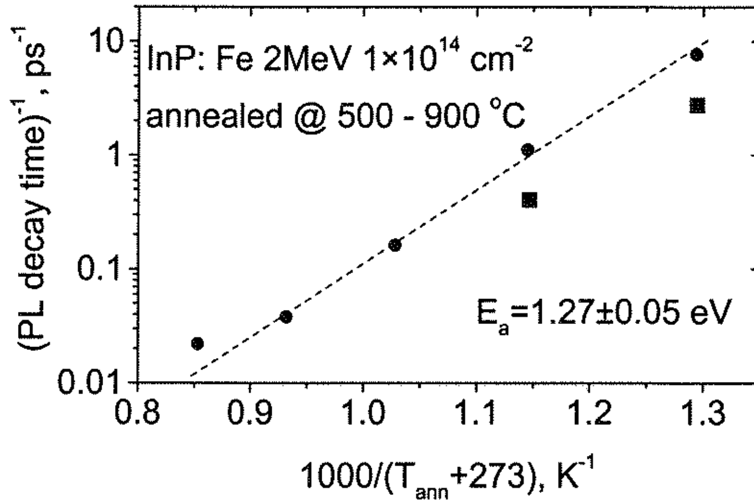

Figure 5.9 Arrhenius plot of the inverse PL decay time for Fe ion -implanted and annealed InP layers (circles). The squares show the data for the P-implanted samples suggesting a similar slope to that of InP:Fe.

donors and deep Fe-related acceptors. For the annealing at 600°C and 700°C, the shallow donors are already activated, but the Fe-related acceptors are not yet created at concentrations large enough to compensate the shallow donors. An increase in the annealing temperature causes Fe ions to diffuse and occupy In vacancy positions[5] and/or form complexes with P vacancies,[6] producing electrically active deep acceptors. Consequently, the resistivity increases, and the equilibrium carrier concentration becomes very small as the annealing temperature is increased. The mobility in the as-implanted case is low, as expected for a material with a high concentration of defects. Upon annealing at 500°C, μ_{eff} increases to ~ 300 $cm^2V^{-1}s^{-1}$ as the concentration of defects is reduced. The mobility then decreases with increasing annealing temperature as the degree of compensation of the material is increased.

Whilst the change in electrical properties with implantation dose and annealing temperature demonstrates an interplay between the implantation-induced shallow donors and compensating acceptors, the PL dynamics is determined by deep carrier traps and recombination centers. Some insight into the origin of these defects can be obtained when plotting the PL decay rates as a function of the inverse annealing temperature in an Arrhenius-type plot for the Fe-implanted samples (Fig. 5.6). As can be seen, all the points, except for the 900°C annealed sample, fall on a straight line producing an activation energy of 1.27±0.05 eV. This energy can be interpreted as energy needed to remove carrier traps by thermal annealing. The concentration of traps is proportional to the inverse PL decay time; with annealing temperature increased from 500 to 800°C the trap concentration decreases over two orders of magnitude.

The obtained activation energy can be compared to 1.2 eV determined from the RBS[10] and theoretical calculations[11] for P vacancy migration and annihilation. Since phosphorus vacancies and their complexes,[12-16] forming the deep traps, are produced during implantation in abundance, they are plausible candidates for recombination centers determining the photoexcited carrier dynamics. These centers should be important for all Fe ion implanted InP samples, except for the one annealed at 900°C, for which a deviation from the Arrhenius dependence suggests a different origin of the main carrier traps. This origin is probably Fe-related. Indeed, for 2×14 cm^{-2} Fe dose implanted at 200°C, the iron concentration within the first micrometer from the surface is expected to be non-uniform based on TRIM simulations. The concentration of Fe is estimated to be in the range of 10^{17} - 10^{18} cm^{-3}. This matches fairly well to the expected 3×10^{17} cm^{-3} density of Fe^{3+}/Fe^{2+} centers, which would be responsible for the PL decay time of 46 ps, if trapping only to such centers were considered.[9]

P vacancies and their complexes are produced during implantation independently of implantation species. Thus, vacancy-related recombination centers should be amongst the most important defects for carrier dynamics in any kind of implanted InP samples. To a certain degree, this is confirmed by similar trap activation energies for the Fe and P implanted samples (Fig. 5.6).

Summary

The expected chemical interaction of the Fe ions with the matrix have resulted in yet another form of damage (as compared to implants with P, As, Ga and In ions) which amorphises the material when implants are done to 10^{16} cm^{-2}. Correspondingly the sheet resistivities of samples implanted to the higher doses are in the low 10^5 Ω/□ range, due to shallow donors; for a dose of 10^{14} cm^{-2}, R_s reaches 10^6 Ω/□, where the damage is not so great. Fe ion implants into SI InP did result in subpicosecond lifetimes, the shortest time being measured for annealing at 500°C, however activation of Fe complexes, responsible for formation of deep traps which provide effective compensation for shallow donors and increase R_s to the 10^5 – 10^6 Ω/□ range, only occurs for annealing at temperatures above 700°C. Accordingly, it was found that the recombination centres responsible for the decay times at all annealing temperatures excepting 900°C were not Fe related.

5.4 MeV P implants into *p* - InP

An alternate method of compensation for the implantation induced donor levels is to implant into *p* -type InP. In this case the maximum sheet resistance will be obtained when the

concentration of n -carriers created by the implantation is exactly equal to the p -carriers incorporated into the wafer, taking into account the trapping effects of deep levels also caused by the implantation.

Figure 5.7 shows the Hall effect measurements for 1 MeV P implantation at 200°C into two different p -InP wafers of differing carrier concentrations at doses between 10^{12} and 10^{16} cm^{-2}, and subsequently annealed at 600°C. Within this range, a critical dose exists at which implantation compensates the p -type material. For an initial acceptor concentration of $\sim 3.4 \times 10^{17}$ cm^{-3}, an implant dose between 10^{13} and 10^{14} cm^{-2} was required. For an acceptor concentration of $\sim 1.3 \times 10^{18}$ cm^{-3}, an implant dose between 10^{14} and 10^{15} cm^{-2} was required.

To pinpoint more accurately the transition dose, a further study was done for implants at doses between 10^{14} and 10^{15} cm^{-2} into the wafer that had a carrier concentration $p \sim 1.3 \times 10^{18}$ cm^{-3}. Figure 5.8 shows the corresponding Hall effect results for annealing at both 500 and 600°C. Generally, the sheet resistance R_s is smaller for annealing at 600 than at 500°C. For annealing at 600°C, R_s peaks at a dose of 5×10^{14} cm^{-2}; this is where the maximum compensation is assumed to occur. Above the compensation dose, R_s sharply decreases, presumably due to an increased concentration of shallow donors, which at this point dominate conduction of the material. Both the mobility and the carrier concentration increase above the compensation dose. At the lower annealing temperature of 500°C, R_s remains fairly independent of dose, with a value of $\sim 10^6$ $\Omega/\square$. The relative insensitivity of R_s to the dose within this range may be due to the fact that 500°C is too low an annealing temperature to activate a sufficient quantity of donors necessary to significantly affect the conductivity.

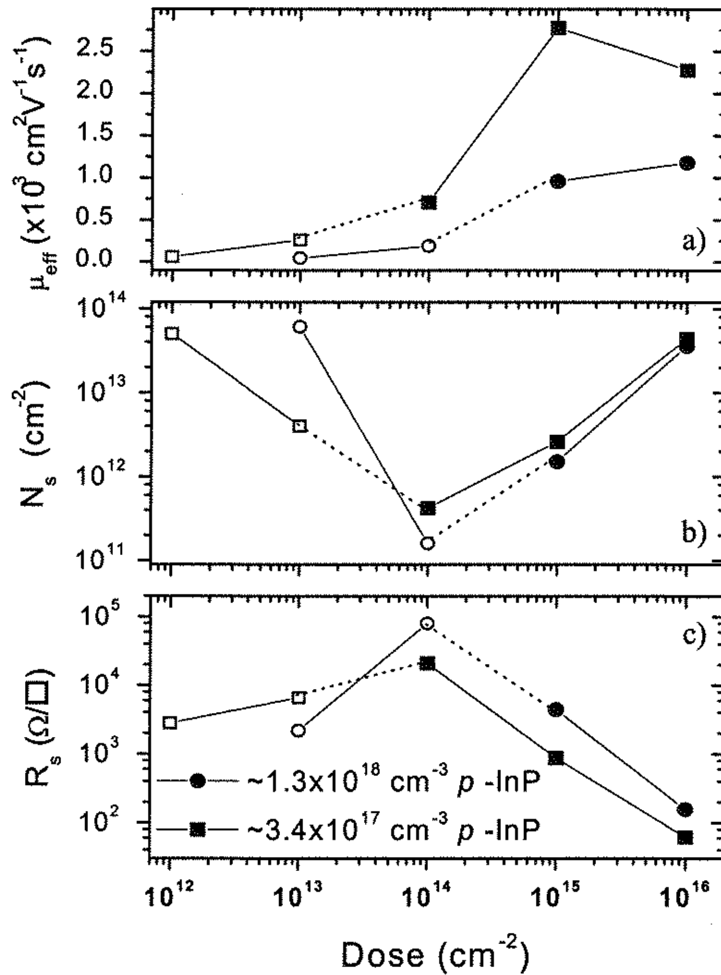

Figure 5.7 Mobility (a), sheet carrier concentration (b) and sheet resistance (c) as a function of P ion implant dose, for *p* -type InP with hole concentrations ~3.4 x 10^{17} and ~1.3 x 10^{18} cm^{-3}. Samples annealed at 600°C for 30s. Open symbols signify *p* -type, and closed symbols signify *n* -type. Joining lines are guides for the eye only.

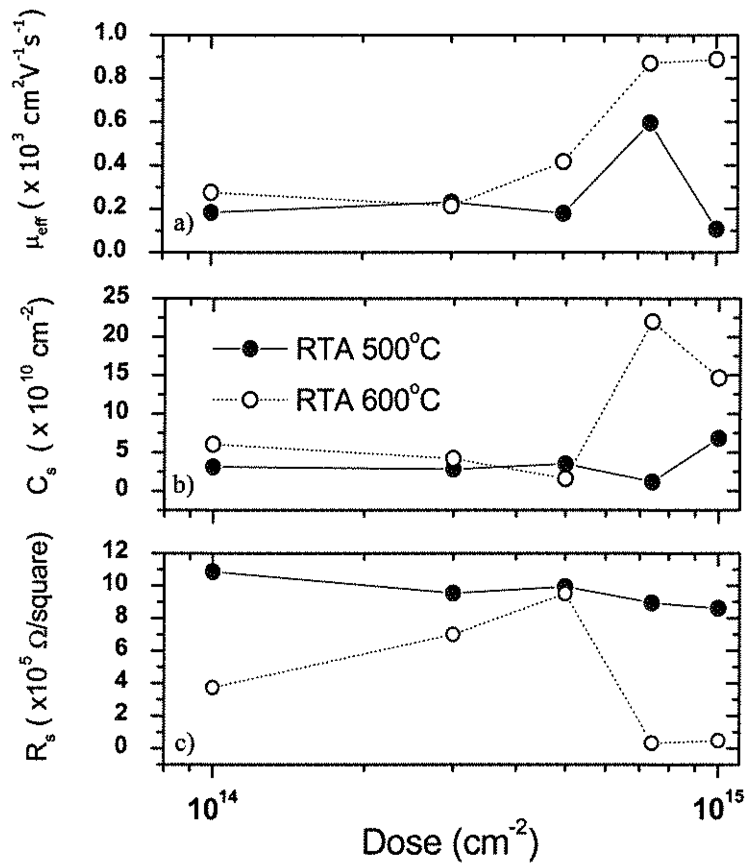

Figure 5.8 Effective mobility (a), sheet carrier concentration (b) and sheet resistance (c) as a function of implantation dose for *p* -type InP implanted with 1 MeV P ions and annealed at 500 and 600°C, respectively.

Recombination properties of implanted InP can also be explored on these *p* -doped P ion implanted samples. The PL decay times obtained by a single-exponential fit for the samples annealed at 500 and 600°C for high excitation powers (with respect to the concentration of equilibrium holes) are shown in Fig. 5.9. The PL decay times are much shorter for the samples annealed at 500°C. The same figure also shows PL decay times obtained for the sample annealed at 600°C for low excitation conditions. In the *p* -doped implanted sample, the

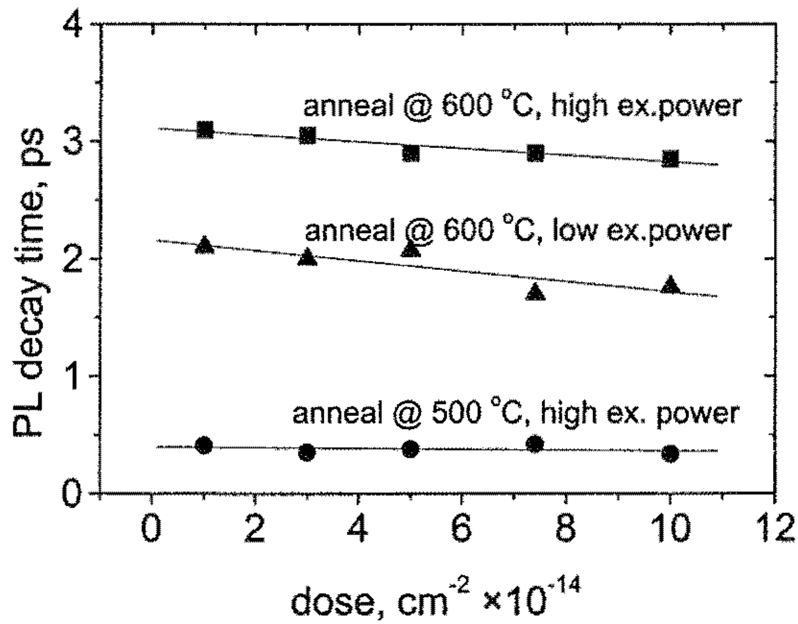

Figure 5.9 PL decay times for P-implanted InP samples annealed at 500 and 600°C as a function of implantation dose.

equilibrium holes are trapped to the implantation-induced defects, making them active electron traps. Thus, for low photoexcited carrier densities the PL intensity, which is proportional to the concentration of free electrons and holes, decays with the electron trapping time. For the high excitation power the PL decay time is longer. Assuming that in this case the electron traps are filled, the free electron and hole populations decay at the same rate, i.e. a new electron is trapped as soon as an electron trap is made active by trapping a hole. Then the PL decays with half the hole trapping time. The evaluated hole trapping times are around 6 ps and do not differ much from the electron trapping times, indicating that carrier dynamics in phosphorus ion-implanted InP is governed by recombination centers as well. This is advantageous for applications where device operation at high repetition frequencies is required.

Another interesting observation, which can be made from Fig. 5.9, is a relatively small dependence of the PL decay time (and the concentration of active traps) on the implantation dose. For the 600°C annealing, the trapping times decrease by only about 25% when the ion dose is changed from 10^{14} to 10^{15} cm^{-2}, i.e. by an order of magnitude. The same tendency holds for the samples annealed at 500°C. Such behaviour may be understood by taking into account peculiarities of heavy ion implantation at elevated temperatures. Rutherford backscattering (RBS) data for Si-implanted InP samples in the literature have shown a broad plateau in the damage dependence on the implanted ion density for doses extending over several orders of magnitude, pointing to an equilibrium between defect production, recombination and dynamic annealing.[17] Similar data have been obtained for Fe ion implantation at 200°C.[8]

Summary

By implanting with MeV P ions into p -InP, it was possible to compensate the initial hole carriers with implant-induced shallow donors. The dose at which conversion of p - to n - type occurs corresponds to a maximum in sheet resistivity as measured by Hall effect, and was greater for increased initial free carrier concentration. For the samples with $p \sim 1.3 \times 10^{18}$ cm^{-3}, a relative insensitivity of electrical and optical characteristics to dose was achieved by annealing at 500°C. Additionally, these conditions provided subpicosecond lifetimes and the highest sheet resistivities, thus making them ideal for fabricating InP which could be used in the fabrication of ultrafast photodetectors.

5.5 Conclusion

Both methods - implantation of p -InP with P and SI InP with Fe ions - can be used to produce a material with subpicosecond response times, good mobility and high resistivity. From the point of view of the shortest decay times, this is achieved in both cases for the lowest annealing temperature of 500°C. At this temperature, the PL decay time resulting from Fe ion implantation into SI InP (130 fs) is shorter than that achieved with P ion implantation into p -InP (400 fs) and is due to the greater amount of damage caused by Fe ion implantation compared to P ion implantation. However, for device considerations, such a difference is not too important as 400 fs is a time short enough for most applications in ultrafast optoelectronics. P ion implantation into p -InP yields a material with a higher sheet resistance ($\sim 10^6\ \Omega/\square$) at 500°C annealing, and both the sheet resistance and the decay time are weakly dependent on the implantation dose. This is highly desirable from a manufacturing point of view, where repeatability of results is of the utmost importance. P ion implantation of p -InP in this dose regime assures that good quality material for devices could be obtained with a relative insensitivity to implant dose. In the Fe ion implantation case, the annealing temperatures needed to produce highly resistive material result in decay times of the order of tens of picoseconds, disqualifying these materials for applications when both high resistivity and subpicosecond lifetimes are needed. Additionally, it appears that the dose dependence of the electrical characteristics of Fe-implanted InP is stronger.

References

1. F. W. Smith, A. R. Calawa, C.-L. Chen, M. J. Manfra and L. J. Mahoney, IEEE Electron Device Lett. **9**, 77 (1988).
2. F. W. Smith, H. Q. Le, V. Diadiuk, M. A. Hollis, A. R. Calawa, S. Gupta, M. Frankel, D. R. Dykaar, G. A. Mourou, and T. Y. Hsiang, Appl. Phys. Lett. **54**, 890 (1989).
3. S. Gupta, J. F. Whitaker, and G. A. Mourou, IEEE J. Quantum Electron. **28**, 2464 (1992).
4. M.-J. Tsai and R. H. Bube, J. Appl. Phys. **49**, 3397 (1978)
5. A. Gasparotto, A. Carnera, C. Frigeri, F. Priolo, B. Fraboni, A. Camporese, and G. Rosetto, J. Appl. Phys. **85**, 753 (1999).
6. A. Kadoun, G. Marrakchi, A. Kalboussi, D. Barbier, and G. Guillot, Mat. Sci. Eng. **B33**, 188 (1995).
7. H. Boudinov, H. H. Tan and C. Jagadish, J. Appl. Phys. **89**, 5343 (2001).
8. A. Gasparotto, A. Carnera, C. Frigeri, F. Priolo, B. Fraboni, A. Camporese, and G. Rosetto, J. Appl. Phys. **85**, 753 (1999).
9. D. Söderström, S. Marcinkevičius, S. Karlsson, and S. Lourdudoss, Appl. Phys. Lett. **70**, 3374 (1997).
10. U. G. Akano, I. V. Mitchel, and F. R. Shepherd, Appl. Phys. Lett. **59**, 2570 (1991).
11. J. A. Van Vechten and J. F. Wager, Phys. Rev. B **32**, 5259 (1985).
12. M.Alatalo, R.M.Nieminen, M. J.Puska, A. P.Seitsonen, and R. Virkkunen, Phys. Rev. B **47**, 6381(1993).
13. K. Kuriyama, K. Tomizawa, M. Kashiwakura, and K. Yokoyama, J. Appl. Phys. **76**, 3552 (1994).

14. A. Sibille, Appl. Phys. Lett. **48**, 593 (1986).

15. T. Bretagnon, G. Bastide, and M. Rouzeyre, Phys. Rev. B. **41**, 1028 (1990).

16. S. K. Si, S. J. Kim, Y. Moon, and E. Yoon, J. Appl. Phys. **83**, 2366 (1998).

17. E. Wendler, T. Opfermann, and P. I. Gaiduk, J. Appl. Phys. **82**, 5965 (1997).

CHAPTER 6

Ion Implanted InGaAs for Ultrafast Photodetector Applications

6.1 Introduction

Ultrafast photonics technology using InGaAs is in particular demand, due to the ideal long wavelength capacity of this semiconductor; devices operating at the 1.3 and 1.55 μm wavelengths are required in optical fibre communications for the internet, where demand for increased data transmission is skyrocketing, and long wavelength capabilities in terahertz spectroscopy are also needed. Since InGaAs epilayers are often grown lattice matched to InP substrates, adding the previous studies into ion implanted InP and InGaAs discussed in Chapters 3, 4 and 5 to the work presented in this Chapter provides a good understanding of the entire InGaAs/InP system. Combining knowledge of the electrical and optical properties of implanted and annealed InP and InGaAs provides an excellent basis for predicting the properties of implanted InGaAs/InP multilayer systems.

Methods of maximising resistivities in InGaAs have been explored in Chapter 4, however, the optical properties of such material have not yet been discussed. Others have found that defective InGaAs grown at low temperatures results in a lower concentration of arsenic antisites than in LT GaAs, and as a consequence subpicosecond electron lifetimes were not obtained.[1,2] An electron lifetime of 400 fs was only observed in conductive LT InGaAs heavily p - doped with Be, in which the lifetime was determined by Auger recombination.[3] On the other hand, defective InGaAs layers and quantum wells produced using ion- and proton implantation have shown carrier lifetimes as short as 1-2 picoseconds,[4,5] although there was no corresponding investigation into the resistivity of these layers. Conversely, resistivities of $\sim 10^5$ Ω/□ were measured in ion-implanted InGaAs,[6] but in these layers the carrier lifetimes have not been measured. The results presented here, then, are of investigations into methods of

achieving high resistivity InGaAs layers with corresponding subpicosecond lifetimes through ion implantation.

6.2 Experimental

Both undoped and p-type $In_{0.53}Ga_{0.47}As$ epilayers were used as starting material for the research presented in this Chapter, and were grown to a thickness of 1.5 μm on semi-insulating (100) InP substrates by MOCVD. TRIM simulations were used to predict the energy required to place the peak damage at 1 μm from the surface for Fe and P ion implants, which turned out to be 2 MeV and 1 MeV, respectively. Thus, samples cleaved from the undoped wafer were implanted with 2 MeV Fe ions at room temperature and at 200°C, at doses between 10^{13} and 10^{16} cm^{-2}. Annealing at temperatures between 500 and 900°C for 30 seconds was subsequently performed on those samples that were implanted at doses of 10^{15} and 10^{16} cm^{-2} at room temperature. During annealing, an InP proximity cap was used on the substrate and a GaAs proximity cap was used on the InGaAs epilayer. Samples cleaved from the p-type wafer were implanted with 1 MeV P ions at room temperature to doses between 10^{12} and 10^{17} cm^{-2}, and then annealed at 500°C and 600°C for 30 seconds. The p-material was doped with Zn, resulting in an initial free hole carrier concentration of $\sim 3 \times 10^{19}$ cm^{-3}. For all implants, the samples were tilted at 7° from the normal direction of the beam to minimise channeling effects.

Hall effect measurements were carried out using the van der Pauw geometry, with sintered indium metal ohmic contacts.

Carrier dynamics in the implanted InGaAs layers were studied by time-resolved photoluminescence (TRPL) and time resolved differential reflectivity (TRDR). TRPL measurements were performed using an upconversion set-up with excitation at 800 nm and PL detection at the band gap wavelength. Degenerate TR experiments were conducted with a central pump and probe wavelength of 1600 nm. A femtosecond Ti:sapphire laser and an optical parametric oscillator providing pulses of 80 - 150 fs duration were used in the TRPL and TRDR experiments, respectively. The photoexcited carrier density and temporal resolution in both experiments was $\sim 1\times10^{18}$ cm^{-3} and 150 fs, respectively. In the TRDR experiment, the probe intensity was 0.01 of the pump intensity.

6.3 MeV Fe ion implants into undoped InGaAs

In searching for the optimum characteristics of implanted InGaAs for ultrafast photodetector applications, and bearing in mind the shallow donor formation which readily occurs in this material, the techniques used in Chaper 5 were also applied here. Fe also occupies a cation site in InGaAs when activated, forming a deep acceptor[7], and thus it was hoped that implantation with Fe would result in a material with high resistivity as well as short response times. Because InGaAs does not show the same sensitivity to amorphisation as InP, implants were performed at both room temperature and 200°C.

Figure 6.1 shows the effective mobility, μ_{eff}, the sheet carrier concentration, N_s, and sheet resistance, R_s, for 2 MeV Fe ion implanted InGaAs epilayers as a function of dose. While implanting into the undoped InGaAs has resulted in much lower sheet resistivities than were measured for Fe implants into SI InP at the same doses (see Figure 5.1), a more pertinent

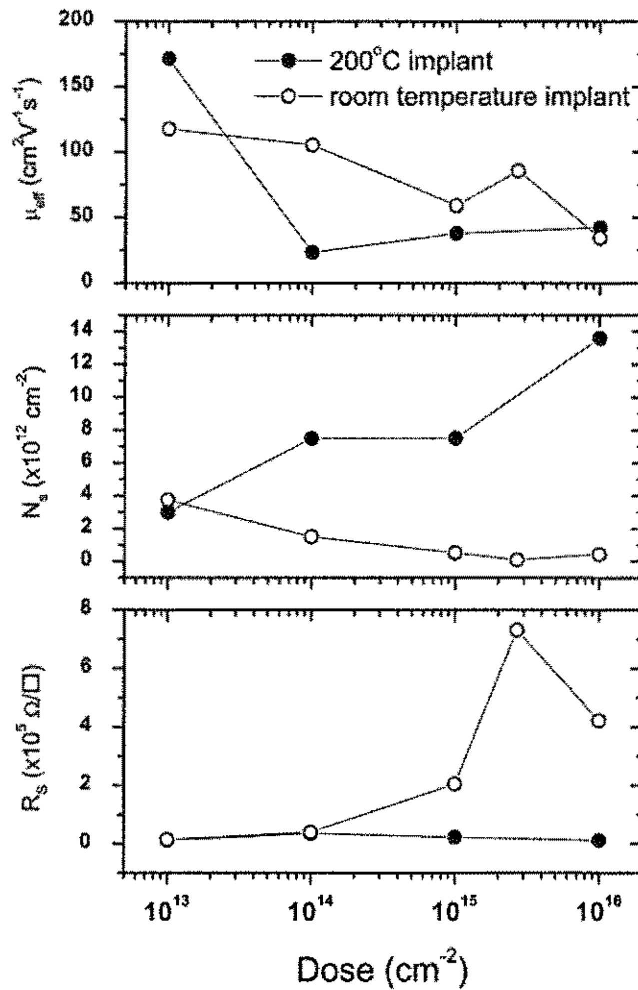

Figure 6.1 Effective mobility, μ_{eff}, sheet carrier concentration, N_s, and sheet resistance, R_s, for both room temperature and 200°C 2 MeV Fe ion implantation as a function of dose.

comparison is with the original values for the unimplanted material. Hall effect measurements on the undoped, unimplanted epilayers yielded an effective mobility of ~5 x 10^3 cm^{2}V^{-1}s^{-1}, an *n* - type sheet carrier concentration of 1-2 x 10^{12} cm^{-2} and sheet resistance of ~800 Ω/□. So we see that the implantation at both room temperature and 200°C has actually increased R_s from the 10^2 up to the 10^5 Ω/□ range and reduced the effective mobility from the thousands to the hundreds of cm^{2}V^{-1}s^{-1}. The effect of the implantation on the electrical characteristics can be

divided into three categories: the trapping of the inadvertent donors by deep defect levels, the formation of new shallow donors such as the As antisite, and the onset of hopping conduction. In Chapter 4 it was shown that, for room temperature O ion implants, the electrical characteristics were dominated by shallow donor production above a dose of $\sim 10^{12}$ cm^{-2}. Fe of course has a much larger atomic mass than O, therefore it would be expected that for the doses used here, a significant contribution would be coming from the shallow donors. Trapping of carriers must also be playing an important role, since the implanted samples have higher resistivites and lower mobilities than the untreated material.

For room temperature implantation, R_s reaches a maximum value of 7 x 10^5 $\Omega/\Box$ as the trapping of inadvertent donors increases with increasing dose. At the highest dose, R_s begins to decrease again, accompanied by a high value of N_s and low μ_{eff}, which is probably due to a shallow donor production which has become stronger than the trapping. The decreasing mobilities may also indicate the onset of hopping conduction. For 200°C implants, R_s stays relatively constant with increasing dose - a strong dynamic annealing at the elevated temperature is most probably preventing the large concentration of traps which occurred for room temperature implants from forming, and simultaneously favouring the creation of shallow donors. N_s is increased to the 10^{13} cm^{-2} range as the dose is increased for 200°C implants, but decreases to the 10^{11} cm^{-2} range for room temperature implants. For elevated temperature implantation, the effective mobility is 170 $cm^2V^{-1}s^{-1}$ for the lowest dose implant, where the damage to the lattice is relatively small, and drops sharply to a few tens of $cm^2V^{-1}s^{-1}$ as the dose is increased. For room temperature implantation we see that the mobilities are still quite low, and decrease with increasing dose (although less abruptly than for elevated temperature implantation), however the sheet carrier concentrations are greatly reduced (4 x 10^{12}- 1 x 10^{11} cm^{-2}), and at the higher doses R_s can reach up 7 x 10^5 $\Omega/\Box$.

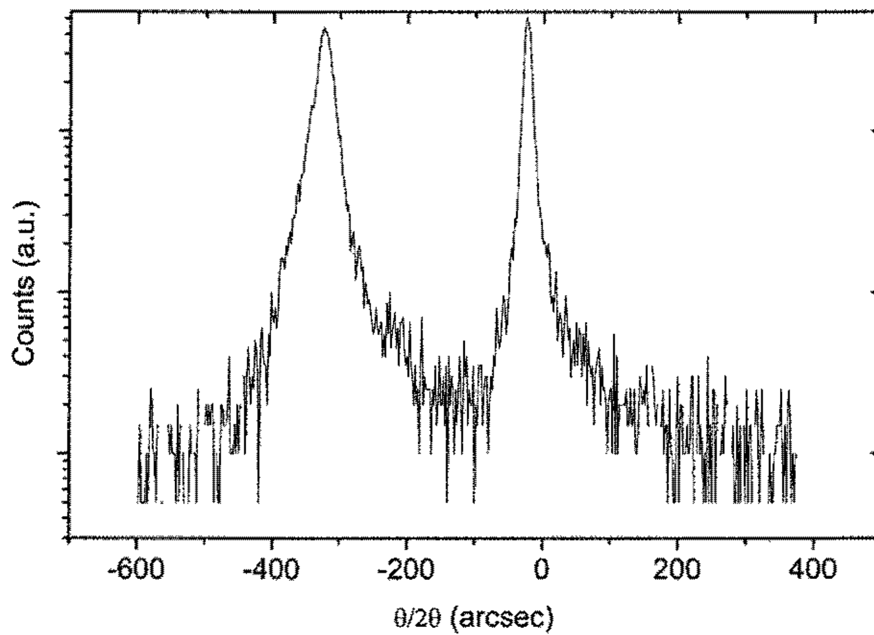

Figure 6.2 DCXRD of an unimplanted 1.5 μm InGaAs epilayer grown on a SI InP substrate.

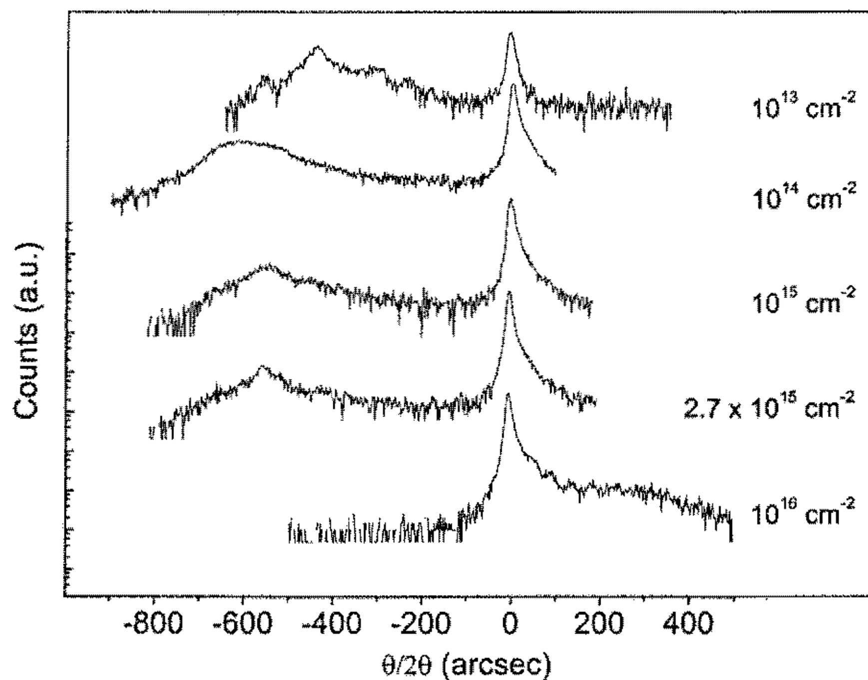

Figure 6.3 Evolution of X-ray rocking curves as a function of dose for room temperature implantation of InGaAs epilayers with 2 MeV Fe ions. Spectra vertically shifted for clarity.

The nonuniform damage profile of these implants will once again result in a possibility of multiple conductive paths occurring within the sample, making it difficult to arrive at conclusive explanations for the electrical behaviour. However, an analysis into the structural changes resulting from implanting at different temperatures and doses, and annealing at different temperatures can be very helpful. Figure 6.2 shows the DCXRD spectrum for an unimplanted sample. The narrower peak situated at 0 arcsec is generated from the InP substrate, while the slightly broader peak at -300 arcsec corresponds to the InGaAs. Such an angular separation for the two peaks corresponds to a lattice mismatch of approximately 0.11%.

Figure 6.3 shows the evolution of the DCXRD rocking curves as a function of dose for room temperature Fe ion implants into InGaAs epilayers on InP. Damage resulting from implantation causes a significant broadening of the InGaAs peak, which increases with implant dose. At the highest dose of 10^{16} cm^{-2}, the InGaAs peak appears to have been completely annihilated, and a broad feature appears for positive $\theta/2\theta$. A transition in the type of damage has occurred between the doses of 2.7 x 10^{15} cm^{-2} and 1 x 10^{16} cm^{-2}. For an implant dose of 10^{14} cm^{-2}, the InGaAs peak shifts towards more negative $\theta/2\theta$, which is indicative of an increase in compressive strain between the epilayer and the InP substrate; for higher doses this peak begins to move back towards -300 arcsec.

XTEM was also performed on these samples, and for all but the highest dose implants, no extended defects were observed in the images. The results for XTEM images on a sample which was implanted at 10^{16} cm^{-2} at room temperature are shown in Figure 6.4. An amorphous layer ~ 1330 nm thick was formed near the surface, followed by a 110 nm-thick crystalline layer. An additional amorphous layer was formed with a thickness of 300 nm directly below the InGaAs/InP interface. The amorphous/crystalline interfaces were very

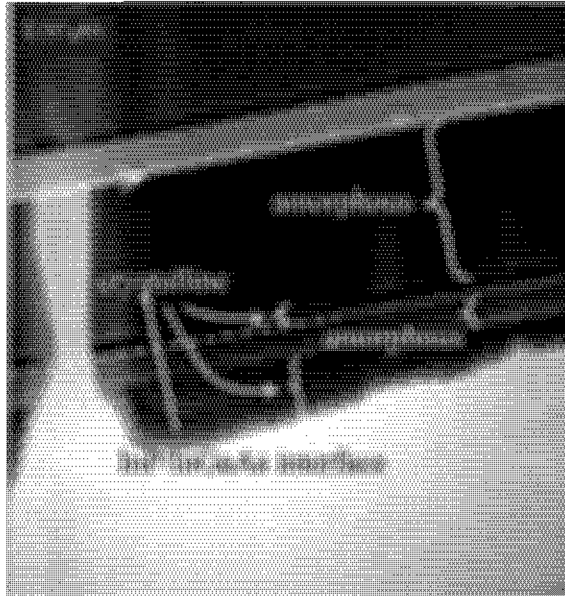

Figure 6.4 XTEM image for InGaAs epilayer on InP, implanted with 2 MeV Fe ions at room temperature to 10^{16} cm^{-2}. Arrow indicates surface.

rough and associated with many planar defects lying along the {111} planes. Below the amorphous/crystalline interface in the InP a high density of small dislocation loops was found. High resolution XTEM analysis found that these planar defects were not stacking faults. These results confirm that a threshold is reached by implanting to a dose of 2.7 x 10^{15} cm^{-2} in InGaAs at room temperature, above which multiple amorphous layers are formed. The crystalline material separating these amorphous layers is highly defective.

The effect of annealing on this sample is shown in the DCXRD spectra of Figure 6.5. Even for the highest annealing temperatures, the original lattice structure is not recovered. Figure 6.6 confirms this, with XTEM showing that annealing at 800°C did not cause the amorphous regions to recover their crystallinity, instead resulting in a high density of twins and planar defects in the to amorphous region of the InGaAs. After annealing, a large concentration of voids occur in the post-implant InGaAs that had remained crystalline, and in

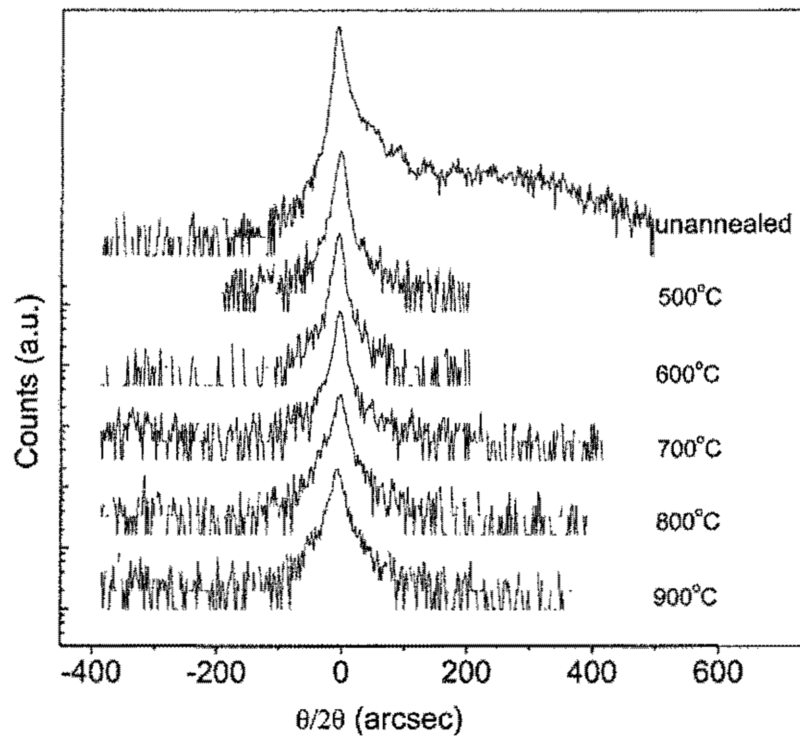

Figure 6.5 DCXRD spectra of InGaAs implanted to 10^{16} cm^{-2} at room temperature with 2 MeV Fe ions and annealed at temperatures between 500°C and 900°C for 30 seconds. Spectra vertically shifted for clarity.

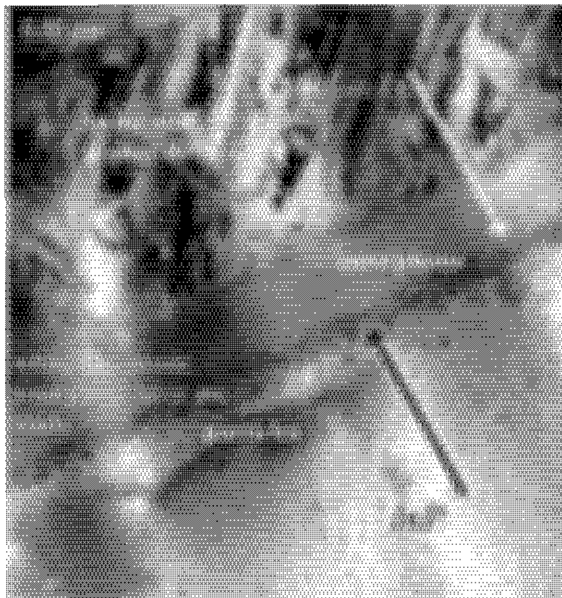

Figure 6.6. XTEM image for InGaAs epilayers on InP implanted with 2 MeV Fe ions at room temperature to 10^{16} cm^{-2}, after annealing at 800°C for 30 seconds, showing amorphous layers, voids and particles.

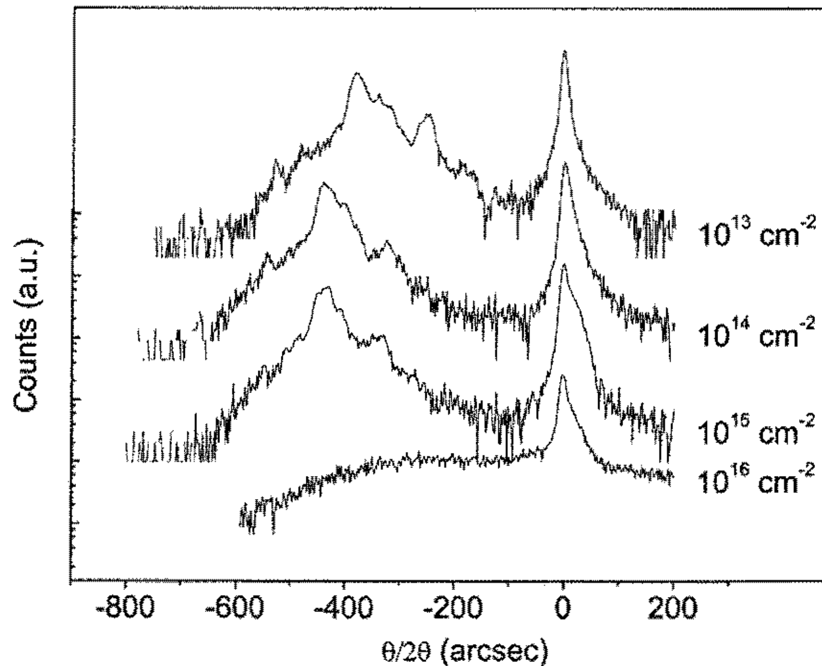

Figure 6.7 Evolution of DCXRD spectra as a function of dose for 200°C implantation into undoped InGaAs with 2 MeV Fe ions.

the InP layer that had been amorphised after implantation, there are many particles of an unknown nature. The presence of this amorphous layer in the 10^{16} cm^{-2} implanted sample makes hopping conduction possible in this region, due to the excessive number of defects. Such hopping conduction may be contributing to the decrease in sheet resistance and mobility observed in Figure 6.1, although it is not clear whether the main conduction path is through this layer.

The samples from Figure 6.1 that were implanted at 200°C were also studied using DCXRD and XTEM. Figure 6.7 shows the X-ray rocking curves for this elevated temperature implantation as a function of dose. Similarly to the room temperature implants, there is a transition in the type of damage created at doses between 10^{15} and 10^{16} cm^{-2}. At the highest dose, the peak originating from the InGaAs epilayer is barely intact. A shift to more negative

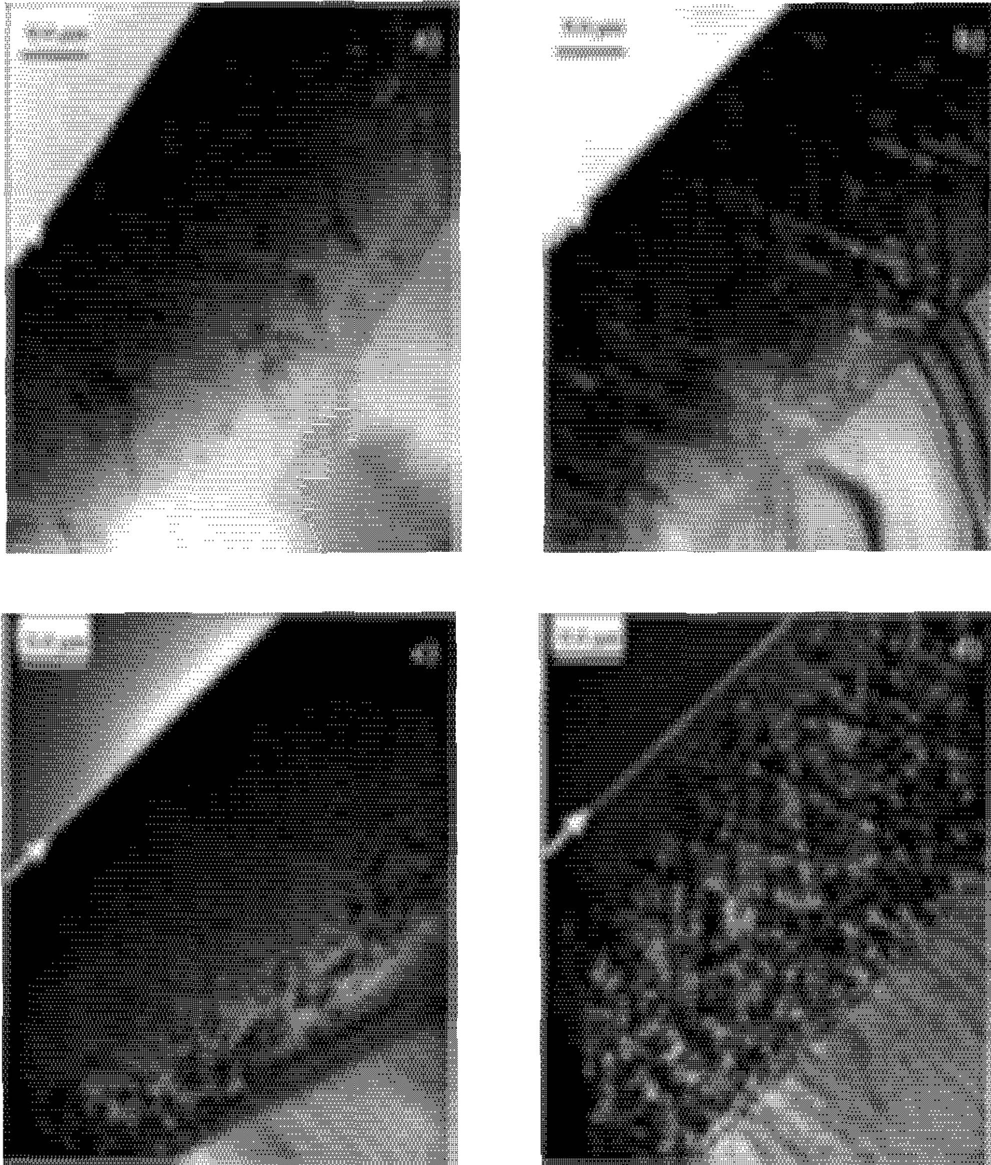

Figure 6.8 XTEM images for InGaAs epilayers on InP, (a) bright field and (b) dark field, implanted with 2 MeV Fe ions at 200°C to 10^{15} cm^{-2}, and (c) bright field and (d) dark field, to 10^{16} cm^{-2}. Arrow indicates surface.

$\theta/2\theta$ is observed for the InGaAs peak as the dose is increased.

For 200°C implants at 10^{15} and 10^{16} cm^{-2}, XTEM images are shown in Figure 6.8. Unlike the room temperature implants at 10^{15} cm^{-2}, which resulted in no visible damage in the XTEM, 200°C implants caused a high density of twins and planar defects near the surface. At the lower extreme of the damaged region in this sample, small dislocation loops and/or clusters were found. Interestingly, and again in contrast to the results for room temperature implantation, the destruction of the InGaAs peak observed in the DCXRD for 200°C implantation at 10^{16} cm^{-2} does not correspond to amorphisation of the layer. For this higher dose implant, a high density of stacking faults was found from 100 nm below the surface right down to the InGaAs/InP interface. Some small dislocation loops and/or clusters were found in the damaged region near the interface. The absence of a peak due to the InGaAs epilayer for 10^{16} cm^{-2} implantation shown in Fig. 6.7, while not due to amorphisation, is due to the extreme damage in the InGaAs epilayer.

The effect of annealing on the sample implanted to 10^{16} cm^{-2} is shown in the DCXRD spectra of Figure 6.9 and the XTEM images in Figure 6.10. By annealing at the highest temperatures, the crystal structure of the InGaAs epilayer is able to be recovered to some extent, as shown by the recovery of the InGaAs peak in the DCXRD. Figure 6.10 shows that a high density of dislocations and voids remain in the sample, extending from the top of the sample to the damaged interface, with many dislocation loops and clusters in the InP substrate near the interface.

The studies above illustrate that, compared to the structural investigations into implanted InP, the damage processes for implants into InGaAs are very different (contrast Figures 6.8 and 5.3, for instance) when implanting under identical conditions. As a further

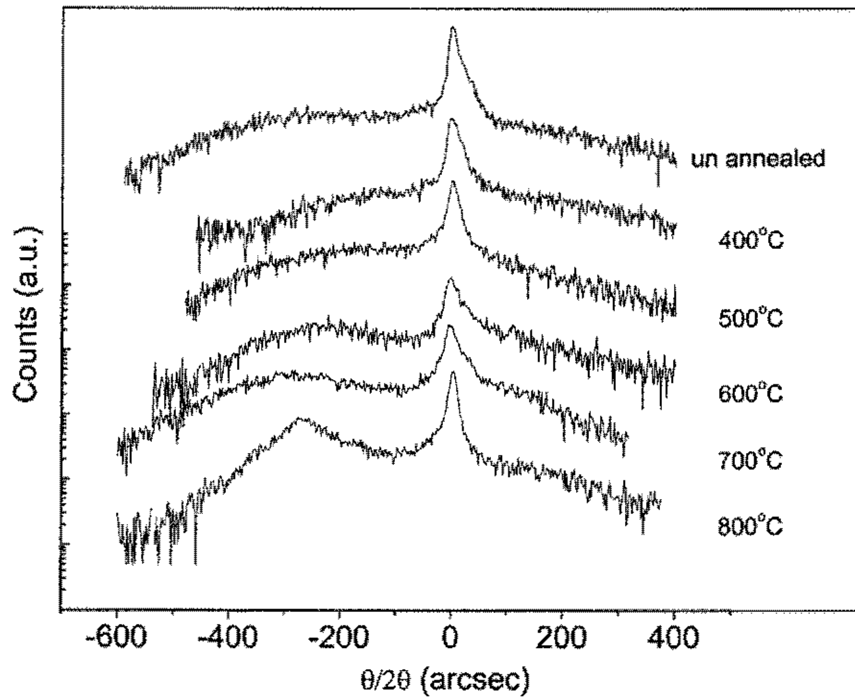

Figure 6.9 DCXRD spectra of InGaAs implanted to 10^{16} cm^{-2} at 200°C with 2 MeV Fe ions and annealed at temperatures between 500°C and 900°C for 30 seconds. Spectra vertically shifted for clarity.

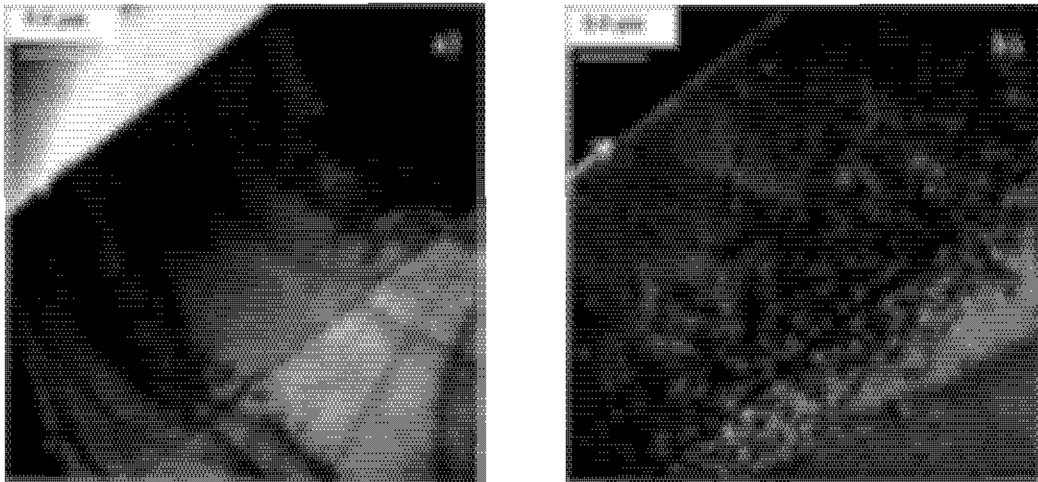

Figure 6.10 XTEM images for InGaAs epilayers on InP, implanted with 2 MeV Fe ions at 200°C to 10^{16} cm^{-2}, and annealed at 800°C for 30 seconds, (a) bright field and (b) dark field. Arrow indicates surface.

example, it is common knowledge that for room temperature implantation of InP, significant defect annihilation occurs over time[8], in which the damage caused by implantation is repaired.

To verify whether or not this had occurred for the room temperature Fe ion implants of the InGaAs, repeat DCXRD measurements were performed on the samples described above after 14 days, and no change was recorded. Thus, in addition to concluding that damaged InP and InGaAs behave differently, we can be confident that our measurements of implanted InGaAs were not dependent on the elapsed time after implantation. Indeed, Akano *et al*[9] noted that amorphous layers could be formed in InP up to 373 K for O fluences above a critical dose, whereas a strong dynamic annealing precluded any amorphisation of InGaAs at 290 K for O implants to doses up to 5×10^{15} cm^{-2}.

The studies above have shown us the degree to which the original structures, after implants at different doses and temperatures, can be recovered by annealing. The effect of annealing on the electrical and optical properties of the implanted samples must also be investigated, since as-implanted material will be too defective for any optical applications, regardless of the high values of R_s obtained. Annealing provides energy for Fe atoms to migrate to the cation sites, thereby forming deep traps, as well as allowing shallow donor formation to play a more significant role. The interplay between these two effects is illustrated in Figure 6.11, which shows the evolution of Hall effect measurements for samples implanted to 10^{15} and 10^{16} cm^{-2} at room temperature, as a function of annealing temperature.

The defects affecting the electrical and optical properties of these implanted samples will have two sources: complexes resulting from Fe incorporation and defects caused by disorder within the lattice itself. The low resistivity of ion implanted and LT-InGaAs is attributed to the existence of donor levels with the activation energy of 30 – 40 meV.[10] In addition to these native defects, incorporation of Fe atoms into cation sites in InGaAs results

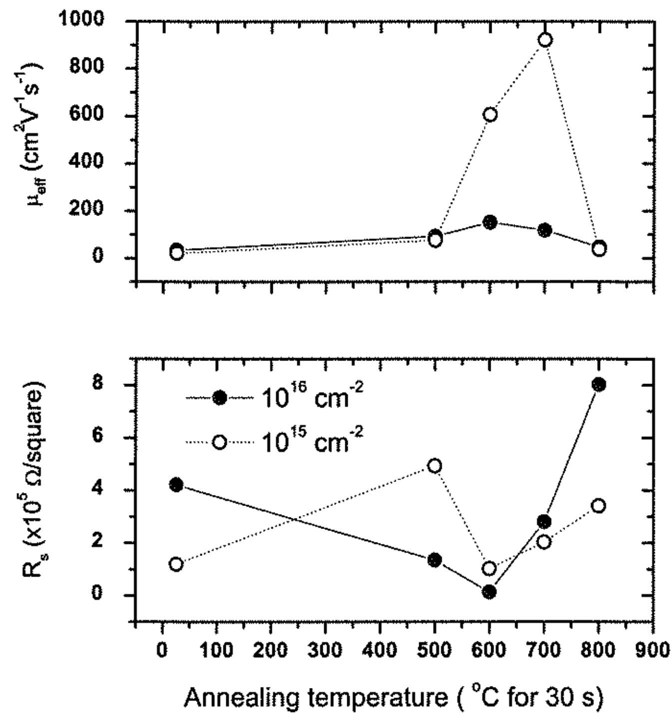

Figure 6.11 Effective mobility, μ_{eff}, and sheet resistance R_s for room temperature 2 MeV Fe ion implantation as a function of annealing temperature for 10^{15} and 10^{16} cm^{-2}.

in a deep acceptor with an energy of ~0.35 eV which shifts the Fermi level towards the mid-gap and increases the resistivity.[12] Other studies have found that annealing InGaAs containing Fe atoms at high temperatures (e.g. 800 °C) for a relatively short time (e.g. 5 s) results in a large surface buildup of Fe, which increases with annealing time and temperature.[13] Therefore, in InGaAs samples prepared under such conditions as are presented here, it is once again likely that layers with different optical and electrical properties exist, according to their distribution of different types of defects.

The 10^{15} cm^{-2} implanted sample has low mobilities for annealing temperatures below 500°C, which then increase sharply to almost 10^3 cm^{2}V^{-1}s^{-1} at 700°C, before decreasing to very low values again at the highest annealing temperature. The sheet carrier concentration has

values of the order of 10^{11} cm^{-2} for all annealing temperatures. The sheet resistance increases to 4 x 10^5 Ω/□ after annealing at 500°C, then drops to a value of ~ 1.5 x 10^5 Ω/□ for annealing at 600°C, above which it increases monotonically with annealing temperature. In the previous Chapter, it was found that activation of Fe deep levels occurred in InP above an annealing temperature of 600°C, and that a type conversion from n - to p - occurred at this annealing temperature. In this case, no transition to p - type was measured, however a similar activation may have begun to occur at these higher annealing temperatures, in addition to the progressive annealing out of shallow donors, causing the sheet resistance to rise with annealing temperature. This result does not exclude the possibility, however, of p - layers existing where the concentration of implanted Fe is highest, surrounded by n - type layers whose overall concentration of n-carriers is higher.

Thus, annealing at 500°C reduces the number of defects such that hopping conduction is significantly reduced and the sheet resistance is increased. Annealing at 600°C corresponds to the onset of activation of the shallow donor levels, which can also be seen in the sudden increase in mobility, and the sheet resistance may be increasing for annealing at temperatures above this due to the activation of ever greater concentrations of Fe acceptors.

No type change was found for the 10^{16} cm^{-2} implantation case either. In this case the evolution of R_s with annealing temperature is similar. There is a sudden increase in the sheet carrier concentration at an annealing temperature of 600°C, which could be due to the activation of a large concentration of shallow donors, which then decreases at 700°C due to the activation of the acceptor levels. The evolution of the effective mobility is also consistent with this picture, with a maximum (albeit a small one when compared to the values for 10^{15} cm^{-2} implantation) at 600°C annealing.

Since it is to be expected that materials with the shortest decay times will be obtained for the lowest annealing temperatures, and since large sheet resistivities were obtained for annealing at 500°C for the room temperature 10^{15} cm^{-2} implanted samples in particular, samples implanted at this dose were chosen for an optical study using time resolved photoluminescence. Besides which, the investigations into the damage resulting from the implantation using DCXRD and XTEM have shown that amorphous regions exist for Fe ion implantation at 10^{16} cm^{-2} into these samples, even after annealing at 800°C. Because of this, the higher dose implanted samples were deemed unsuitable for optical analysis.

Time-resolved optical measurements performed on samples implanted to 10^{15} cm^{-2}, are shown in Figure 6.12. Fig. 6.12(a) shows TRPL transients. For an undoped InGaAs sample measured under the same conditions as the implanted samples, there is a rather long PL decay time of 120 ps, which is determined by Auger recombination. Thus, the short PL decay times in implanted samples reflect carrier trapping into deep centers. The PL decay times, equal to 1.3, 2.5, 4.0 and 4.5 ps for the implanted samples annealed at 500 to 800°C, were determined by fitting the PL transients. During the fits, prolonged carrier relaxation, manifesting itself in the long PL rise time for the unimplanted sample (inset to Fig. 6.12(a)), was taken into account. As mentioned in Chapter 3, the high, compared to the band gap, excitation energy establishes long times for electron relaxation to the bottom of the band, which, in turn, results in long PL rise times and prolonged PL decay times. While, for LT GaAs, where the process of electron scattering to the bottom of the band affects the PL transient, and the PL decay becomes considerably longer than the electron trapping time,[14] the situation in InGaAs for the 800 nm excitation is even more severe: electron scattering to and from the L valleys further delays the relaxation.[15]

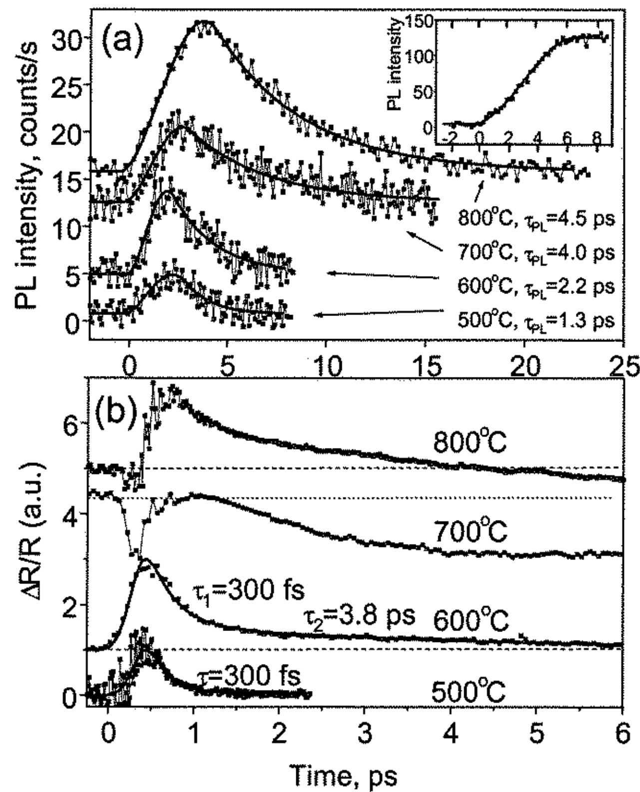

Figure 6.12 (a) Measured and simulated TRPL traces from annealed InGaAs samples implanted at room temperature with a dose of 10^{15}cm^{-2}. The curves for different samples are shifted vertically for clarity. The inset shows the rising part of the PL transient for the unimplanted sample. (b) Differential reflectivity measurements of the same samples excited with band gap energy photons. The horizontal lines indicate the reflectivity before excitation. Note different time scales for both graphs.

In an attempt to avoid the relaxation phenomena and determine real electron trapping times, TRDR measurements at the band gap wavelength were also performed (Fig. 6.12(b)). To evade coherent artefact effects, pump and probe pulses had orthogonal polarisations, however, some coherent oscillations still distort the rising part of the curve for the 500°C sample. The TRDR dynamics for the implanted InGaAs samples annealed at 500 and 600°C

show a single peak, which, after a fit to a function suggested by Roux *et al.*,[16] provides electron trapping times of 300 fs. For the 500°C sample, the trapping time is probably even shorter but is obscured by the temporal resolution of the experiment. In the 600°C sample curve, a longer tail with a characteristic time of about 3.5 ps appears, which can be attributed to changes in absorption from the mid-gap traps.[17,18] According to the model, trapping of one carrier type to the mid-gap centers occurs with a characteristic time of 300 fs, and subsequent recombination by the trapping of the other carrier type occurs at the slower rate of 3.5 ps. For the 700 and 800°C annealed samples, the TRDR transients are more complicated. Here there are three different changes in reflection. The initial fast decrease persists for a time at least of the order of 100 ps. A possible explanation for this long-term component consistent with the electrical measurement data could be electron excitation from the deep Fe-related centers, which are expected to be present in samples annealed at higher temperatures at larger densities, and subsequent trapping to the shallow donors. As far as donor levels are concerned, the As-antisite was observed to occur in smaller concentrations in LT-InGaAs when compared to LT-GaAs, which has been used to explain longer absorption recovery time for LT-InGaAs[11]. After annealing at 600°C, the antisites have also been observed to form precipitates which, being small and widely spaced, were considered to act as slow recombination centers.[15] At these donor sites, the carriers can stay for a long time before thermal reemission into the conduction band and subsequent recombination. On top of this long transient, band-to-band carrier excitation, and trapping and recombination manifests itself through the positive peak in the TR transient. Decay times for these peaks have similar characteristic times to that of TRPL.

Summary

Prior to annealing, the electrical characteristics of room temperature and 200°C Fe ion implanted InGaAs are dominated by the interplay of shallow donor and deep trap formation, which overall increase the original unimplanted values of sheet resistivity by several orders of magnitude while decreasing the effective mobility. Room temperature implants at 10^{16} cm^{-2} result in amorphous layers which cannot be recovered by annealing. Extreme damage is also observed for 200°C implants, however the structural damage can be recovered somewhat by annealing at 800°C. The different defect agglomeration and dynamic annealing properties of InGaAs when implanted, as compared to InP, were noted. Annealing the implanted samples at 600°C caused the formation of large concentrations of shallow donors. At annealing temperatures above this, Fe activation began to affect the electrical properties of the samples, markedly increasing the sheet resistance and decreasing the sheet carrier concentration and effective mobility. Similarly to the case for Fe ion implanted InP, the shortest carrier lifetimes in InGaAs are achieved at annealing temperatures much lower than those which have been associated with Fe activation. As discussed in Chapter 4, the production of shallow donors in InGaAs by implantation results in fairly low maximum resistivities when compared to other semiconductors such as GaAs. Consequently the values for R_s achieved here, by implanting the undoped material, while being lower than for similar experiments with InP as discussed in the previous Chapter, are at the upper limit of what is achievable for n-InGaAs. A jump in sheet resistance to a value of 4×10^5 $\Omega/\square$ occurs for samples implanted at room temperature to a dose of 10^{15} cm^{-2} when annealed at 500°C, where shallow donor activation has not yet become dominant. Around this annealing temperature, the carrier lifetime is also extremely short, at most 300 fs, indicating that these implantation conditions deliver InGaAs layers with characteristics appropriate for ultrafast optoelectronic applications.

6.4 MeV P ion implants into p - InGaAs

An alternative method for achieving ultrafast optical responses while maximising sheet resistivity can be explored using P ion implants into p -type layers, as was already shown in Chapter 5 for InP. The results of Hall effect measurements on 1.5 μm p -InGaAs-on-SI InP layers implanted at room temperature to a range of doses and annealed at 500 and 600°C for 60 seconds are shown in Figure 6.13. At the lower doses, between 10^{12} and 10^{14} cm^{-2} and for annealing at 600°C, the slight damage which is accompanied, it is assumed, by large concentrations of donor levels, causes low sheet resistances, high sheet carrier concentrations and decreasing effective mobilities. In contrast to p -InP implantation, compensation of the p carriers does not coincide with the maximum values of R_s. For annealing at 500°C, majority carriers are all n -type, whereas for annealing at 600°C, the majority carriers remain p -type up to a dose of 7.7 x 10^{16} cm^{-2}. In the former case, the maximum value of R_s is obtained at a dose of 5 x 10^{16} cm^{-2}, while for the latter, the optimum dose is between 5 x 10^{15} and 1 x 10^{16} cm^{-2}. In other words, conversion to n -type majority carriers, along with maximum R_s, requires a higher dose for annealing at 600°C as compared to 500°C. Annihilation of shallow donors is therefore stronger at the higher annealing temperature, and thus higher doses are required to create a sufficient quantity to compensate the free holes in the material. The fact that conversion from p - to n -type does not coincide with the maximum in R_s points to a layered conductivity within the implanted and annealed samples. The annealing at 500 and 600°C has allowed for sufficient recovery of the material (except for the highest doses) such that hopping conduction is no longer governing the electrical properties, and compensation of the free holes by shallow donors is the main effect. We see that for the higher doses, maximum R_s values of up to 4 x 10^6 Ω/□ were achieved. This is as good if not better than the optimum values

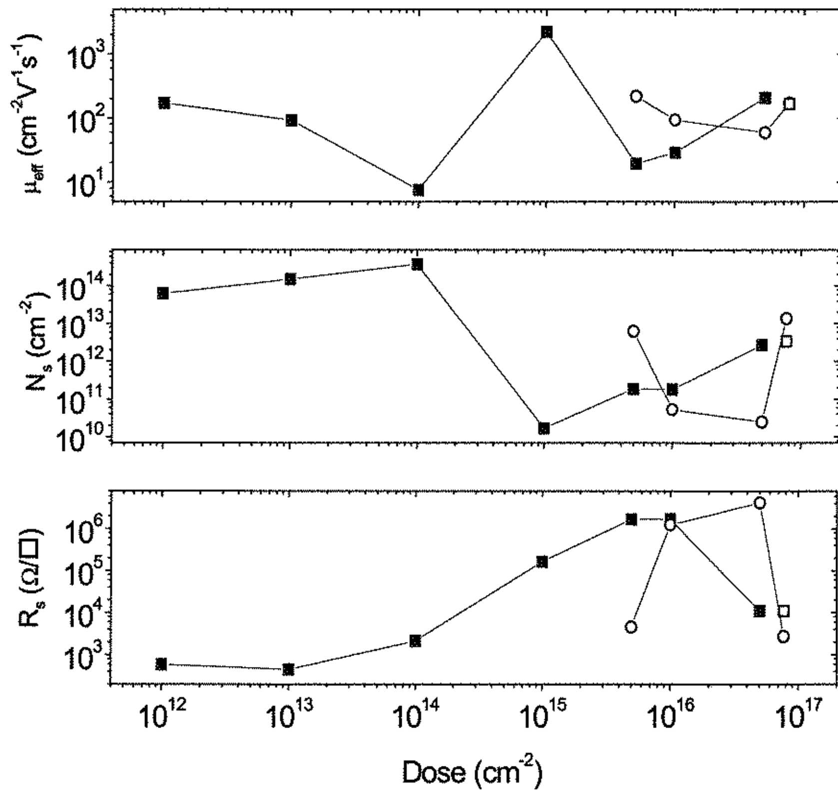

Figure 6.13 Effective mobility, μ_{eff}, sheet carrier concentration, N_s and sheet resistance R_s for *p* -InGaAs implanted at room temperature with 1 MeV P ions as a function of dose and for annealing at 500°C (circles) and 600°C (squares) for 60 seconds. Open symbols indicate *n* -type and closed symbols indicate *p* -type.

obtained for implanted *p* -InP. At such doses, the mobilities are no greater than a few hundred cm^{-2}V^{-1}s^{-1}, which is acceptable in certain device applications, and which also indicates that the optimum conduction path through this material is not dominated by hopping mechanisms.

The effect of the implantation on the strain profile can be seen in the X-ray curves of Figures 6.14 and 6.15. P, with its smaller atomic mass than Fe, causes a lesser degree of damage for implants at the same dose and temperature. While, for implantation to a dose of 10^{15} cm^{-2}, the peak due to the InGaAs is still present in the un-annealed material, implanting above 10^{16} cm^{-2} results in almost complete annihilation of this feature, leaving only the peak

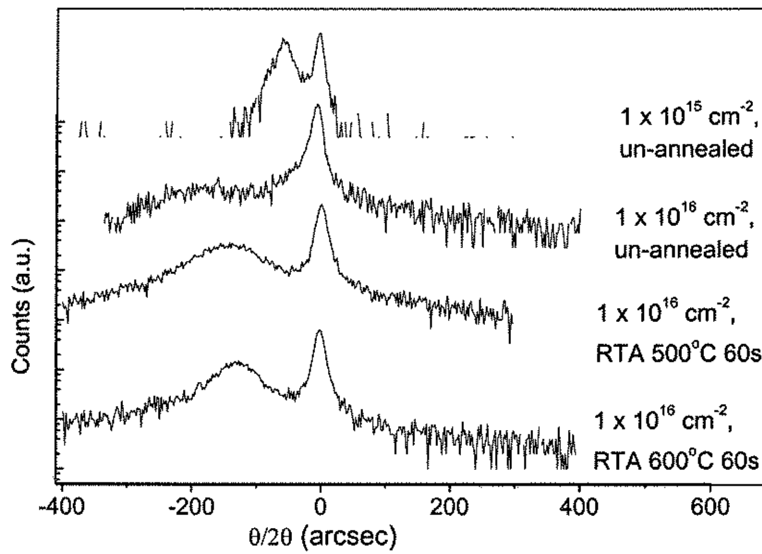

Figure 6.14 X-ray rocking curves of room temperature 1 MeV P ion implanted p -InGaAs to a dose of 10^{16} cm^{-2} as a function of annealing temperature. For comparison the spectrum of an un-annealed sample implanted to 10^{15} cm^{-2} is also included. Spectra vertically shifted for clarity.

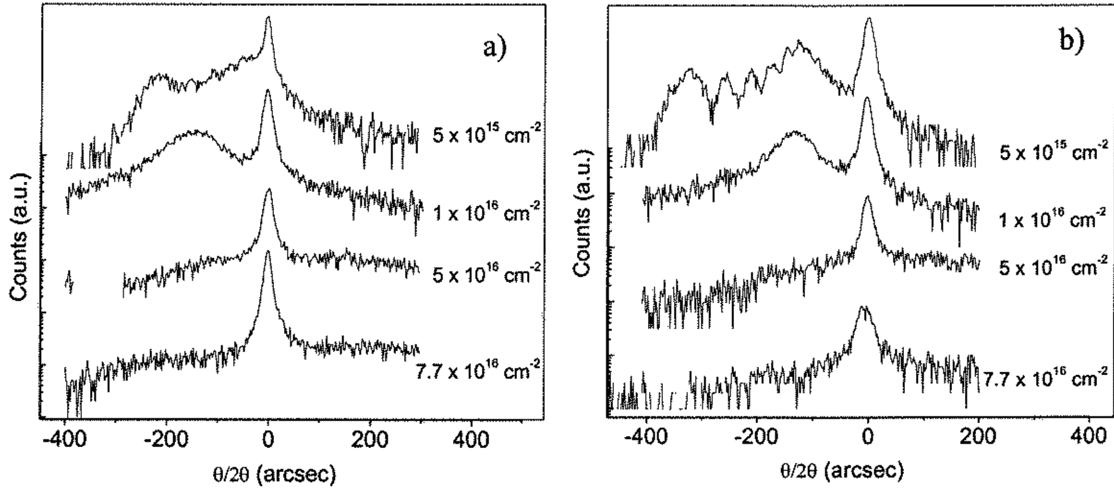

Figure 6.15 Evolution of X-ray rocking curves for 1 MeV P ion room temperature implanted p -InGaAs as a function of dose for (a) 500°C and (b) 600°C annealing for 60 seconds. Spectra vertically shifted for clarity.

from the InP substrate. In Fig 6.14, we see the effect of annealing on the recovery of the crystalline integrity of the p -InGaAs. For 500°C annealing, the p -InGaAs peak has been recovered although it is broadened compared to the un-implanted peak, as well as being shifted to slightly more negative θ/2θ. Annealing at 600°C recovers the p -InGaAs further, shifting it back towards the substrate peak as well as narrowing the FWHM. However, this annealing temperature is not sufficient to return the sample to its unimplanted form, indicating the large numbers of residual defects still present in the material. Figure 6.15 shows the effect of these two annealing temperatures on samples implanted to doses presented in the Hall effect results of Fig 6.13. The higher annealing temperature produces better recovery of the p -InGaAs, although at the highest two doses the damage appears too great; perhaps irreversible damage has been created by implanting at these doses.

Once again, if a comparison is made between the damage formed in InGaAs epilayers by MeV P ion implants and those already discussed in Chapter 3 on InP, the striking difference in the damage accumulation and agglomeration processes between the two semiconductors becomes evident.

Several attempts were made to analyse the optical properties of the implanted p -InGaAs through time resolved photoluminescence and differential reflectance measurements. However, no data was obtained, most likely due to the high doses used to achieve compensation of the material; the large amount of damage has probably caused the response times to be below the detection limit of the experiment. Future work could be done using p -type material with a lower initial free carrier concentration, which would then require lower doses to achieve compensation and thus hopefully provide material with measurable optical response times.

Summary

P ion implants into *p* -type InGaAs layers produced less damage than for Fe ion implants under the same conditions, due to the lower atomic mass of P. Values of R_s in some cases exceeding those found using the same method to implant InP in the previous Chapter were produced. Optimum doses did not correspond to a conversion from *n* - to *p* - type material, suggesting multiple paths of conduction within the material. Lower annealing temperatures allowed for lower optimum doses, which is ideal from the point of view of decreasing device response times. Structural studies showed that damage in samples implanted to 10^{16} cm^{-2} could be partially recovered by the annealing.

6.4 Conclusion

Similarly to the case for implanted InP, high resistivity InGaAs is achievable using either Fe ion implantation into undoped material, or P ion implantation into *p* -type material. In spite of the ease with which shallow donors can be formed in InGaAs, implants into the *p* - type InGaAs actually resulted in sheet resistivities as good if not better than those achieved by implanting into *p* -InP. However, the doses at which this high resistivity was achieved created too many defects for optical lifetimes to be measured. In the case of Fe ion implanted undoped InGaAs, the annealing temperatures at which the fastest decay times were achieved (300 fs as measured by differential reflectance for annealing at 500°C for 60 seconds), were not sufficient to activate the Fe trapping centres, resulting in sheet resistivities of $\sim 5 \times 10^5$ Ω/□. The high annealing temperatures required for Fe activation within the InGaAs matrix resulted in optical lifetimes of the order of picoseconds.

Implantation into p-InGaAs samples with initial free carrier concentrations lower than that used for this study ($< \sim 3 \times 10^{19}$ cm^{-3}), thus requiring lower doses to achieve the high resistivities, is the most promising direction for further research into creating InGaAs with optimum characteristics for use in ultrafast photodetectors.

References

1. S. Gupta, J. F. Whitaker, and G. A. Mourou, IEEE J. Quantum Electron. **28**, 2464 (1992).
2. Y. Chen, S. S. Prabhu, S. E. Ralph, and D. T. McInturf, Appl. Phys. Lett. **72**, 439 (1998).
3. D. Vignaud, J. F. Lampin, E. Lefebvre, M. Zaknoune, and F. Mollot, Appl. Phys. Lett. **80**, 4151 (2002).
4. E. Lugagne Delpon, J. L. Oudar, N. Bouché, R. Raj, A. Shen, N. Stelmakh, and J. M. Loutrioz, Appl. Phys. Lett. **72**, 759 (1998).
5. L. Joulaud, J. Mangeney, J. M. Lourtioz, P. Crozat, and G. Patriarche, Appl. Phys. Lett. **82**, 856 (2003).
6. S. J. Pearton, C. R. Abernathy, M. B. Panish, R. A. Hamm, and L. M. Lunardi, J. Appl. Phys. **66**, 656 (1989).
7. B. Tell, U. Koren, and B. I. Miller, J. Appl. Phys. **61**, 1172(1986).
8. U. G. Akano, I. V. Mitchell, F. R. Shepherd, and C. J. Miner, J. Vac. Sci. Technol. A. **10**, 996 (1992).
9. U. G. Akano, I. V Mitchell, F. R. Sheperd and C. J. Miner, Nucl. Instrum. Meth. in Phys. Res. B **106**, 308 (1995)
10. H. Künzel, J. Böttcher, R. Gibis, and G. Urman, Appl. Phys. Lett. **61**, 1347 (1992)
11. B. Grandidier, H. Chen, R. M. Feenstra, D. T. McInturff, P.W. Juodawlkis and S. E. Ralph, Appl. Phys. Lett. **74**, 1439 (1999).
12. B. Tell, U. Koren, and B. I. Miller, J. Appl. Phys. **61**, 1172(1986)

13. S. M. Gulwadi, M. V. Rao, A. K. Berry, D. S. Simons, p. H. Chi, and H. B. Dietrich, J. Appl. Phys., **69**, 4222 (1991)

14. A. Krotkus, R. Viselga, K. Bertulis, V. Jasutis, S. Marcinkevičius, and U. Olin, Appl. Phys. Lett. **66**, 1939 (1995)

15. A. I. Lobad, Y. Kostoulas, G. W. Wicks, and P. M. Fauchet, *Hot Carriers in Semiconductors*, edited by K. Hess et al. (Plenum, New York, 1996) p. 97.

16. J.-F. Roux, J. –L. Coutaz, and A. Krotkus, Appl. Phys. Lett. **74**, 2462 (1999).

17. A. Krotkus, K. Betrulis, M. Kaminska, K. Korona, A. Wolos, J. Siegert, S. Marcinkevičius, J.-F. Roux, J. -L. Coutaz, IEEE Proc. Optoelectronics, **149**, 111 (2002).

18. P. W. Juodawlkis and S. E. Ralph, Appl. Phys. Lett. **76**, 1722 (2000)

CHAPTER 7

Ion Implantation Induced Interdiffusion in InP and InGaAs based Quantum Wells

7.1 Introduction

Interdiffusion of quantum well structures has been explored since the early 1980s as a promising technique for both the tuning of the quantum well (QW) emission/detection wavelength as well as monolithic integration of optoelectronic devices on a single chip. Interdiffusion is achieved, typically through an annealing step, by the exchange of elements between the quantum well and barrier, and is driven by the discontinuity of each element which occurs at the quantum well/barrier interface. In this way, the composition of the materials near the interface is altered, typically smoothing the initially square well potential to approximately a double error function potential as shown in Figure 7.1. As the shape of the potential is changed, the energy eigenstates of electrons and holes within the quantum well are altered. Typically, the effective bandgap of the quantum well is increased after interdiffusion, resulting in a wavelength blueshifting.

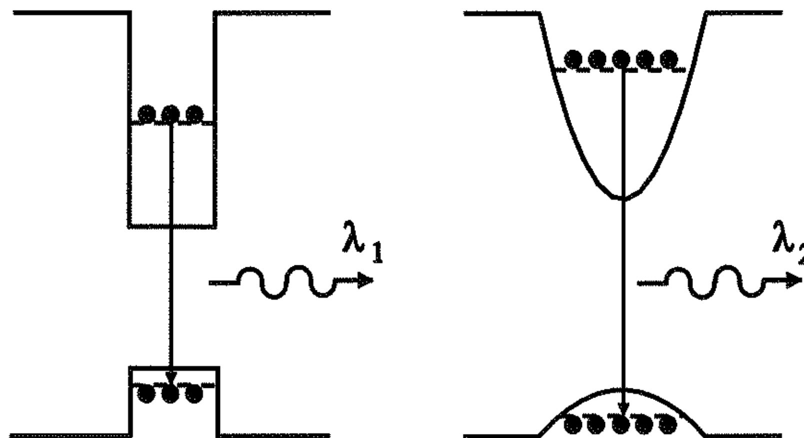

Figure 7.1 Schematic of quantum well interdiffusion.

Quantum well structures such as GaAs/AlGaAs and GaAs/InGaAs (hereafter referred to as group III- diffusion systems) have been studied extensively, however our understanding of systems involving InP/InGaAs, InP/InGaAsP, InAsP/InGaAs and other combinations (hereafter referred to as group V/III- diffusion systems) has been more contentious. This debate arises from the added complexity associated with interdiffusion in group V/III- diffusion QW systems: the interrelated effects of strain and the possibility of varying ratios of group V and group III diffusion lengths. In the GaAs/AlGaAs QW system, for example, these issues do not exist, since the material will remain lattice-matched regardless of the composition of the AlGaAs, and only the group III elements will interdiffuse since the concentration of As across the barrier/well interface remains constant. Thus, understanding the effects of interdiffusion in group III- diffusion quantum well structures, such as the blueshifting of the photoluminescence, is more straightforward. In the case of the InP/InGaAs system, modelling has been used to understand how varying the group III and/or group V interdiffusion will affect strain, the shape of the quantum well profile and the transitions between the electron and hole eigenstates[1]. Such computer simulations reveal the possibility of bandgap tuning to degrees not achievable in the group III - diffusion systems. When added to the potential for applications in 1.3 and 1.55 μm range, interdiffusion in group V/III- diffusion quantum well systems presents an exciting topic for research.

Many studies into interdiffusion in this groupV/III- diffusion system, using a range of techniques such as implantation induced intermixing, impurity free vacancy disordering (IFVD) and laser annealing[2-10], have reported varying ratios of group III and group V diffusion coefficents. Different mechanisms are brought to the fore depending on the method used, and thus the type of interdiffusion can potentially be tailored.

In the case of ion implantation induced interdiffusion, defects created by the implantation process are used to drive the mixing of quantum well and barrier materials via an annealing step (illustrated below). The focus of this work is on understanding diffusion mechanisms in InP/InGaAs quantum well structures; comparative studies on InGaAs/AlInGaAs quantum wells (where the group III interdiffusion is favoured) were also done.

7.2 Experimental

For this study, four wafers were grown by metalorganic chemical vapour deposition (MOCVD) on (100) semi-insulating InP substrates. Their structures are illustrated in Figure 7.2. Two wafers had a single 5 nm $In_{0.53}Ga_{0.47}As$ quantum well and InP barriers, one with a 250nm InP cap layer and the other with a 200nm InP barrier followed by a 50 nm $In_{0.53}Ga_{0.47}As$ capping layer. The remaining two wafers had a single 5 nm $In_{0.53}Ga_{0.47}As$ quantum well and $Al_{0.2}Ga_{0.27}In_{0.53}As$ barriers, one with an InP cap and one with an $In_{0.53}Ga_{0.47}As$ cap. All of the quantum well samples were implanted with P^- ions at 20 keV as well as P^+ ions at 1 MeV, TRIM simulations predicting the damage to lie within the first 50 nm (within the capping layer) and 1 μm from the surface, for these two energies respectively. The calculated profiles of total vacancies as a function of depth into the sample are shown in Figure 7.3, with the role played by these implants on the interdiffusion process depicted in Figure 7.4. Doses ranged between 10^{12} and 10^{14} cm^{-2}, and all implants were performed with a constant flux of 7 nA/cm^2 and the sample tilted at 7° from the normal direction of the beam to minimise channeling effects. In each case one half of the sample was masked in order to provide an unimplanted reference. Rapid thermal annealing (RTA) for 60s was conducted on

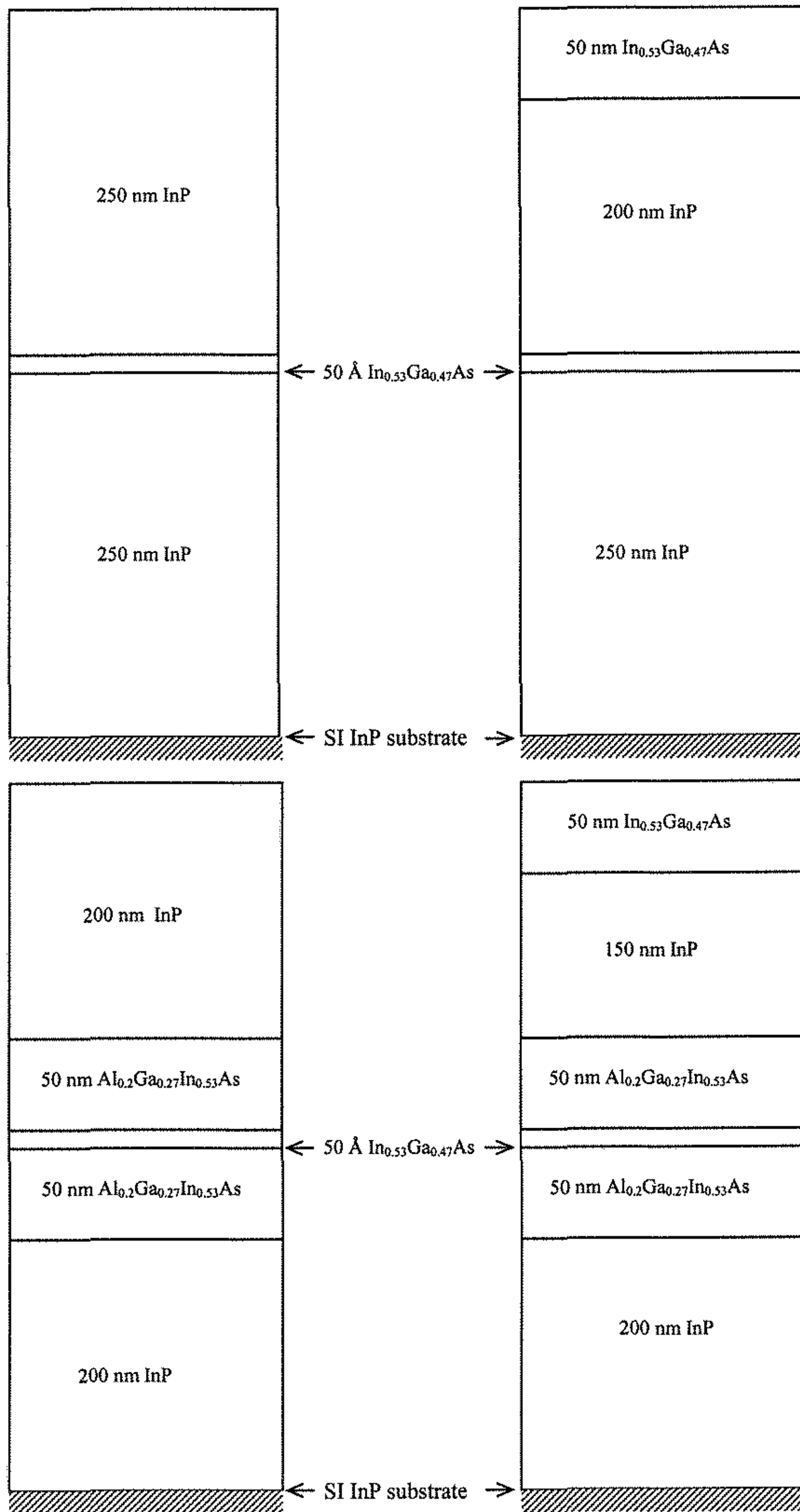

Figure 7.2 Schematic of quantum well epitaxial structures used in the study.

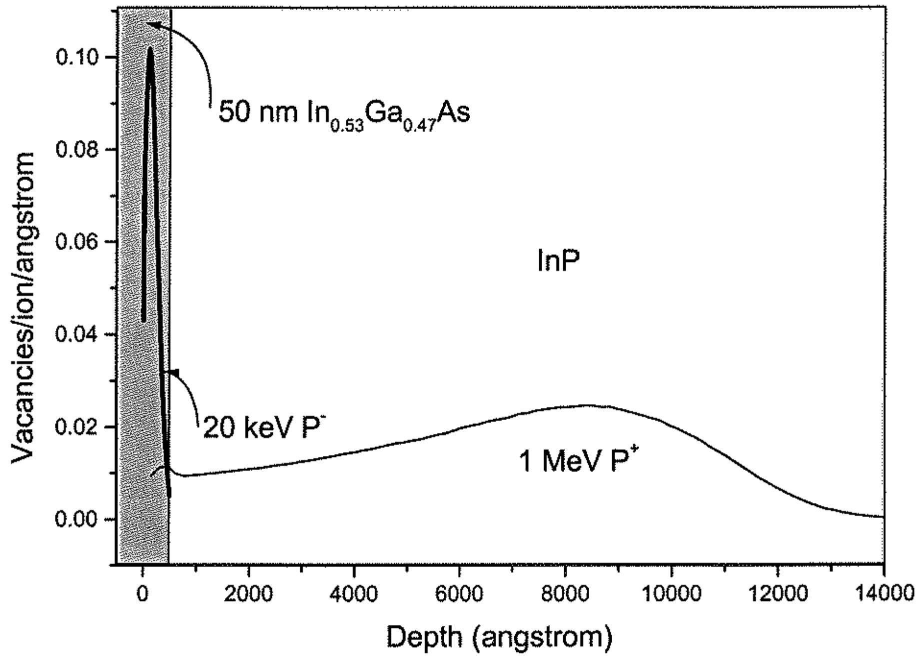

Figure 7.3 Vacancies produced by implanting into InGaAs epilayers on InP as a function of depth, calculated by TRIM.

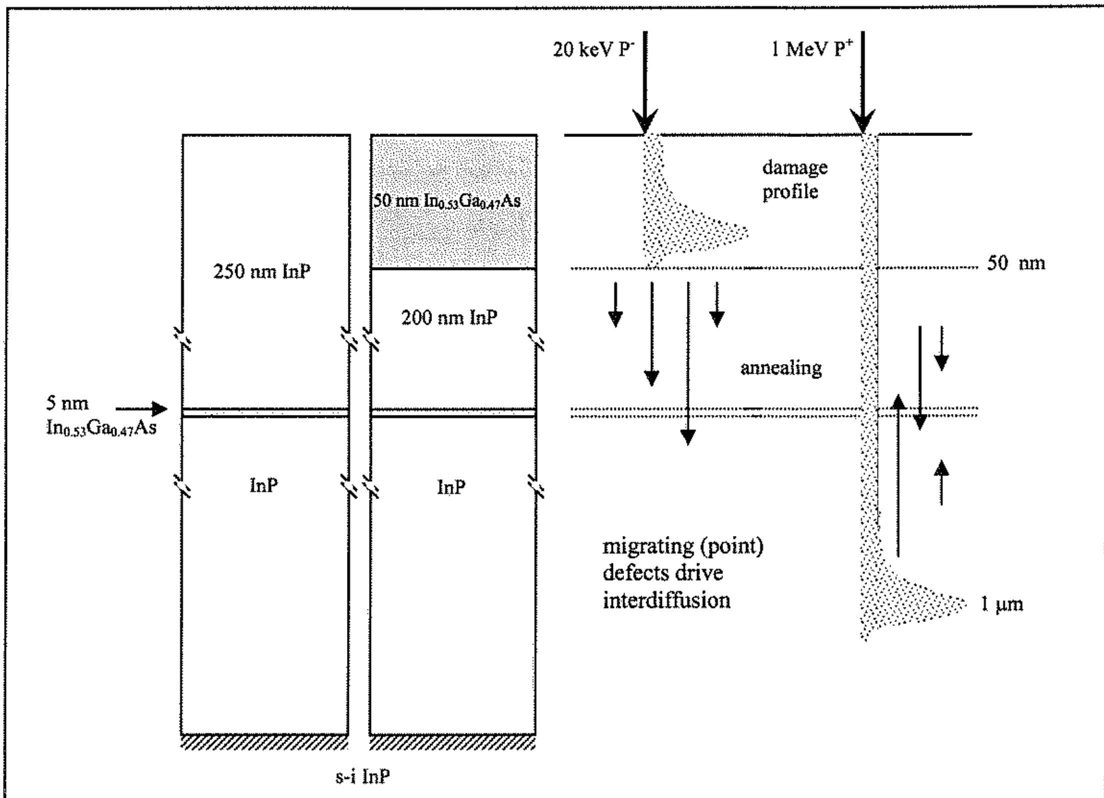

Figure 7.4 Schematic of quantum well interdiffusion induced by ion implantation (low and high energy cases depicted).

the samples after implantation. Photoluminescence (PL) at 77K, using a red diode laser at 670 nm, and an InGaAs photodetector through a 0.5 m monochromator, was used to measure the shifts in quantum well emissions. The relative PL energy shifts were calculated from the difference between the emission energy of the implanted side and that of the (annealed) reference side on the same sample. To provide information on the damage produced by such implants, Rutherford backscattering spectrometry-channeling using 2 MeV He ions was also performed with a 10° glancing angle geometry.

7.3 Thermal Stability of the Quantum Wells

Interdiffusion will occur spontaneously if enough energy is provided to allow migration of quantum well and barrier elements across the interface. Since the methods which drive the interdiffusion in this work all make use of an annealing step, it is important to study the interdiffusion caused by purely thermal effects.

Figure 7.5 shows the peak energy of the quantum wells measured by photoluminescence as a function of cumulative annealing for 60 seconds at different temperatures. As the annealing temperature is increased, the peak energy shifts to higher values in all cases (corresponding to a blueshifting of the wavelength). The greatest peak shifts occurred for the InP capped, InP/InGaAs sample. Capping this quantum well structure with InGaAs seemed to reduce the susceptibility of the structure to thermal effects. The InGaAs/AlGaInAs quantum wells showed a much higher thermal stability, and even after annealing to 850°C, the peak emission had only shifted 0.012 eV from the original value. It would appear that the greater the opportunity for group V intermixing (such as using an InP

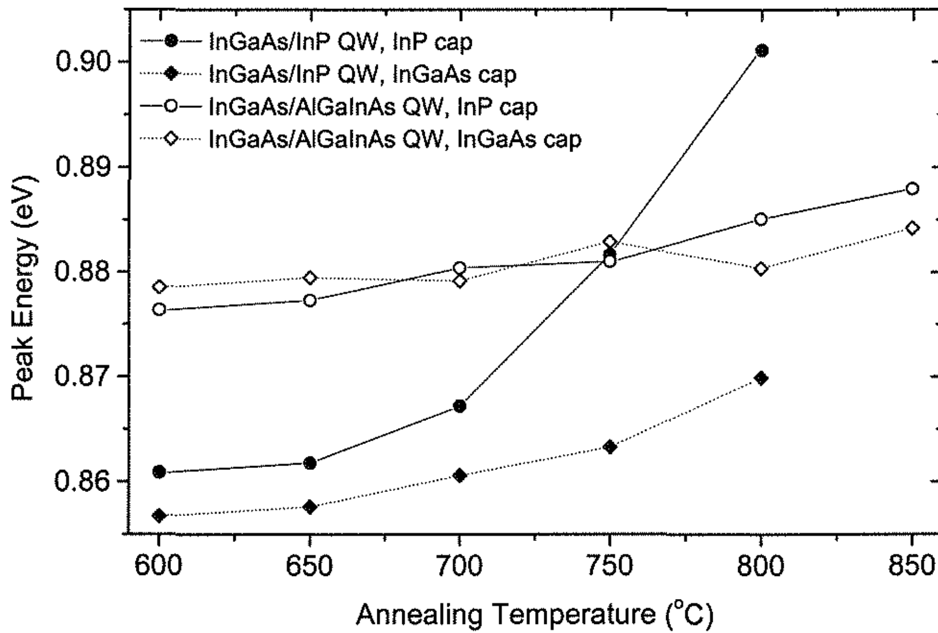

Figure 7.5 77K photoluminescence peak energy of InP/InGaAs quantum wells (with InP or InGaAs cap) and InGaAs/AlGaInAs quantum wells (with InP or InGaAs cap) as a function of annealing temperature. Annealing was cumulative, for 60 seconds in all cases.

cap or having groupV/III- diffusion quantum wells), the more blueshifting can be achieved. Group III intermixing appears to require higher annealing temperatures (which has also been found for GaAs/AlGaAs quantum wells, where annealing temperatures >800°C are required to achieve significant blueshifting)[11].

Based on this study of the temperature dependence of interdiffusion, an annealing temperature and time of 700°C and 60 seconds was chosen for the subsequent experiments involving implantation, so as to be certain that any measured peak energy shifts were not due to these thermal effects.

7.4 Cap Layer Implants (Low Energy)

7.4.1 InGaAs/InP quantum wells

Implantation into a capping layer is a relatively non destructive technique in the sense that defects are not directly created in the quantum well region - annealing allows the defects to move down from the surface and promote interdiffusion, as shown in the schematic of Figure 7.4. The effect on interdiffusion of InP or InGaAs capping layers was compared, as well as the implantation temperature, following rapid thermal annealing (RTA) at 700°C for 60 seconds.

Figure 7.6 illustrates the post-annealing blue shift of the PL emission from the InP capped sample with increasing ion dose, when implanted with 20 keV P ions at 200°C. The FWHM stays fairly constant for doses at or below 5 x 10^{12} cm^{-2}, but becomes significantly broadened above this value. Figure 7.7 depicts the relative shifts for room temperature and 200°C implants on this sample, as a function of the same doses. As the dose is increased, the shift in emission from the sample implanted at 200°C increases to 90 meV at a dose of 10^{14} cm^{-2}, while for room temperature implantation the energy shift reaches a maximum of 40 meV at a dose of 10^{13} cm^{-2}, and decreases beyond this dose.

Figure 7.8 depicts the relative shifts for the InGaAs capped sample, as a function of dose, for 20 keV P ion implants at room temperature and 200°C. In this case, the energy shift increases with dose for both implantation temperatures. The shifts are marginally greater for implantation at room temperature than at 200°C. Figures 7.7 and 7.8 illustrate that the level of interdiffusion at a particular dose is greatly modified by the type of capping layer. Additionally, the temperature of implantation is producing a different evolution of shifts with dose.

In order to understand these differences in energy shifts, residual damage after ion

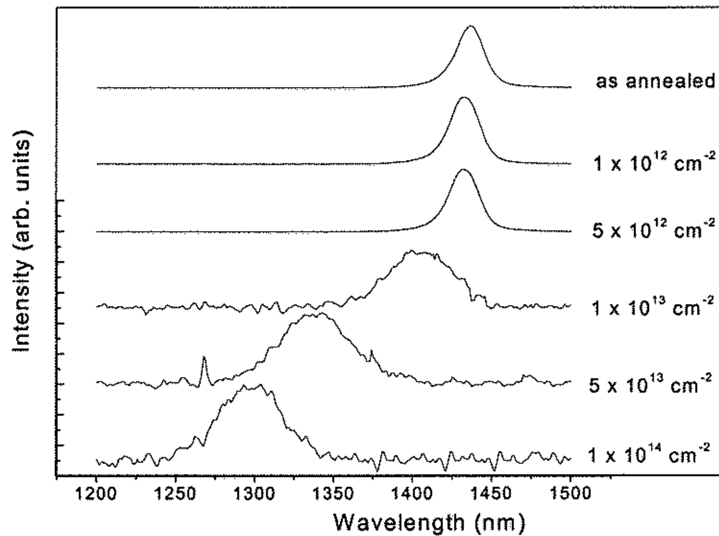

Figure 7.6 Low temperature (77K) photoluminescence spectra from InP/InGaAs quantum well structure implanted at room temperature with 20 keV P ions to various doses and rapid thermally annealed at 700°C for 60 seconds.

implantation was measured using Rutherford backscattering spectrometry- channelling (RBS-C). Figure 7.9 shows the glancing angle RBS-C spectra measured for the InP capped sample implanted with 20 keV P ions at room temperature to a dose of 10^{14} cm^{-2}. The region near the surface has been nearly amorphised at this implant temperature. A similar measurement for implantation at 200°C shows negligible variation from the unimplanted spectrum. Defect annihilation is an important characteristic of implanted InP - at room temperature it is known that over a period of many days the damaged material will begin to recrystallise[12]. It follows that, for implantation at 200°C, the dynamic annealing is significant. It is well known that there is a maximum amount of damage which can be induced in samples, beyond which point defects group themselves into clusters and do not diffuse sufficiently during annealing to

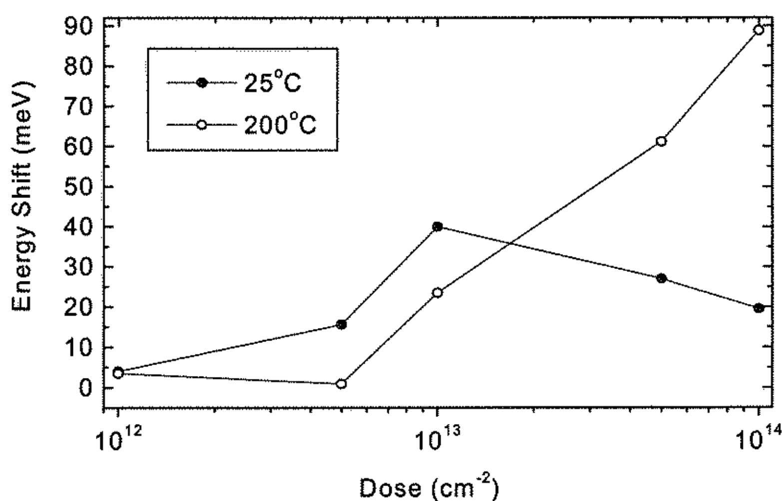

Figure 7.7 Energy shift of InP capped InP/InGaAs quantum wells as a function of dose for 20 keV P ion cap implants at both room temperature and 200°C. RTA at 700°C for 60s.

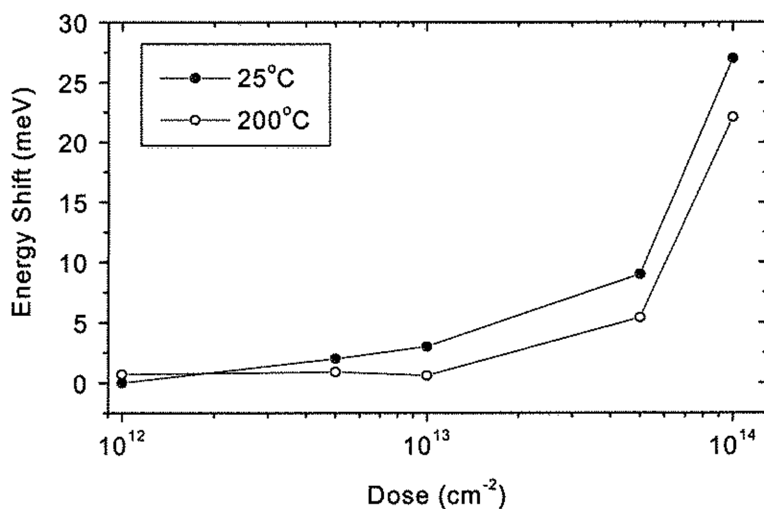

Figure 7.8 Energy shift of InGaAs capped InP/InGaAs quantum wells as a function of dose for 20 keV P ion cap implants at both room temperature and 200°C. RTA at 700°C for 60s.

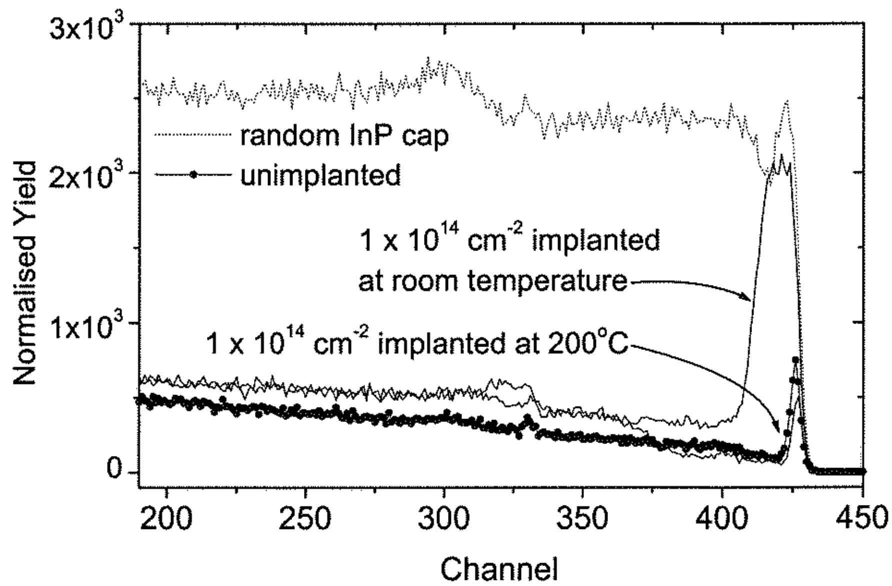

Figure 7.9 Glancing angle RBS-C spectra for the InP capped sample, implanted with 20 keV P ions to a dose of 10^{14}cm^{-2} at room temperature and 200°C. Random and channeled spectra for the as-grown sample are shown for comparison.

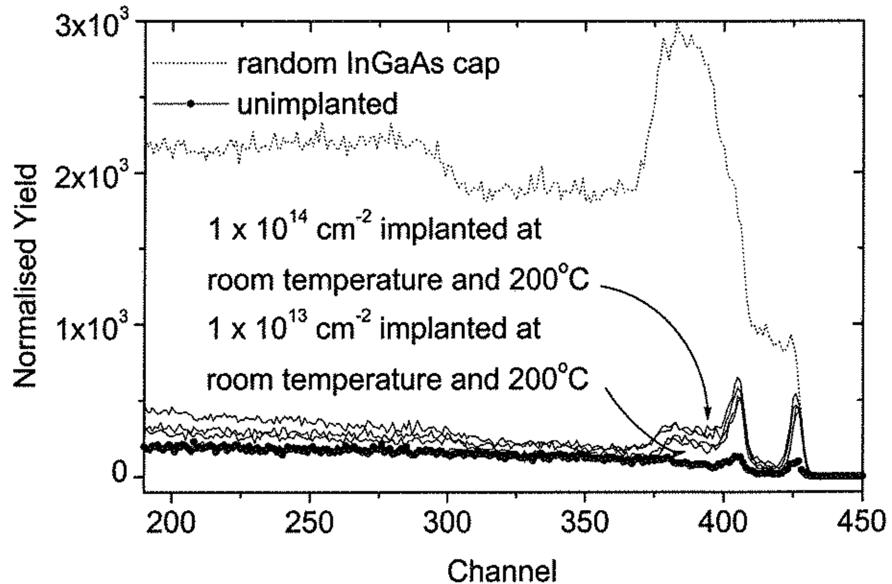

Figure 7.10 Glancing angle RBS-C spectra for the InGaAs capped sample, implanted with 20 keV P ions to a dose of 10^{13} and 10^{14} cm^{-2} at room temperature and 200°C. Random and channeled spectra for the as-grown sample are shown for comparison.

participate in the interdiffusion process[13-16]. At 200°C, amorphisation is suppressed and more point defects are generated, which will lead to enhanced interdiffusion. By contrast, for room temperature implantation of the InP capped sample, the defect clusters in the amorphised region have higher thermal stability and thus make a smaller contribution to intermixing. InP capped samples irradiated at a dose of 10^{13} cm^{-2} were also measured (not shown) for both implant temperatures, and again show very little difference from the unimplanted spectrum. This lack of significant damage at the lower doses correlates well with the large shifts observed. It is likely that, at this dose of 10^{13} cm^{-2}, the energy shift is slightly reduced for 200°C implantation, because at this temperature there are fewer point defects due to the dynamic annealing. The RBS-C spectra for the InGaAs capped samples are shown in Figure 7.10. All samples, for doses of 10^{13} and 10^{14} cm^{-2}, and for both room temperature and 200°C implantation, showed evidence of only a small amount of damage - there was no amorphisation. There is a very slight increase in the amount of damage for implantation at the higher dose, but almost no difference between the two implantation temperatures. We cannot distinguish between the type of damage induced at the different implant temperatures from the RBS-C measurements, however we propose that the decreased energy shifts observed for 200°C temperature implants into the InGaAs capped samples are due to a lower concentration of point defects. The number of point defects will be reduced by a greater amount of dynamic annealing and/or formation of clusters, and it is likely that such processes occur more readily at elevated implant temperatures (as for InP).

We have already had indications from the previous Chapters that the defect accumulation and diffusion mechanisms are different for the InP and InGaAs cap layers, and the RBS-C measurements show this conclusively. The nature of the defects is specific to the layer, as can be inferred from the unique temperature dependence of the dynamic annealing in

either InP or InGaAs. The In-P bond strength has been measured as ~ 198 kJ mol^{-1}, whereas the In-As and Ga-As bond strengths are ~ 201 and ~ 210 kJ mol^{-1} respectively[17]. Thus, the bonds in InP are much easier to break, and room temperature implantation into InP causes much more damage than implantation into InGaAs at the same temperature. For example, the room temperature amorphisation doses for Se implantation into InP, InAs and GaAs were measured to be 1.8×10^{13} , 7×10^{13} and 32×10^{13} cm^{-2}, respectively[18]. The indium and phosphorous self diffusion factors, D_o, in InP, are 1×10^5 and 7×10^{10} cm^2/s, respectively[17].

For In self diffusion in InAs, D_o is 6×10^5 cm^2/s, for As self diffusion in InAs it is 3×10^7, for As diffusion in GaAs it is 7×10^{-1} cm^2/s and for Ga self diffusion in GaAs it is 1×10^7 cm^2/s (values for InGaAs could not be obtained). It is not known how these values might change in the presence of (implantation-induced) defects, however they do provide some indication of the likelihood of diffusion of the constituent elements in either InP or InGaAs. The greatest photoluminescence energy shifts obtained were for implantation at 200°C into the InP capped sample. From the diffusion factors listed above, it can be inferred that phosphorous-associated point defects created in InP by implantation at 200°C will be very mobile, and by comparison, the degree of diffusion of any of the point defects created in InGaAs will be orders of magnitude less. It is possible that greater shifts are achievable in the InGaAs capped samples if the implants are done at higher doses.

Summary

Extensive damage in the capping layer was found to reduce the amount of interdiffusion due to the high thermal stability of the complex defects. Elevated temperature implants into the InP capped sample produced the greatest blueshifts, since amorphisation was suppressed and more mobile defects could be created in abundance at this temperature. The defect

accumulation and agglomeration processes in InP and InGaAs were revealed to be markedly different, as shown in the RBS-C results, with InGaAs showing minimal sensitivity to the implant temperatures used. In the case of InGaAs capped samples, room temperature implants resulted in a marginally higher energy shift than at 200°C, possibly due to the greater concentration of point defects created at the lower temperature.

7.4.2 InGaAs/AlGaInAs quantum wells

Figure 7.11 shows the effect of implanting into the InP capped InGaAs/AlGaInAs quantum wells, and Figure 7.12 shows the effect of implanting into the InGaAs cap of the same quantum well structure. In comparison to the InP/InGaAs quantum wells, the achievable shift is much less for implantation and annealing under identical conditions. Considering that the type and amount of defects created in the capping layer will be the same as for the previous section, different intermixing behaviour observed in this system must be attributed to the way these defects affect element exchange at the quantum well, which, in this case, is expected to favour diffusion on the group III sublattice. For the case of the InP capped samples, a plateau is reached for the higher doses at *both* implant temperatures. Therefore, in spite of a large amount of point defects in the InP cap for 200°C implants, which produced large blueshifts in the InP/InGaAs quantum well, the results of Figure 7.11 are suggestive of some kind of clustering or inhibition of the migration of these small defects into InGaAs/AlGaInAs system, especially when they are created in large quantities (high doses). The blueshift is only a few meV, indicating the greater thermal stability of this quantum well system as compared to the InP/InGaAs system. The saturation of blueshifting occurs at a lower dose for room temperature implantation with respect to 200°C implants. It is not necessary for the cap to be

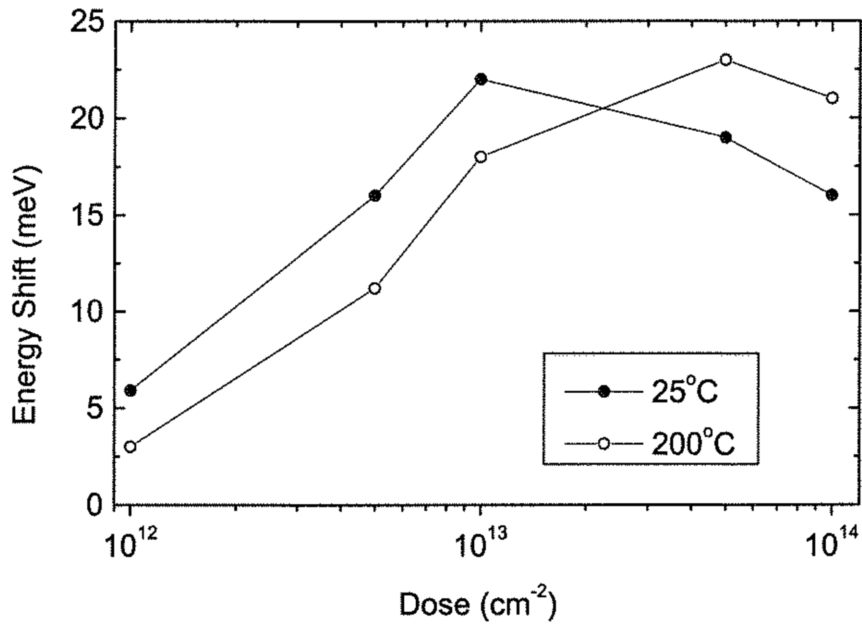

Figure 7.11 Energy shift of InP capped InGaAs/AlGaInAs quantum wells as a function of dose for 20 keV P ion cap implants at both room temperature and 200°C. RTA at 700°C for 60s.

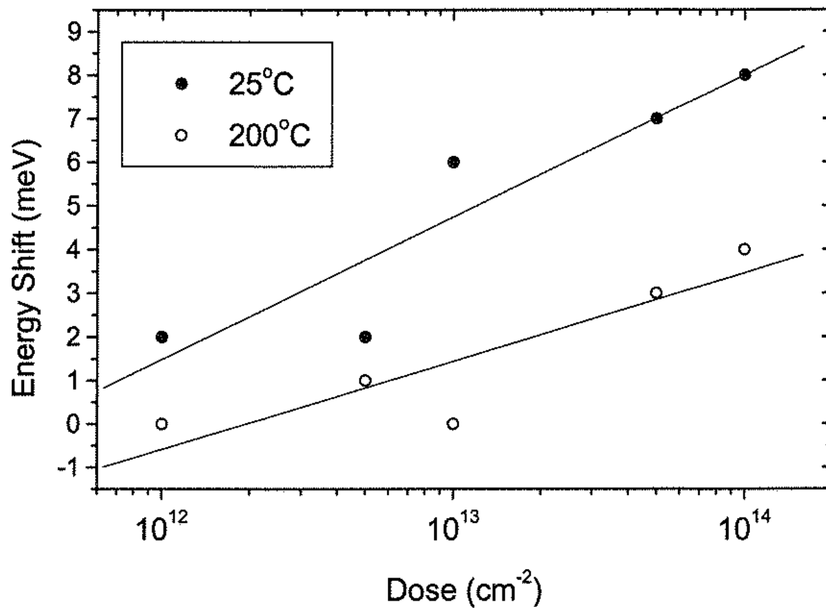

Figure 7.12 Energy shift of InGaAs capped InGaAs/AlGaInAs quantum wells as a function of dose for 20 keV P ion cap implants at both room temperature and 200°C. RTA at 700°C for 60s.

amorphised for this plateau to occur, since all that is required is a significant number of thermally stable defects as would be expected from highly damaged material.

Similarly to the InP/InGaAs quantum well case, the InGaAs capped samples exhibit greater resistance to interdiffusion under the same annealing conditions that were used for the InP capped samples. It is likely that no major shifts were observed in InGaAs capped sample due to strong dynamic annealing in the capping layer during implantation, in addition to the reduced tendency of the group III sublattice to diffuse. Once again, a larger shift occurs for room temperature implantation because at 200°C the dynamic annealing was sufficient to reduce the number of available point defects. The thermal stability study in section 7.1 has also shown that there is no incentive for thermal interdiffusion of this system even at the highest annealing temperatures, thus interdiffusion must be driven by some kind of defect injection process. The defects created in the cap layer appear to diffuse far more readily when a greater possibility exists for group V interdiffusion.

Because the shifts were so small for the initial annealing at 700°C, the effect of additional annealing steps on the interdiffusion was studied. For additional cumulative anneals for 60 seconds up to 900°C, the blueshifting of the InGaAs capped samples remained negligible, while that of the InP capped sample was markedly improved for very high temperature annealing.

Figure 7.13 shows that, for room temperature implantation, additional annealing at 700°C causes the blueshifting to increase while still exhibiting a maximum at a dose of 10^{13} cm^{-2}. Further annealing at 900°C causes the blueshifting to increase monotonically with dose, with very large blueshifts achieved for the highest doses. For 200°C implantation (Figure7.14), a similar trend is followed, however the amount of blueshifting achieved for 900°C annealing is

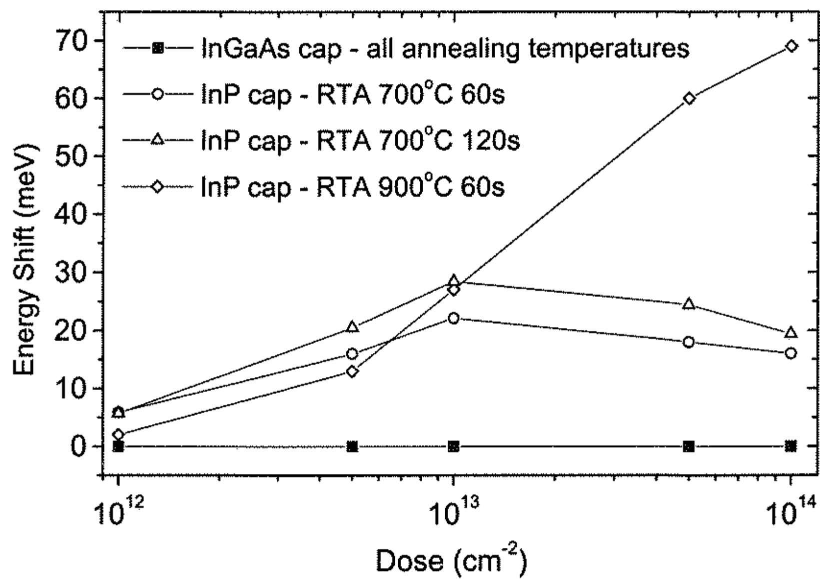

Figure 7.13 Energy shifts of InGaAs/AlInGaAs quantum wells as a function of dose for 20 keV P ion cap implants at room temperature, for different annealing temperatures and cap layers.

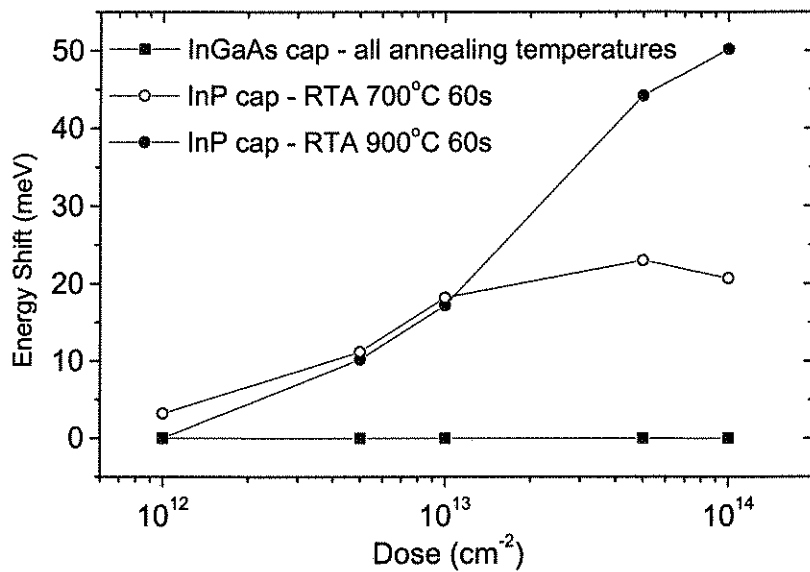

Figure 7.14 Energy shifts of InGaAs/AlInGaAs quantum wells as a function of dose for 20 keV P ion cap implants at 200°C, for different annealing temperatures and cap layers.

slightly less. This may be due to the lower concentration of defects produced in the InP cap with elevated temperature implantation, as previously illustrated by the RBS-C results in Figure 7.8. The removal of the plateau in the evolution of blueshift with dose for the two cases is an indication that the defects created in the capping layer, combined with the interdiffusion mechanisms specific to the InGaAs/AlGaInAs quantum well system, are not sufficient to induce any significant diffusion for annealing at temperatures below 900°C. Annealing at 900°C provides enough energy to release these defects and thereby allow for the large amount of interdiffusion, as evidenced by the blueshifts which are of comparable values to those that were measured for the InP/InGaAs system.

The enhanced blueshifting of the InP capped samples for additional annealings is also a strong indication that the presence of highly mobile P atoms will cause a great deal of interdiffusion. It is likely that this capping layer has allowed for group V interdiffusion, especially at the highest annealing temperatures which would have given the P atoms ample opportunity to migrate down to the quantum well region. Thus, by including a layer containing P in these quantum well systems, a large degree of interdiffusion can be obtained using the cap layer implantation technique.

In the case of InGaAs capped samples, the lack of blueshifts indicates that annealing at 900°C for 60 seconds was not sufficient to allow the group III defects to migrate to the quantum well region. This is consistent with the fact that the implant damage needed to be close to the quantum well region in InGaAs/AlGaAs quantum well systems which also rely on group III intermixing[16,19].

Summary

Cap layer implants into the InGaAs/AlInGaAs quantum well samples resulted in interdiffusion which was less extensive than that of the InP/InGaAs quantum well system, due to the decreased tendency of the group III elements to interdiffuse. InP capped samples exhibited greater blueshifting than the InGaAs capped samples, for similar reasons as were discussed in section 7.4. At the higher doses, a plateau in the amount of blueshifting was observed for the InP capped samples, which occurred for both room temperature and 200°C implants. This insensitivity to implant temperature indicates that the diffusion mechanisms in the InGaAs/AlInGaAs system are different to the InP/InGaAs system. The defects responsible for the saturation of blueshifting at the higher doses were only thermally stable to annealing temperatures below 900°C. By annealing at this highest temperature it was possible to release the defects from the InP capping layer and cause significant blueshifting, which was of comparable magnitude to the InP/InGaAs case. It is presumed that this behaviour is due to the highly mobile P defects, as was found in section 7.1.

7.5 Deep Implants (High Energy)

Figure 7.15 shows the effect of the different capping layers for both InP/InGaAs and InGaAs/AlGaInAs quantum well samples in the case of deep implant (1 MeV P ion) induced interdiffusion. The energy shifts as a function of dose are essentially the same for both capping layers because the defects can now migrate to the quantum well from both above and below. Both quantum well samples follow the same trend of increasing blueshift with increasing dose, although the interdiffusion for the InGaAs/AlGaInAs quantum well system is

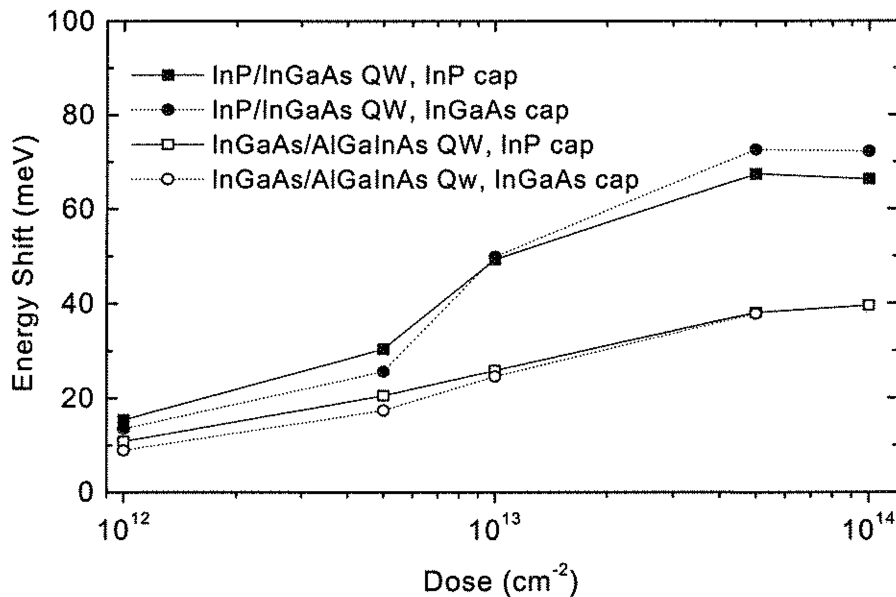

Figure 7.15 Energy shift as a function of dose for all quantum well samples after implants with 1 MeV P ions at 200°C and annealing at 700°C for two 60 second intervals.

less, due to its aforementioned higher thermal stability resulting from the dominant group III mechanism.

After annealing at 700°C for two 60 second intervals, the maximum energy shift achievable for the deep implants is still less than that for shallow implants into the InP capped sample. This may be due to the damage peak being located farther from the quantum wells in the high energy implantation case, as compared to the low energy implant case, which means the majority of defects - which are produced at the damage peak - must diffuse for a greater distance to influence the quantum well region. Another feature of the evolution of energy shifts with dose is the plateau which seems to be reached at the higher doses. At these doses the intermixing is probably saturated because of the onset of defect clustering, similarly to the case for room temperature InP cap implants.

Summary

For both the InP/InGaAs and InGaAs/AlInGaAs systems, the effect of the capping layer was absent in the case of deep implants, since the defects which drive the interdiffusion were able to migrate to the quantum well region from both above and below. This indicates that the implant induced defects can only diffuse over a relatively short distance. The former system produced a greater amount of blueshifting than the latter. In general the shifts were less than what was obtained using the low energy implantation technique, however this may be explained by the greater distance of the peak damage in the deep implant case to the quantum well region, as compared to the case for cap layer implants.

7.6 Conclusion

Interdiffusion driven by implant damage created in the cap layer was dependent both on the implant temperature and capping layer material (InP or InGaAs). In particular, this dependence was strongly correlated with the damage accumulation, dynamic annealing and defect agglomeration processes that occurred in the InP or InGaAs cap layers as a consequence of implanting in the two different semiconductors at different temperatures. The degree of interdiffusion was enhanced when large amounts of point defects were formed in the cap layer, and reduced when complex defects with high thermal stability were created. At elevated temperatures, highly mobile defects were created in the InP which produced the greatest amount of interdiffusion in the samples. The respective natures of damaged InP and InGaAs have already been contrasted in the previous Chapters; the interdiffusion studies decribed here show how these properties could be used to tailor blueshifting in the InP/InGaAs and InGaAs/AlGaInAs quantum well systems. While large blueshifts can

generally be achieved by the presence of an InP layer which contains highly mobile P-related point defects in the structure, alternate group III/V structures with high thermal stability, such as those containing combinations of InGaAs and AlGaInAs layers, could be grown expressly to be resistant to interdiffusion. In general, structures where group III interdiffusion is favoured do not interdiffuse as readily as those where disorder in both sublattices is possible. Furthermore, given enough energy via annealing at high temperatures or for long times, the extremely mobile P related defects created in InP capping layer could ultimately cause extensive group V interdiffusion in the group III mobile systems (such as the AlInGaAs/InGaAs case). When interdiffusion was driven by deep implants which passed through the quantum well itself, the effect of the cap layer was removed due to the opportunity for defects to migrate from both above and below the active region. When interdiffusion is generated using high energy deep implantation, only the tail of the damage profile is affecting the quantum well region. Although in the cap implantation case the quantum well was not directly affected, its distance from the region of higher defect concentration was less. The degree of blueshifting achieved in the deep implant case was not as substantial - even after additional annealing steps - as that obtained using the cap layer implantation technique.

References

1. J. Micallef, *"Strain in Interdiffused $In_{0.53}Ga_{0.47}As/InP$ Quantum Wells"*, E. H. Li (editor), *Semiconductor Quantum Wells Intermixing*, Gordon and Breach (2000)

2. D. K. Sengupta, T. Horton, W. Fang, A. Curtis, J. Li, S. L. Chuang, H. Chen, M. Feng, and G. E. Stillman, Appl. Phys. Lett 70, 3573 (1997).

3. D. Sengupta, V. Jandhyala, S. Kim, W. Fang, J. Malin, P. Apostolakis, K.-C., Hsieh, Y.-C. Chang, S. L. Chuang, S. Bandara, S. Gunapala, M. Feng, E. Michielssen, and G. Stillman, IEEE J. Sel. Top. Quant. Electron. 4, 746 (1998).

4. G. Li, S. J. Chua, S. J. Xu, X. C. Wang, A. Saher Helmy, Mao-Long Ke, J. H. Marsh, Appl. Phys. Lett., 73, 3393 (1998).

5. Hitoshi Sumida, Hajime Asahi, S. Jae Yu, Kumiko Asami, Shun-ichi Gonda, and Hisao Tanoue, Appl. Phys. Lett. **54,** 520 (1989).

6. Huajie Chen, H. A. McKay, R. M. Feenstra, G. C. Aers, P. J. Poole, R. L. Williams, S. Charbonneau, P. G. Piva, T. W. Simpson and I.V. Mitchell, J. Appl. Phys. **89,** 4819(2001).

7. D. G. Deppe, N. Holonyak, Jr., W. E. Plano, V. M. Robbins,J. M. Dallesasse, K. C. Hsieh and J. E. Baker, J. Appl. Phys. **64,** 1838 (1988).

8. R. D. Goldberg, I. V. Mitchell, P. G. Piva, H. H. Tan, C. Jagadish, P. J. Poole, G. C. Aers, S. Charbonneau, G. C. Weatherly, M. B. Johnston, M. Gal, A. J. Springthorpe, H. Chen and R. M. Feenstra, *"Selective intermixing of ion irradiated semiconductor heterostructures"*, MRS Symposium Proceedings **540,** 15 (1998).

9. Huajie Chen, R. M. Feenstra, P. G. Piva, R. D. Goldberg, I. V. Mitchell, G. C. Aers, P. J. Poole, and S. Charbonneau., Appl. Phys. Lett. **75,** 79 (1999).

10. M. Paquette J. Beauvais, J. Beerens, P. J. Poole, S. Charbonneau, C. J. Miner, and C. Blaauw, Appl. Phys. Lett. **71**, 3749 (1997).

11. Gregory F. Redinbo, Harold G. Craighead, and J. Minghuang Hong, J. Appl. Phys. **74**, 3099 (1993).

12. U. G. Akano, I. V. Mitchell, F. R. Shepherd, and C. J. Miner, J. Vac. Sci. Technol. A, **10**, 996 (1992).

13. P.J. Poole, P. G. Piva, M. Buchanan, G. C. Aers, A. P. Roth, Z. R. Wasilewski, E.S. Koteles, S. Charbonneau, and J. Beauvais, Semicon. Sc. Tech.. **9**, 2134 (1994)

14. P. G. Piva, P. J. Poole, M. Buchanan, G. Champion, I. Templeton, G. C. Aers, R. Williams, Z. R. Wasilewski, E.S. Koteles, S. Charbonneau, Appl. Phys. Lett. **65**, 621 (1994)

15. J. Cibert, P. M. Petroff, D. J. Werder, S. J. Pearton, A. C. Gossard, J. H. English, Appl. Phys. Lett. **49**, 223 (1986)

16. P. G. Piva, P. J. Poole, S. Charbonneau, E. S. Koteles, M. Buchanan, G. Aers, A. P. Roth, Z. R. Wasilewski, J. Beauvais and R. D. Goldberg, Superlattices and Microstructures, **15**, 385 (1994).

17. D. R. Lide [Ed.], *'CRC Handbook of Chemistry and Physics'*, CRC Press, pp 9.129,12.88 (1992)

18. W. Wesch, E. Wendler, G. Götz, and N. P. Kekelidse, J. Appl. Phys. **65**, 519(1989).

19. K. Kash, B. Tell, P. Grabbe, E.A. Dobisz, H. G. Craighead and M. C. Tamargo, J. Appl. Phys., **63**, 190 (1988)

CHAPTER 8

Impurity Free Vacancy Disordering in InP/InGaAs Quantum Wells

8.1 Introduction

Apart from the implantation-induced interdiffusion already discussed in Chapter 7, impurity free vacancy disordering (IFVD) is another method available for tuning the emission and detection wavelengths of optoelectronic devices, and one which results in the lowest concentration of residual defects. In IFVD, defects caused by the presence of a dielectric layer on the surface of the sample migrate down to the quantum well region during annealing and thereby cause interdiffusion, as shown in Figure 8.1. The defects are generally understood to be created by interfacial reactions between the semiconductor and dielectric layer during annealing. The thermal stress created at annealing temperature, caused by differences in thermal expansion coefficients between the semiconductor and the dielectric, is also understood to modify the degree to which the various defects created in this way are able to diffuse. While this has been proposed as the principal cause of interdiffusion using this technique, it is not known whether the strain felt at the quantum well during annealing is sufficient to cause interdiffusion of the quantum well on its own, in the absence of interfacial reactions with the dielectric. In this case, the defects causing the interdiffusion could originate from dislocations at the quantum well/barrier interface which occur under strain, as well as grown-in defects which are never completely eliminated from epitaxial structures. Systematic investigations into such issues have yet to be pursued. Regardless of the exact mechanisms, it has generally been found that the quality of the photoluminescence from such interdiffused quantum wells compares very well to those from the original structures[1-3]. Thus it is a worthwhile technique to investigate for interdiffusion in InP/InGaAs quantum wells. The

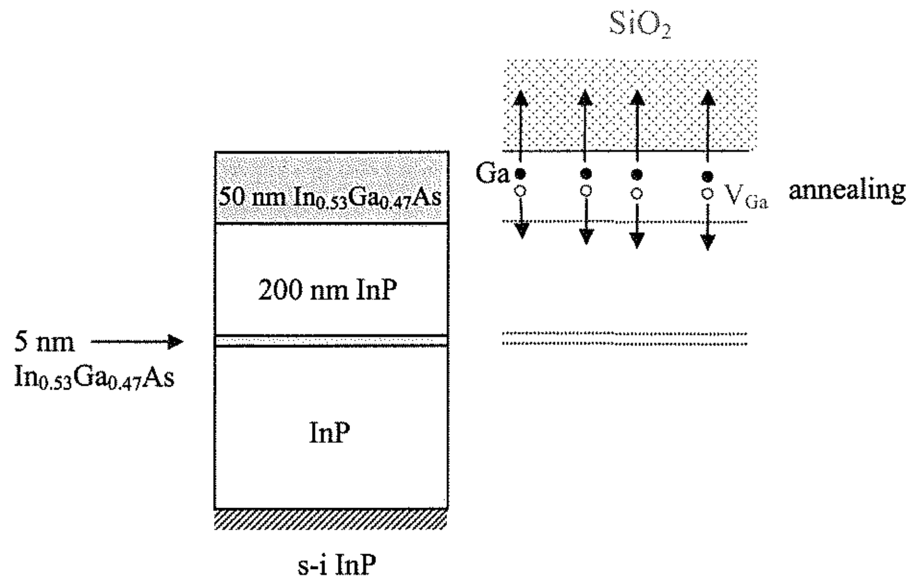

Figure 8.1 Schematic of interdiffusion induced by impurity free vacancy disordering. The example given shows how interfacial reactions between the capping layer and dielectric - resulting from the natural solubility of Ga in SiO_2 - allow for Ga atom migration into the oxide and a corresponding injection of Ga vacancies into the heterostructure. During annealing these vacancies can migrate down to the quantum well and promote interdiffusion.

issues relating to interdiffusion using this technique are similar to those already discussed in Chapter 7, however the results we have achieved here are vastly different, illustrating the extent to which InP/InGaAs interdiffusion can be tailored using different techniques.

Another consequence of different diffusion coefficients for the group III and group V sublattices is that after the interdiffusion process, the quantum well will no longer be lattice matched, causing strain to be introduced into the system. This can have important effects on the ultimate shape of the well potential profile[4,5]. Varying ratios of group V to group III diffusion have thus been predicted to result in different degrees of blueshifting of the original quantum well emission, and in some cases even redshifting, as illustrated in Figure 8.2. This Chapter discusses the role of silicon dioxide properties on interdiffusion in the InP/InGaAs quantum well structures, capped with InGaAs. We also investigate the effect of depositing dielectric single layers and bilayers, as illustrated in Figure 8.3, which deliberately introduce either compressive or tensile strain into the system. The single layer dielectrics consisted of SiO_2, SiN_x or TiO_2 deposited directly onto the samples. The bilayers used a sublayer of SiO_2, of varying thickness, and overlayers of either SiN_x or TiO_2. Finally, the effect of undoped or Ga-, P- or Ti- doped spin-on silica layers is studied. Interdiffusion was found to depend strongly on the capping layer as well as the type of dielectric deposited on the surface. Both the induced strain and interfacial reactions between the sample and the dielectric played a significant role in causing interdiffusion of the quantum wells.

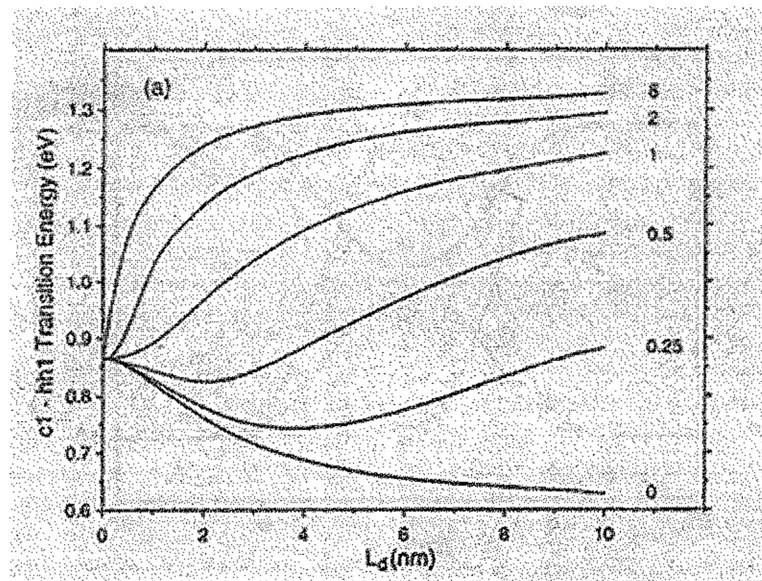

Figure 8.2 Simulations of ground state (electron-heavy hole) transition energy variation with interdiffusion for a 6 nm $In_{0.53}Ga_{0.47}As/InP$ quantum well, for various values of k = group V/group III diffusion rates. When k < 1 the interdiffusion rate on the group V sublattice is less than the interdiffusion rate on the group III sublattice, and vice versa. Taken from Micallef[4].

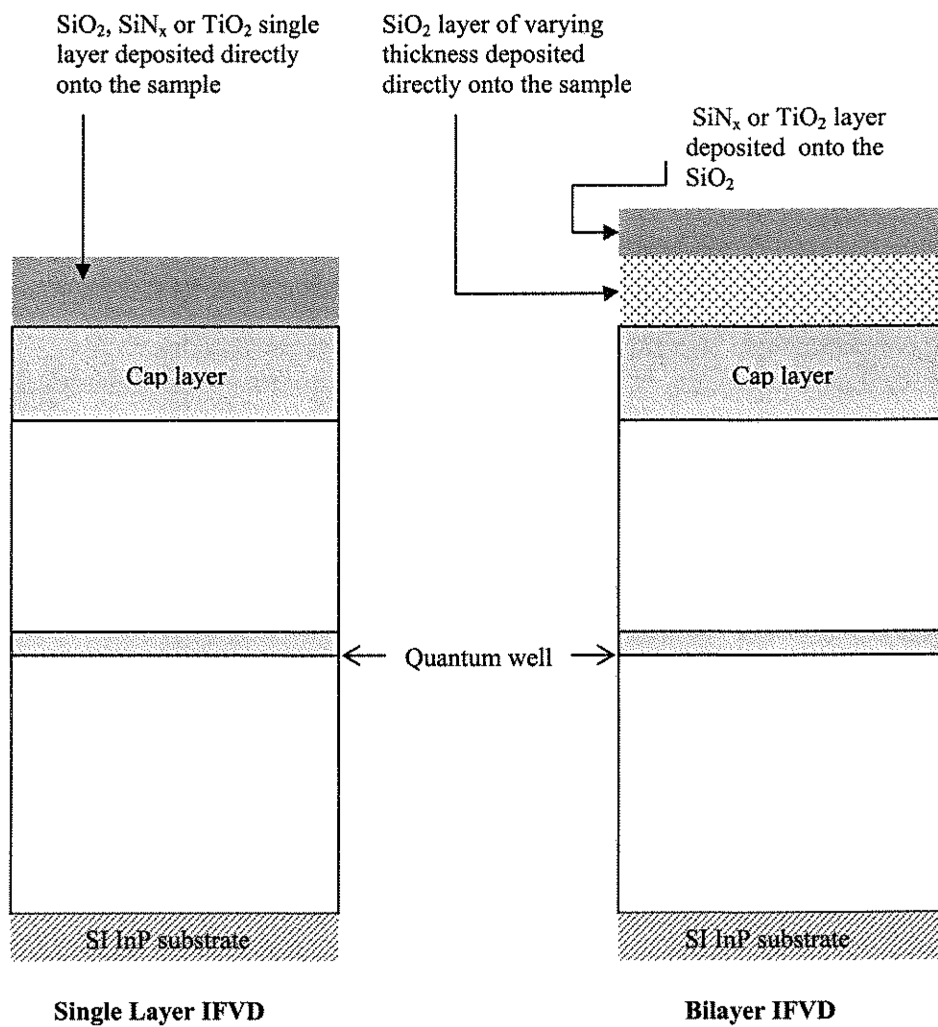

Figure 8.3 Schematic illustrating concepts for 'single layer' and 'bilayer' impurity free vacancy disordering.

8.2 Experimental

The InGaAs capped samples studied here were identical to those used in Chapter 7. For single layer dielectric studies, PECVD was used to deposit 200 nm of SiO_2 at room temperature and SiN_x at 300°C. The same thickness was used for deposition of TiO_2 single layers by electron beam evaporation. For dielectric bilayer studies, SiO_2 was deposited at room temperature to thicknesses of approximately 5, 14, 28 and 70 nm. 200 nm thick SiN_x or TiO_2 overlayers were then deposited using identical methods as for the single layer dielectric treatment. Studies using spin-on glasses (SOGs) were done with undoped, Ga-, P- or Ti- doped silica layers, which were deposited on the samples by spinning at 3000 rpm for 30 seconds, then baking at 300°C for 15 minutes.

The dielectrics of one half of the area of each sample were removed by etching with 10% HF solution, in order to create a reference. The samples were then annealed at 800°C for 60 seconds, with an InP proximity layer next to the substrate, and a GaAs proximity layer next to the InGaAs cap. Photoluminescence was performed at 77K using a red diode laser at 670 nm, and an InGaAs photodetector through a 0.5 m monochromator, in order to measure the shifts in quantum well emissions. The relative PL energy shifts were calculated from the difference between the emission energy of the dielectric coated side and that of the (annealed) reference side on the same sample.

XPS in-depth profiling (using a VG ESCALAB 220-iXL spectrometer with a monochromated Al Ka x-ray source, and sputtering with a 5 keV Ar ion beam) was also performed on the samples to investigate metallurgical reactions between the semiconductor elements and the dielectric.

8.3 SiO_2 Induced Interdiffusion

From the outset, interdiffusion in the InP/InGaAs quantum well system using the IFVD technique has revealed markedly different behaviour to the implantation induced disordering. Depositing a single layer of SiO_2 using PECVD on the InGaAs capped samples resulted in no interdiffusion when the samples were subsequently treated at the standard annealing temperature and time of 700°C for 60s used in Chapter 7. By annealing at 800°C for 60 s, a large shift of the emission wavelength (corresponding to an energy shift of some 85 meV), occurred on the oxide-coated side of the sample, as shown in Figure 8.4. The quality of the peak from the intermixed samples is also very good, indicating the high quality of the wafer as well as the low concentration of residual defects created by IFVD. The as-annealed side of the sample showed essentially no shift at all from the un-treated emission wavelength of ~1440 nm. In Chapter 7, the thermal shifts which occured in this sample for annealing at the same temperature were a result of cumulative anneals; the samples experienced four 60 second anneals (at 600, 650, 700 and 750°C) prior to annealing at 800°C, which resulted in the thermal shifts observed in Figure 7.5. The lack of thermal shifts observed here for a single anneal at 800°C therefore do not contradict the results described in Chapter 7.

Similar experiments were also tried on the InP capped quantum well structures used in Chapter 7, however no SiO_2 induced blueshifts were observed even for annealing temperatures higher than 800°C. This was a consistent result over several experiments, and following initial attempts to understand the reason for this, it was decided a thorough study was beyond the scope of this work. Therefore, studies on the InGaAs capped quantum well structures are pursued here. The IFVD behaviour of the InP capped samples remains an important topic for future work.

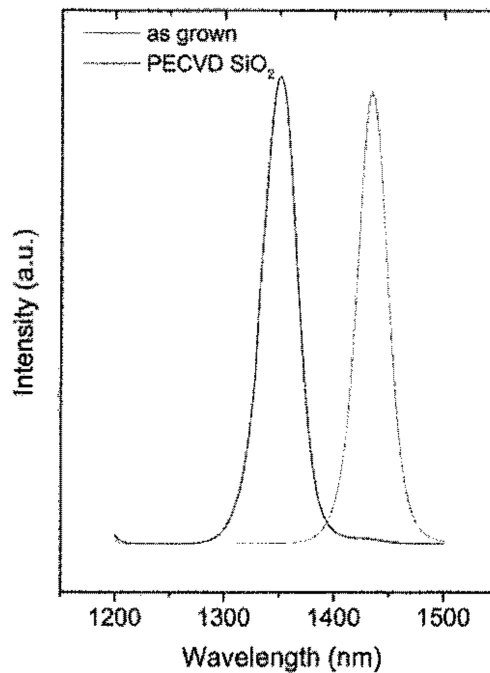

Figure 8.4 77K photoluminescence spectra of InGaAs capped InP/InGaAs quantum wells for PECVD of 60 nm SiO_2. RTA 800°C for 60 sec. PL spectra from annealed reference samples with no SiO_2 layer are also shown (no change was observed with respect to as-grown samples).

In previous work on GaAs/AlGaAs or GaAs/InGaAs quantum well systems, the combination of a GaAs capping layer and a SiO_2 layer resulted in the injection of Ga atoms into the oxide, providing Ga vacancies to drive interdiffusion[6-8]. In these systems, diffusion was only possible on the group III sublattice, and annealing temperatures of at least 850°C were required to induce interdiffusion of the quantum wells. In the samples used here, we can also assume an interaction of Ga atoms with the oxide (and through XPS measurements shown later we have proof of this). It will also be shown at the end of this Chapter that surface In also oxidizes and migrates through the SiO_2. In the same experiments, very little As-O or P-O was detected in the oxide, indicating that the solubility of the group V elements in

SiO_2 is much less. Thus, group III elements have a strong tendency to move up into the dielectric and form oxides. These metallurgical reactions occurring between the semiconductor and dielectric must therefore play a role in causing interdiffusion in this quantum well system.

The presence of the oxide on the sample during annealing has another effect: at temperature the smaller expansion coefficient of SiO_2 with respect to InP or InGaAs will mean that the sample will experience compressive strain. The respective thermal expansion coefficients have been listed in Table 8.1 (see p178). Two main effects resulting from this compressive strain need to be considered: the known favourable conditions for vacancy migration under compressive strain[9,10], and in group V/III - mobile systems, the favourable conditions for interdiffusion on the group V sublattice. The former effect is simply due to the fact that the presence of a vacancy in the lattice causes localized tensile strain, and hence migration of this type of point defect is energetically favoured under conditions of compressive strain. We already have strong evidence that group III vacancies are being created in the capping layer, and now the compressive strain being created at annealing temperature is conducive to these vacancies moving around in the sample.

On the other hand, the SiO_2-induced compressive strain is also conducive to interdiffusion on the group V sublattice. This can be understood in the following way: assuming that interdiffusion will occur during annealing in order to minimise the compressive strain at the quantum well, the lattice constant of the InGaAs needs to be reduced (and that of the barriers increased). This can be achieved by increasing the P content in the quantum well and the As content in the barriers. A transition from InGaAs to InGaAsP in the quantum well represents a change to larger bandgaps, hence a blueshifting of the emission wavelength. Thus, at the quantum well, the compressive strain creates a strong driving force for group V interdiffusion.

Deenapanray *et al.*[11] with reference to silica treatment of epitaxial GaAs samples, noted that in addition to the formation of V_{Ga}, the compressive stress caused by the silica was conducive to the formation of As interstitials, and as a consequence As_{Ga} ($V_{Ga} + As_i \rightarrow As_{Ga}$) formation was also favoured. While there is no possibility for group V interdiffusion in GaAs based quantum well systems, these findings show how the formation of V_{Ga} at the SiO_2/InGaAs interface can lead to interdiffusion on the group V as well as group III sublattice.

Thus, the SiO_2-induced compressive strain and interfacial SiO_2/InGaAs reactions create opportunities for both group III and group V diffusion. As has been mentioned in the introduction, this is a common feature of the InP - based quantum well systems. The question which remains is whether diffusion on one or the other sublattice is dominant, or whether they are both equal. As mentioned in the introduction, unequal diffusion of group III and group V elements will cause its own strain at the quantum well. Thus, by inducing strain during annealing via the presence of a dielectric layer, conditions could be created which are energetically favourable for unequal interdiffusion on the group III and group V sublattices.

Knowing that Ga will diffuse into the SiO_2 would seem to support the predominance of group III interdiffusion in the InP/InGaAs system, however this would be inconsistent with computational studies by Micallef[4], Li[5] and Bollet *et al.*[12] as well as the extensive literature on Zn induced interdiffusion in InP/InGaAs quantum well structures[13-16]. Such work indicates that group III interdiffusion in the InP/InGaAs system is associated with a redshifting of the photoluminescence, while blueshifting results when the ratio, k, of group V to group III diffusion coefficients is greater than or equal to unity. The large blueshift shown in Figure 8.4 would seem to support a dominant group V interdiffusion. Moreover, higher annealing temperatures were required to initiate group III interdiffusion in GaAs based quantum well

systems than were used here. During annealing, (in addition to the natural Ga and In solubility in the oxide) the in-plane compressive strain felt in the semiconductor structure will cause Ga and In atoms to diffuse into the SiO_2, providing group III vacancies which migrate into the quantum well region. This initial group III interdiffusion, if it penetrates far enough into the sample, may have a potential to increase the In content in the quantum well. Increasing the In content will increase the lattice constant of the InGaAs with respect to the InP barriers, thus causing the quantum well to be under additional in-plane compressive strain. Thus, we propose that, while it is highly likely that group III vacancy injection is occurring in this system, the competing group V interdiffusion is the energetically favoured process, leading to the large blueshift observed in Figure 8.4.

Summary

Blueshifting of InGaAs capped samples coated with SiO_2 was very large. Ga and In uptake into the SiO_2 was considered as an important group III diffusion mechanism, although the large blueshifts supported a dominant group V diffusion process (brought on by compressive strain and facilitated by reactions with group III vacancies, leading to antisite and interstitial formation).

8.4 SiO_2, SiN_x or TiO_2 Single Layer Induced Interdiffusion

If strain is playing an important role in driving the interdiffusion in this system, it follows that inducing different types of strain into the system will result in different degrees of blueshifting. We can test this idea by applying surface treatments that have different thermal expansion coefficients. Table 8.1 shows the thermal expansion coefficients for InGaAs, InP, GaAs, SiO_2,

SiN_x and TiO_2. SiO_2 and SiN_x have smaller thermal expansion coefficients than the semiconductors, while TiO_2 has a larger coefficient. By depositing these materials onto the samples and annealing, we can create both tensile and compressive strain in the system. Table 8.2 shows the blueshifting that was induced in the samples when treated with SiO_2, SiN_x or TiO_2 single layers 200 nm thick, after annealing at 800°C for 60s. The as-annealed peak was always located at approximately 1440 nm, which is also the emission wavelength of an untreated sample. This serves to illustrate the remarkable consistency of the as-annealed peak emission from sample to sample, and indicates the high quality of the wafer that has been used

Material	Thermal expansion coefficient (x 10^{-6} °C^{-1})
SiO_2	0.52
SiN_x	2.8
InGaAs	5.25
InP	4.56
GaAs	6.86
TiO_2	8.19

Table 8.1 Thermal expansion coefficents for InGaAs, InP and GaAs and various dielectrics[17].

Dielectric	InGaAs cap (meV)
SiO_2	85
SiN_x	12
TiO_2	25

Table 8.2 . Photoluminescence energy shifts (in meV) for 200 nm PECVD deposited SiO_2, SiN_x and TiO_2 single layers on InGaAs quantum well samples after annealing at 800°Cfor 60 seconds.

in these experiments. Thus, the peak shifts listed in Table 8.2 are due solely to the dielectric layers, since there is minimal thermal interdiffusion.

Intermixing occurs more readily when the sample is treated with SiO_2 as compared to SiN_x. As a single layer, the SiN_x causes a small amount of blueshifting in the InGaAs capped sample. The small amount of shifting could well be due to the incorporation of O and H into the SiN_x during deposition (a commonly reported issue with regard to PECVD of SiN_x layers), which would then allow a small amount of Ga or In diffusion into the nitride, since it is known that during PECVD of SiN_x it is very hard to remove oxygen competely. Otherwise, the compressive strain conditions, and the resulting mechanisms already described, are exactly the same as for SiO_2, the only differences being a smaller degree of compressive strain and less oxygen (if any) for group III elements to react with. Assuming strain and/or interfacial reactions are the only causes for interdiffusion, it follows that the amount of blueshifting observed would be less than for SiO_2. It should also be mentioned that the importance of the interfacial reactions is not known. It may be that the compressive strain at the quantum well is sufficient to induce interdiffusion on its own, or it may be that the interfacial reactions are *necessary* for defect injection which then kick-starts the whole interdiffusion mechanism.

Li *et al.*[17] reported larger blueshifts for InGaAs capped InGaAs/InGaAsP quantum wells when they were coated with SiN_x than when they were coated with SiO_2, whereas Yu *et al.*[19] and Lee *et al.*[20] found results similar to those reported in Table 8.2, with greater blueshifts occurring for SiO_2 deposition. Different deposition conditions resulting in different quality dielectrics may be responsible for these varied results. The role of the quality of the dielectric (porosity and so on) on interdiffusion in InP based quantum well systems needs to be more thoroughly investigated.

The larger thermal expansion coefficient of TiO_2 as compared to InP or InGaAs means that tensile biaxial strain would be felt at the quantum well during annealing in the TiO_2 treated samples. XPS experiments done on TiO_2 treated GaAs and InP surfaces (not shown) have also shown Ga- or In- oxide, respectively, throughout the dielectric. These reactions are similar to the case for SiO_2 treatment, although the degree of blueshifting shown for the TiO_2 case in Table 8.2 is much less. If compressive strain provides favourable conditions for vacancy diffusion, tensile strain will suppress it. Thus it would be expected that the presence of TiO_2 on the sample surface is not conducive to group III vacancy migration throughout the sample, even these vacancies may be created in the cap layer as a result of oxidation of surface In and Ga atoms[21].

During annealing, the TiO_2 induced in-plane tensile strain felt at the quantum well can be counteracted by an increase of lattice constant in the InGaAs quantum well, which is achieved by increasing the In content. A larger In concentration will reduce the bandgap of InGaAs and thus the effective bandgap of the quantum well, creating the potential for a redshift of the emission wavelength. A redshift was not observed, however. Micallef[4] has shown that for the case of dominant group III interdiffusion where the group V interdiffusion is nonzero, both blueshifting and redshifting of the peak emission can occur, depending on the extent of interdiffusion. A large amount of interdiffusion will create an increase in the c1-hh1 transition energy (blueshift), while a redshift is obtained for lesser amounts of interdiffusion. This has been illustrated in the simulations of Figure 8.2 above, where in a 6 nm InGaAs/InP quantum well, for example, for k = group V/group III = 0.5 (dominant group III interdiffusion), the c1 – hh1 transition energy increases (blueshift) for a diffusion length, L_d, $>$ 4 nm, and decreases (redshift) for $L_d < 4$ nm. In the case of our experiment, if the effect of

the TiO_2 felt by the semiconductor is very strong (due to the large thermal stress), then a large amount of interdiffusion and thus slight blueshifting would be expected.

Summary

The separate but equally significant effects of chemical interactions between the capping layer and dielectric, and of strain induced by different thermal expansion coefficients during annealing, have produced some intriguing results. The greatest amount of interdiffusion was seen in the SiO_2 deposition case. In the case of SiN_x treatment, Ga or In migration into the nitride has probably also occurred due to the unavoidable presence of oxygen in the dielectric, and along with a smaller induced compressive strain during annealing, has resulted in a blueshifting, albeit not as extensive as for the SiO_2 case. SiO_2 and SiN_x, both having smaller thermal expansion coefficients than InP or InGaAs, would have caused compressive biaxial strain in the samples during annealing, creating favourable conditions for group V dominant interdiffusion. The TiO_2, having a larger thermal expansion coefficient than the InP or InGaAs, has induced tensile biaxial strain which is conducive to group III dominant interdiffusion.

8.5 SiO_2- and SiN_x or TiO_2 Bilayer Induced Interdiffusion

Single layer dielectric deposition has resulted in some intruiging responses from the samples to different types of strain. To explore this effect further, bilayer dielectric treatments were employed. It has already been shown that by depositing a layer of SiN_x on top of layers of SiO_2 of different thicknesses, which in turn have been deposited on InGaAs/GaAs quantum well systems, the SiN_x will suppress the intermixing induced by the Ga diffusion into

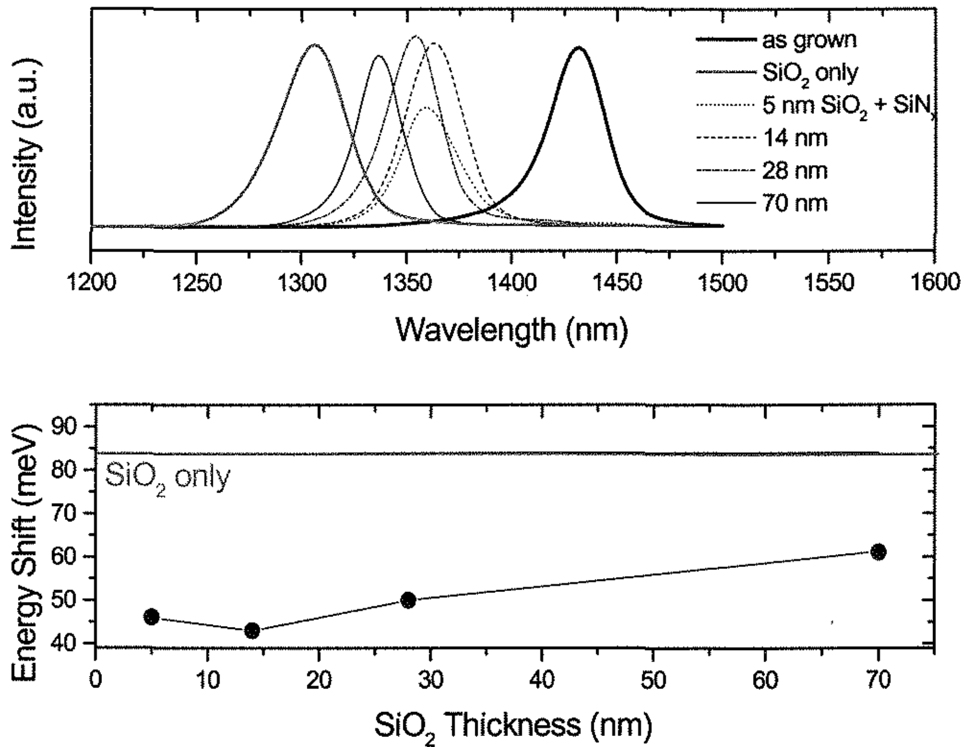

Figure 8.5 Photoluminescence shifts as a result of SiO_2/SiN_x bilayer dielectric treatment of the InGaAs capped InP/InGaAs quantum wells, with the SiO_2 thickness varying between 5 and 70 nm and an overlayer thickness of ~200 nm, after annealing at 800°C for 60s. a) Photoluminescence spectra at 77K, b) Energy shifts as a function of SiO_2 thickness.

the SiO_2, and that the degree of suppression decreases as the thicknesss of the SiO_2 increases[10,22]. We note from Table 8.1 that the thermal expansion coefficent of SiN_x is greater than that of SiO_2 but still less than that of InGaAs and InP. We have chosen to repeat this technique to see if it has an effect on the intermixing of the InP/InGaAs system, which is proving to be highly susceptible to strain. We have tried it with a TiO_2 overlayer as well, which has a thermal expansion coefficient larger than that of InGaAs and InP.

Figure 8.5 shows the photoluminescence spectra and energy shifts as a function of SiO_2 thickness, from the InGaAs capped quantum well samples that have been coated with the SiO_2/SiN_x dielectric bilayers. Positive energy shifts correspond to a blueshift in photoluminescence with respect to the as-annealed emission. The shifts due to SiO_2 only deposition, depicted by the thick grey line, remain constant (within experimental error) regardless of the SiO_2 thickness. Figure 8.5 (a) shows behaviour that is consistent with the experiments done on AlGaAs/GaAs systems[23]. The SiN_x is suppressing the degree of intermixing, with the thinnest SiO_2 layers yielding the smallest blue shift in the photoluminescence peak with respect to the as-annealed sample. As the SiO_2 layer becomes thicker, the effect of the SiO_2/InGaAs strain induced by the SiN_x overlayer is diminished, and the peak emission is increasingly blueshifted.

When comparing the expansion coefficients of SiN_x, SiO_2, InGaAs and InP, we see that the SiN_x overlayer will be reducing the amount of biaxial compressive strain in the semiconductor caused by the SiO_2. Thus the amount of strain felt at the quantum well will be less, resulting in a smaller amount of intermixing and reduced blueshifting. As the SiO_2 thickness is increased, thereby increasing the compressive strain, the blueshifting increases.

Figure 8.6 shows the effect of the SiO_2/TiO_2 bilayers. The larger thermal expansion coefficent of the TiO_2 when compared to InP and InGaAs has had a novel effect on the intermixing behaviour of this system. Not only does this overlayer suppress the blueshifting associated with SiO_2-only treatment of the sample, at a SiO_2 sublayer thickness of ~28 nm, there is actually a significant *redshift* (negative energy shift) of about 60 nm. This experiment has provided a way of varying the degree of intermixing by varying the strain, and thus we are able to probe different stages of the group III dominant intermixing as proposed by Micallef and Bollet *et al.*[4,12] (see Figure 8.2).

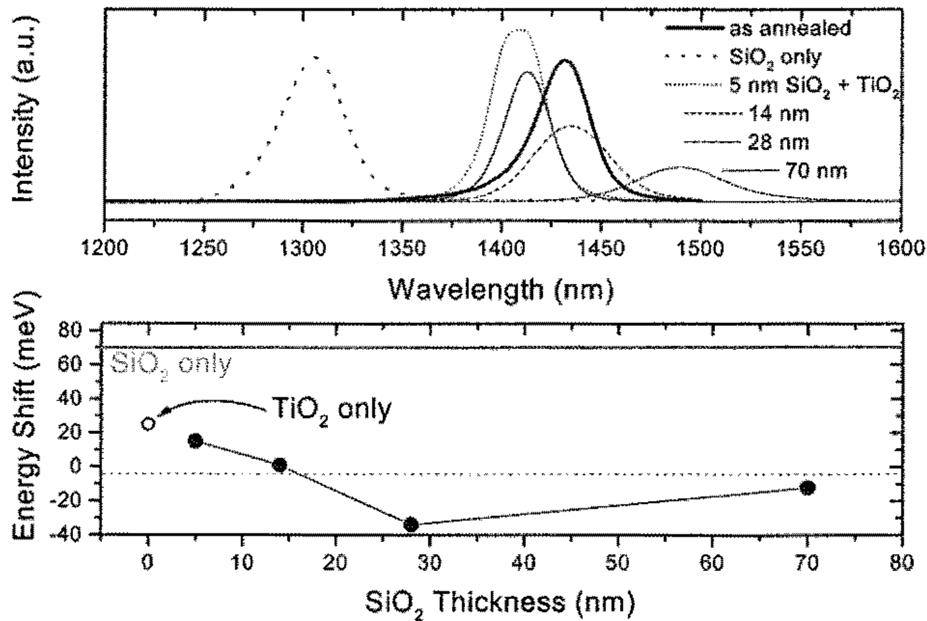

Figure 8.6 Photoluminescence shifts as a result of SiO_2/TiO_2 bilayer treatment of InGaAs capped InP/InGaAs quantum wells, with the SiO_2 thickness varying between 5 and 70 nm and an overlayer thickness of ~200 nm, after annealing at 800°C for 60s. a) Photoluminescence spectra at 77K, b) Energy shifts as a function of SiO_2 thickness.

The result of TiO_2 deposition in the absence of SiO_2 discussed in the previous section is shown by the open circle in Figure 8.6 (b). The blueshift of 25 meV for TiO_2 deposition is slightly more than for the SiO_2/TiO_2 case where the sublayer is thinnest, although less than the ~70 meV induced by SiO_2 only deposition.

As mentioned earlier, regarding simulations such as by Micallef *et al.*, group III dominant interdiffusion, such as is favoured by tensile strain, is able to produce both redshifting and blueshifting. When there is a large amount of dominant group III interdiffusion, a small amount of blueshifting is expected. When this diffusion is to a lesser extent, redshifting of the emission wavelength is possible. For the thinnest SiO_2 sublayers, the

effect of the TiO_2 felt by the semiconductor is very strong, which would correspond to a large amount of interdiffusion and thus some blueshifting. As the sublayer thickness is increased and the effect of the TiO_2 is reduced, the amount of interdiffusion decreases. The peak emission shifts further to the red end of the spectrum, reaching a maximum the 28 nm sublayer case. As the sublayer thickness is increased further, the peak shifts back towards the SiO_2-only peak, presumably because the strain caused by the SiO_2 sublayer has begun to compete with the strain caused by the TiO_2 overlayer.

Summary

Using a bilayer dielectric treatment, it was possible to see how varying the amount of strain experienced by the quantum well during annealing changed the interdiffusion. SiN_x/SiO_2 treatment of the InGaAs capped sample resulted in reduced blueshifting as the strain was decreased. TiO_2/SiO_2 treatment allowed a thorough probing of the group III dominant interdiffusion by varying the thickness of the SiO_2, and at certain thicknesses a redshift in the quantum well emission was observed. Such an evolution of blueshifting to redshifting is consistent with modeling of the group III dominant process done by Micallef and Bollet *et al.*[4,12]

8.6 Spin-on Glass Induced Interdiffusion

Spin-on glasses provide yet another way of inducing IFVD. They are also easily obtainable with various doping elements, which, in the case of this work, is useful for testing various theories about which elements are diffusing into the dielectrics. SOGs provide a very simple and cost effective means for inducing interdiffusion. Moreover, there are fewer deposition

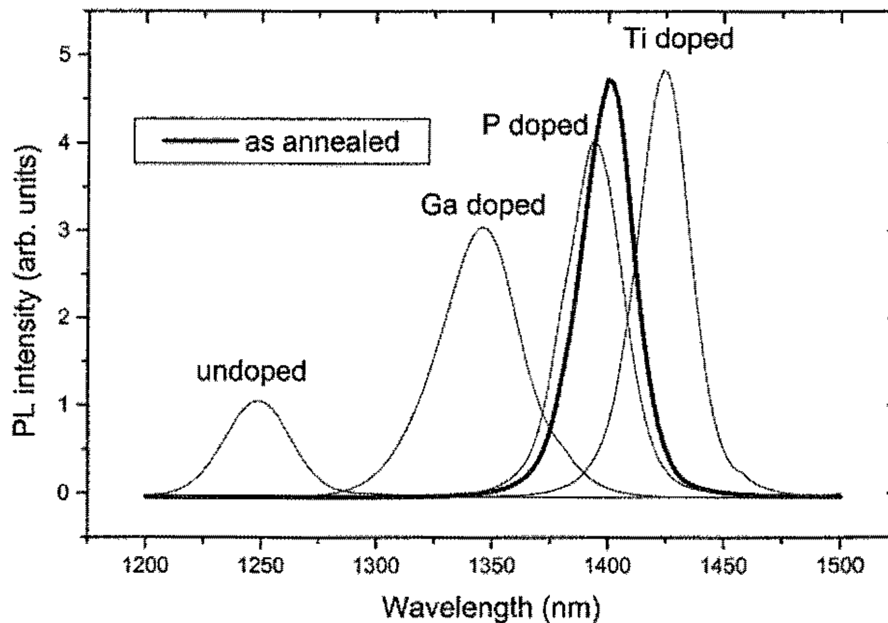

Figure 8.7 Photoluminescence shifts of InGaAs capped InP/InGaAs quantum wells coated with an undoped, Ga-, P- or T- doped spin-on glasses, baked at 300°C for 15 minutes and then annealed at 800°C for 60s.

parameters involved using this form of silica treatment (as compared to PECVD deposition). In the previous sections we varied the amount of strain induced into the samples, whereas here the importance of interfacial reactions can be studied. In similar experiments on GaAs/AlGaAs quantum well systems, Fu *et al.* found that, as proof of the concept that Ga atoms were diffusing into the SiO_2 to promote interdiffusion, deposition of Ga-doped spin-on silica glasses resulted in a decreased amount of blueshifting[24]. In the same work, it was found that undoped and P- doped SOGs produced similar interdiffusion.

Figure 8.7 shows the quantum well emissions resulting from undoped, Ga-, P- or Ti-doped silica deposition on the InGaAs capped InP/InGaAs structure, post annealing at 800°C for 60s. Unlike the experiments done with PECVD deposited dielectrics, the as-annealed emission has shifted slightly from the un-treated value of ~1440 nm, to ~1400 nm. While annealing at 800°C is not expected to induce significant intermixing in the InGaAs capped

samples (as was consistently the case in the previous sections), the combination of this step and the prior 300°C baking for 15 minutes used to set the silica films has produced this thermal shift in the peak emission. The spun-on silica has caused blueshifting in addition to this thermal shift. The undoped SOG results in a shift to ~1250 nm, which is larger even than that for the PECVD deposited SiO_2, although the peak has broadened and has a decreased intensity with respect to that of the as-annealed sample. Ga doping has produced a suppression of this blueshifting, with suppression from the P doped SOG even more significant. The peak resulting from treatment with the Ti doped SOG has caused a redshifting with respect to the as-annealed peak, back to ~1440 nm. Alternatively this can be seen as a total suppression of interdiffusion, even thermal diffusion, such that the peak emission does not shift at all from the untreated value. It is worth mentioning that doped SOGs have also been used as sources of dopants for Si - based devices, however the annealing temperatures used are typically greater than 1000°C and the times are much longer than 60s. Hence, while there is a small possibility of injection of Ga, P or Ti into the samples from the respective doped SOGs, the annealing conditions used in this study make it likely that such an effect is negligible.

The results of XPS in-depth profiling done on the sample treated with the undoped SOG after annealing at 800°C are shown in Figure 8.8. The region of increased Ga and As signals for Ar ion sputtering (etching) between ~250 - 350 seconds corresponds to the 50 nm InGaAs capping layer. For etching times beyond this, signals are being collected from the InP barrier. The slight increase of Ga and As signals at an etching time of ~470 seconds corresponds to the 5 nm quantum well. Because the sputtering rate was quite fast, this very thin InGaAs layer does not show up clearly through the dominant InP signals. Both O and Si are injected into the sample, right through the capping layer, with oxygen penetrating deeper

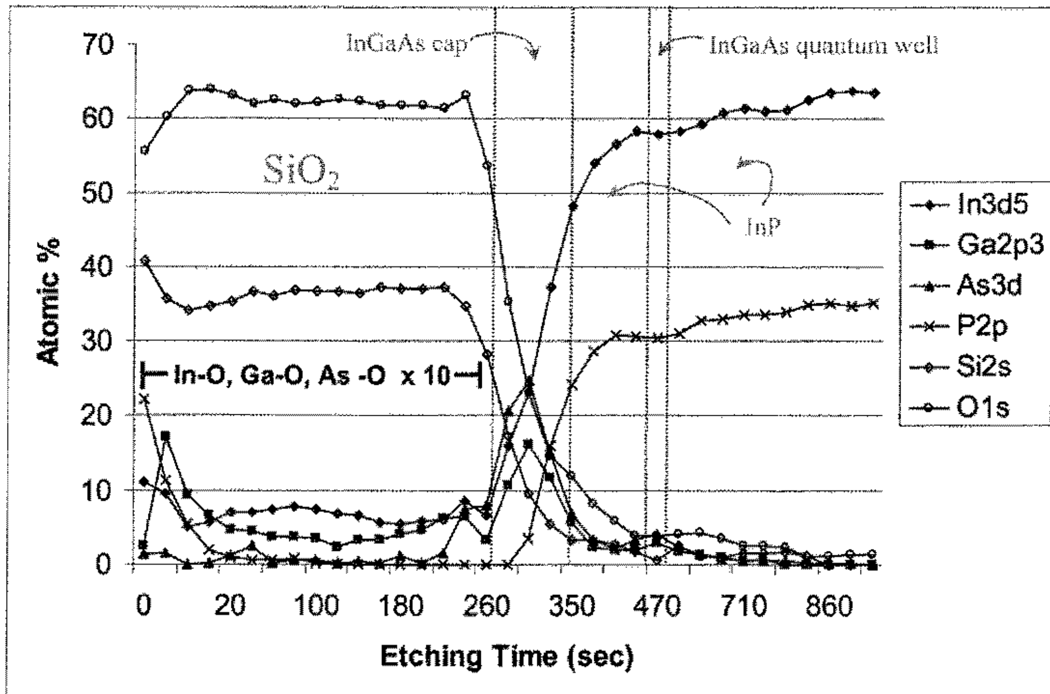

Figure 8.8 XPS in-depth profiles of InGaAs capped InP/InGaAs quantum wells treated with an undoped SOG, baked at 300°C for 15 minutes and then annealed at 800°C for 60s. In-O, Ga-O, As-O signals within the silica have been magnified 10 x.

than Si. A similar penetration of Si and O signals into the semiconductor has also been observed in XPS profiling of samples treated with PECVD SiO_2 (not shown). In-oxide and Ga-oxide are present from the surface of the dielectric, through whole silica layer down to the InGaAs cap. As-oxide is seen at the interface of SiO_2/InGaAs (the In, Ga and As oxide signals have been magnified in the figure). At certain depths, Ga-As signals are seen together with P signals, pointing to interdiffusion between the InGaAs cap and InP barrier. However, it is not clear how deep this interdiffusion might be, since the kinetic energy of P 2p is relatively high, causing the penetration depth of such a signal to be relatively high. A large P signal is seen at the surface of the silica, however this was not a P-O signal; thus it has been disregarded as a result of contamination during the experimental process.

There are three features to the interdiffusion caused by treatment with the undoped silica: the penetration of Ga, In and also As into the silica, and the significant P presence in the InGaAs capping layer. The Ga and In injection into the oxide is as expected, and hence Ga doped SOG treatment results in a decreased blueshifting since the driving force for the Ga to diffuse from the InGaAs to the oxide is reduced. The presence of P in the InGaAs, and the migration of As to the surface and its penetration into the oxide is definitive proof that the silica treatment is allowing for group V intermixing (this can also be applied to PECVD SiO_2 treated samples discussed in the previous section). The As presence in the oxide is particularly interesting, since this was not found in the case of (PECVD) SiO_2 treated GaAs capped GaAs/AlGaAs quantum well structures. Perhaps, in the case of this quantum well system, the strong group V interdiffusion mechanism has caused the As to migrate into the silica. While P has migrated into the capping layer, there is a strong decrease in the P content near the interface with the silica.

It is interesting to note that, in the GaAs/AlGaAs quantum well system, the P - doped SOG produced similar blueshifts to that of the undoped SOG, while in the case of the InGaAs/InP quantum well system, strong suppression of interdiffusion has occurred with the deposition of P - doped SOG. The latter finding indicates the important role played by group V interdiffusion in this system, although exact reason for this result is not yet clear.

Finally, the Ti doped SOG may be producing this strong suppression of interdiffusion because of a change in thermal expansion coefficient resulting from the presence of Ti in the silica. Since after baking, Ti- doped silica would become a combination of TiO_2 and silica, it is reasonable to assume that the resultant effect on intermixing is similar to the TiO_2/SiO_2 bilayer case. At this stage, the role of dopants on the thermal expansion coefficients of silica films is not known. However, a plausible explanation for the suppression of blueshifting could be

found in a combination of group III and group V interdiffusion which results in no variation of the peak emission wavelength from the as-grown value. Further work is necessary to understand the mechanisms responsible for the suppression caused by P- and Ti- doping of the spin-on glass. It may be that Ti-doped spin-on glasses could be used to enhance the thermal stability of InP/InGaAs quantum well systems.

8.7 Conclusion

Interdiffusion in InP/InGaAs quantum wells capped with InGaAs using the IFVD technique has provided very surprising results. The system has shown itself to be highly versatile, with different dielectric treatments and capping layers apparently drawing out different degrees of interdiffusion on the group III and group V sublattices. The system is also highly susceptible to strain. Variation in both the doping of silica films as well as strain induced during annealing were able to greatly modify the emission wavelengths.

In addition to the expected Ga diffusion into SiO_2, In atoms also show a strong tendency to react with O. Large blueshifts were achieved by depositing SiO_2 on InGaAs capped samples and annealing at 800°C for 60 seconds. The explanation for this behaviour was that, while group III reactions with the oxide may provide a kick-start mechanism for interdiffusion, the compressive in-plane strain felt at the quantum well during annealing is conducive to dominant diffusion on the group V sublattice.

SiN_x treatment produced smaller blueshifts than SiO_2 treatment of the samples. This was explained by a reduced compressive strain and a lesser degree of interfacial reactions between the dielectric and InGaAs cap.

TiO_2, with its larger thermal expansion coefficient than the semiconductors, causes tensile in-plane strain at the quantum well during annealing. This is conducive to

interdiffusion on the group III sublattice. According to simulations, a large degree of group III dominant interdiffusion (caused by a large amount of tensile strain) results in a small amount of blueshifting.

SiN_x/SiO_2 dielectric bilayer treatment of InGaAs capped samples yielded behaviour consistent with similar experiments done on InGaAs/GaAs quantum wells. The SiN_x, with its smaller thermal expansion coefficient than SiO_2 (although still larger than that for InP or InGaAs) acts to reduce the amount of strain caused by the SiO_2. Thus, the degree of blueshifting is less than for SiO_2 only deposition. If the thickness of the underlying SiO_2 is varied, this reduction of blueshifting is strongest (weakest) when the SiO_2 is thinnest (thickest).

TiO_2/SiO_2 bilayer dielectric deposition onto the InGaAs capped samples, with the competing combination of tensile in-plane strain caused by the larger thermal expansion coefficient of the TiO_2 and compressive in-plane strain caused by the SiO_2, has produced the most interesting results. In some cases, the peak emission was *redshifted* from the untreated value, from ~1440 nm to ~1500 nm. These results were explained by the varying degrees of group III dominant interdiffusion caused by changing the proximity of the TiO_2 to the quantum well (which was achieved by changing the thickness of the underlying SiO_2). Depending on the extent to which the group III dominant interdiffusion progresses, either a blueshift or a redshift in peak emission has been predicted (as shown in Figure 8.2)

Undoped spin-on glass treatment of the InGaAs capped samples resulted in the largest blueshifting, from ~1400 nm to ~1250 nm. Doping the SOG with Ga produced a reduction in blueshifting, which could be explained by the reduced Ga uptake from the semiconductor. This would seem to indicate that the group III reactions with the oxide do still play an important role, and compete with the role played by strain in determining the degree and type of interdiffusion in the quantum well. P- doping of the SOG suppressed the blueshifting even

further, which is interesting given the indications that P appears to have very low solubility in the silica. It was shown that As-O bonding does occur, however. The strength of the suppression of blueshifting in the case of P- doped SOG treatment is further evidence of the importance of group V interdiffusion. Ti doping of the SOG produced an even stronger suppression of blueshifting, which may be due to a different thermal expansion coefficient which is causing the silica to behave like TiO_2.

Suggestions for further work

Many questions remain unanswered with respect to the exact mechanisms responsible for interdiffusion in systems where mixing of elements can occur on both the group III as well as group V sublattices. Interdiffusion using the impurity free vacancy disordering technique seems to be the most direct probe of the issues relating to this. To test the ideas presented in this Chapter regarding the dominance of group V interdiffusion, similar experiments could be done on structures where the possibility of group III interdiffusion is removed. For example, InGaAs/InGaAsP quantum well structures could be used, with the In and Ga compositions held at the same value in both materials. It may also be interesting to compare GaAs and GaP interactions with SiO_2. Another question is whether In and Ga reactions with O in SiO_2 or TiO_2 occur with equal likelihood. As far as spin-on glass deposition, similar experiments could be tried using InP/InGaAs with InGaP capping layers to see if the effect of P-doping is any stronger. Since doping of this silica (as opposed to varying porosity) did seem to have an effect on the degree of interdiffusion achieved, it may also be interesting to try interdiffusion using deposition of Ga_2O_3 (and oxides of the other constituent elements in the sample).

References

1. A. C. Bryce, F. Camacho, P. Cusumano, and J. H Marsh, IEEE J. Sel. Top. Quantum Electron. **3**, 885 (1997)
2. J. H. Marsh, P. Cusumano, A. C. Bryce, B. S. Ooi, and S. G. Ayling, Proc. SPIE 74, 2401 (1995)
3. S. S. Si, D. H. Yeo, K. H. Yoon, and S. J. Kim, IEEE J. Sel. Top. Quantum Electron. **4**, 619 (1998)
4. J. Micallef, *"Strain in Interdiffused $In_{0.53}Ga_{0.47}As/InP$ Quantum Wells"*, E. H. Li (editor), *Semiconductor Quantum Wells Intermixing*, Gordon and Breach (2000)
5. G. Li, IEEE J. Quantum Electron. **34**, 982(1998)
6. P. N. K. Deenapanray, H. H. Tan, L. Fu and C. Jagadish, Electrochem. And Solid State Lett. **3**, 196 (2000)
7. L. Fu, P. N. K. Deenapanray, H. H. Tan, C. Jagadish, L. V. Dao, and M. Gal. Appl. Phys. Lett., **76**, 837 (2000)
8. Jae Su Yu, Jin Dong Song, Yong Tak Lee and H Lim, J. Appl. Phys. **91**, 4256 (2002)
9. A. Pépin, C. Vieu, M. Schneider, R. Planel, J. Bloch, G. Ben Assayag, H. Launois, J.Y. Marzin, and Y. Nissim Appl. Phys. Lett. **69**, 61 (1996)
10. M. K. Lee, J. D. Song, J. S. Yu, T. W. Kim, H. Lim, Y.T. Lee, Appl. Phys. A. **73**, 357 (2001)
11. P. N. K. Deenapanray, B. Gong, R. N. Lamb, A. Martin, L. Fu, H. H. Tan, and C. Jagadish, Appl. Phys. Lett. **80**, 4351 (2002)
12. F. Bollet, W. P. Gillin, M. Hopkinson, and R. Gwilliam, J. Appl. Phys., **93**, 3881(2003)

13. G. J. van Gurp, W. M. Van de Wijgert, G. M. Fontijn, and P. J. A. Thijs, J. Appl. Phys. **67**, 2919 (1990)

14. K. Nakashima, Y. Kawaguchi, Y. Kawamura, Y. Imamura, H. Asahi, Appl. Phys. Lett. **52**, 1051 (1988)

15. I. J. Pape, P. Li Kam Wa, J. P. R. David, P. A. Claxton, P. N. Robson, D. Sykes, Electron. Lett. **24**, 910 (1988)

16. S. A. Schwartz, P. Mei, T. Venkatesan, R. Bhat, D. M. Hwang, C. L. Schwartz, M. Koza, L. Nazar, B. J. Skromme, Appl. Phys. Lett. **53**, 1051 (1988)

17. D. R. Lide [Ed.], *CRC Handbook of Chemistry and Physics*, CRC Press, 12.78 (1992); G. V Samsonov [Ed.], tr. from Russian by C. N. Turton and T. I. Turton, *The Oxide Handbook*, IFI/Plenum, NY (1973)

18. H. T. Yi, J. Cho, W. J. Choi, D. H. Woo, S. H. Kim, and K. N. Kang, J. Mat. Sci. Lett. **21**, 1739 (2002)

19. J. S. Yu, J. D. Song, Y. T. Lee, and H. Lim, J. Appl. Phys. **91**, 4256 (2002)

20. M. K. Lee, J. D. Song, J. S. Yu, T. W. Kim, H. Lim and Y. T. Lee, Appl. Phys. A **73**, 357 (2001)

21. L. Fu, P. Lever, H. H. Tan, C. Jagadish, P. Reece and M. Gal, Appl. Phys. Lett. **82**, 2163 (2003)

22. A. Pepin, C. Vieu, M. Schneider, R. Planel, H. Launois, and Y. Nissim, Appl. Phys. Lett. **68**, 3772 (1996).

23. A. Pépin, C. Vieu, M. Schneider, H. Launois, and Y. Nissim, J. Vac. Sci. Technol. B **15**, 142 (1997)

24. L. Fu, R. W. v. d. Heijden, H. H. Tan, C. Jagadish, L. V. Dao, and M. Gal, Appl. Phys. Lett. **80**, 1171 (2002)

CHAPTER 9

Concluding Remarks and Suggestions for Further Work

Many interesting properties of damaged or defective InP and InGaAs have been revealed by the investigations presented in this Thesis, and the combined enhancement or suppression of various of these properties has been demonstrated to be a useful technique for creating potential optoelectronic device materials. The intriguing defect formation and agglomeration contrast between these two semiconductors was studied in depth. Damage in InP was highly sensitive to the implant temperature (room temperature or 200°C), while damage in InGaAs appeared to be independent of the implant temperatures used. Very strong dynamic annealing occurred in InP when implanted at 200°C, though it was weak for implants at room temperature. Dynamic annealing was also strong in InGaAs at both temperatures.

It was found in both semiconductors that, for the same implant dose, the amount and type of damage created in the material did not scale with implant ion atomic mass. Moreover, the amount and type of damage correlated strongly with the observed optical and electrical properties. This was even more true after annealing. In the case of implantation into InP with As and Ga, whose atomic masses were very close to each other, very different structural, optical and electrical properties were observed. Implanting with Fe into both InP and InGaAs in general did produce more extensive damage than implanting with the other elements used in this work, and this can be attributed to the strong chemical reactivity between the implanted Fe and the constituent elements of these III/V semiconductors.

Both InP and InGaAs share a characteristic n-type conductive behaviour, due to intrinsic donors in the case of undoped material, and due to the formation of shallow donors when the material is defective due to being grown at low temperatures or implanted. Such conductive behaviour is not ideal from the point of view of

optoelectronic device applications, since the resulting devices would have high leakage currents, thus causing reduced sensitivity as well as heat fatigue shortening of device lifetimes. As a result of single energy implants into InP with P, As, Ga or In, either single or double n- conductive layers were formed in the region of peak damage, whose conductivity increased with annealing temperature. This n-typeness can be compensated for by doping with Fe, implanting with Fe and annealing to temperatures above 600°C for 30s – both of which rely on deep acceptors caused by Fe complexes to act as trapping centres, or else implanting into initially p-type material. Compensation can also be achieved using implant-isolation techniques, and this was investigated in the case of both n- and p- type InGaAs, where it was found that maximum resistivities occurred at the dose which resulted in the greatest balance between the free carriers, implant induced shallow donors, and implant induced deep traps. In this way, resistivities as high as 10^7 $\Omega/\square$ were achieved in the case of O, C and Li implanted p-type material, although the dose at which this compensation occurred was critical, since at doses above compensation the strong shallow donor formation mechanism quickly reduced resistivities.

The damaged semiconductors have characteristic short optical lifetimes, due to the high concentrations of defects which act as recombination centres. This property was investigated with a view to creating materials for ultrafast optoelectronic applications: ultrafast photodetectors and saturable absorbers for the mode locking of solid state lasers. In the former case, good mobilities and high resistivities are required in addition to the short lifetimes, while in the latter case highly resistive material is not as crucial. It was found that, using the compensation techniques of Fe implantation into

semi insulating material and implants with other elements into *p* - type material, lifetimes as short as 130 fs were achieved in InP and 300 fs in the case of InGaAs, both when implanted with Fe and annealed at 500°C for 30s. Such low annealing temperatures were required to maintain high levels of damage which resulted in the shortest optical lifetimes; however, they did not coincide with Fe activation in the semiconductor. Correspondingly, the sheet resistance in these two cases was $\sim 5 \times 10^5\ \Omega/\square$. To obtain higher resistivities at this annealing temperature, it was necessary to implant into *p* -type material. In the case of *p* -InP, the compensation region turned out to be fairly independent of dose, resulting in decay times of the order of 400 fs and sheet resistivities of $\sim 10^6\ \Omega/\square$, which overall seemed to constitute the optimal parameters for an ultrafast photodetector material. In the case of *p* - InGaAs, sheet resistivities slightly higher than this were achieved, for implant doses above 10^{16} cm^{-2} in samples with a high initial free carrier concentration of $\sim 3 \times 10^{19}$ cm^{-3}. In this case, the damage produced resulted in optical lifetimes below the detection limit of the experiment. The correlation between initial carrier concentration and threshold dose could be further explored using the *p* -type material, such that optimal implant and annealing parameters for ultrafast InGaAs could be obtained.

All of the investigations for the Chapters just mentioned could also be pursued further using multiple energy implant schemes, which would avoid issues relating to the non-uniform damage profile which is a characteristic of the single energy implants.

The defects of InP and InGaAs were also investigated as vectors for interdiffusion in InP/InGaAs and InGaAs/AlGaInAs quantum well systems. In the former system, interdiffusion of both the group III and group V sublattices was possible,

while in the latter system, group III interdiffusion only was favoured. It was found that the thermal stability of the InGaAs/AlGaInAs system was higher than the InP/InGaAs system, due to the fact that interdiffusion on the group V sublattice occurred at much lower temperatures than on the group III sublattice. The defects were introduced into the quantum well structures in two ways: either by implantation, or by chemical reactions with/strain induced by deposition of dielectric layers on the semiconductor surface. In the case of implantation, energies were chosen such that the damage occurred either within an InP or InGaAs capping layer or well into the sample (through the quantum well). When cap layer implantation was employed, the type of capping material (InP or InGaAs) did have an effect on the degree of interdiffusion - this was correlated with the damage accumulation processes in that layer. If the damage was too great, such that thermally stable types of damage such as clusters and loops could be formed, the defects did not migrate down to the quantum well in sufficient quantities during annealing to cause significant interdiffusion. On the other hand, highly mobile point defects caused large amounts of interdiffusion. Correspondingly, InP cap layers resulted in large blueshifts when implants were done at 200°C, due to the greater dynamic annealing and thus greater concentrations of point defects at this temperature. Room temperature implantation into InP capped samples and at high doses reduced this interdiffusion; indeed, at the highest doses, implants at this temperature resulted in amorphisation of the cap layer, indicating the degree to which thermally stable, complex defects were being produced. InGaAs capping layers caused less interdiffusion than InP due to the different damage caused and because of the favoured group III interdiffusion. Deep implants resulted in interdiffusion that was independent of the capping layer, and was greater in the InP/InGaAs system due to the greater group V interdiffusion. In general, cap layer

implantation was the less destructive technique of the two, producing greater interdiffusion.

Impurity free vacancy disordering of the InP/InGaAs quantum wells capped with InP and InGaAs yielded many of the most fascinating results of this work. While the degree of blueshifting in these structures interdiffused by implantation could be explained in terms of the number and type of defects created, IFVD appeared to allow for variation of the respective group III and group V diffusion lengths. This in turn resulted in very large blueshifts of up to ~200 nm, and in some cases redshifting of the peak emission some 60 nm. In other cases, complete suppression of interdiffusion was obtained, even for annealing at 800°C, resulting in a thermally stable quantum well sample which would have otherwise diffused extensively at this temperature. The large range of wavelength tuning options for this system then becomes obvious. When the conditions for dominant group V interdiffusion were created, as in the case for SiO_2 or undoped SOG treatment of the InGaAs capped quantum wells (where a great deal of compressive strain was caused at the quantum well during annealing, and interfacial reactions between the InGaAs and the silica occurred, as well as group V exchange between the cap layer and barrier) extremely large blueshifts were created. Moreover, the quality of the shifted emission peak was excellent. Unlike similar treatments of GaAs/AlGaAs or GaAs/InGaAs systems, the interdiffusion was only weakly dependent on group III element interactions with the dielectric. In addition to the known Ga migration into SiO_2, it has been found that In also forms an oxide and will penetrate through to the dielectric surface in this form. It was postulated that the group III element interactions may provide a kick-start mechanism, after which group V interdiffusion becomes dominant.

When the conditions for dominant group III interdiffusion were created (in-plane tensile strain during annealing, created by deposition of TiO_2 which has a larger thermal expansion coefficient than InP or InGaAs), small blueshifts or redshifts were created. This was explained according to modeling which showed how the combination of strain felt at the quantum well and variations in composition during different stages of interdiffusion resulted in either an increase or decrease in the quantum well bandgap.

Doping spin-on glasses provided further indications of the relative importance of group V and group III interdiffusion in the system, as well as the degree to which interdiffusion could be affected by interfacial reactions between the oxide and the capping layer. Ga doping, similarly to InGaAs/GaAs and AlGaAs/GaAs systems, resulted in a reduced blueshifting due to the smaller incentive for Ga uptake into the SOG from the sample. P doping of the SOG produced an even stronger suppression of blueshifting, which would seem to indicate the greater importance of diffusion on the group V sublattice and supports the idea of dominant group V interdiffusion in the sample using a silica treatment. Given that only a small amount of As-O was found at the semiconductor/dielectric interface, this result is quite interesting.

Ti doping of the SOG produced the strongest suppression of blueshifting, with the peak emission barely moving from its untreated value. The exact reason for this was not clear; further work is required to understand the mechanisms involved in this case.

Many more experiments could be done to elucidate the exact interdiffusion mechanisms in the group V/III - diffusion quantum well systems. Growing structures where only group V diffusion could occur, and then repeating the experiments presented here might give further clues. Studies into the quality of the dielectrics (porosity etc) and the effect of this on interfacial interactions and subsequent interdiffusion also needs to

be thoroughly investigated. Deep level transient spectroscopy and Fourier transform infrared spectroscopy could yield further information about the types of defects occurring in the sample and the quality of the oxides and nitrides deposited. Knowing the effect of different doping elements on the thermal expansion coefficient of the spin on glasses would also be very useful.

The potential of defective InP and InGaAs as materials useful in optoelectronic applications has been extensively explored in this Thesis. In particular, these materials have been shown to have qualities ideal for ultrafast long wavelength optical detection, and the extent of the emission/detection wavelength tuning possibilities of quantum wells made from these semiconductors has also been revealed. In order to achieve these main aims, ways of dealing with the intrinsic n-typeness of the defective InGaAs and InP had to be found, and in the case of interdiffusion studies, the appropriate annealing temperatures and conditions which avoided extensive thermal diffusion and the formation of complex defects had to be established. Many interesting features of these materials could be further investigated with a view to their development for novel device applications.